Cavity enhanced spectroscopies for small volume liquid analysis

Dean James

St. Edmund Hall

University of Oxford

A thesis submitted for the degree of

Doctor of Philosophy

Hilary 2017

Acknowledgements

Firstly, I would like to thank my supervisor Prof. Claire Vallance, and express my eternal gratitude for her enthusiasm, wisdom, guidance and patience over the years.

I would also like to thank the members of the Vallance group, past and present, particularly those who have worked on the cavity side of the laboratory:

- Dr. Cathy Rushworth for her friendship over the years, for starting me off down this path, and for providing the microfluidic chips with integrated mirrors described in Chapter 4.
- Dr. Jason Lee for teaching me how to not break LabVIEW.
- James Foster for help with the initial microcavity experiments.
- İdil Cazımoğlu for always challenging me to think about things from another angle, and for making the basement a brighter place.
- Chris Mason for help in designing the latest microcavity prototype and performing the CFD calculations, as well as for making the last year of my D.Phil. much more entertaining.
- Nick Ramsbottom for teaching me that although a scientist may escape the lab, sometimes the lab may follow you home.

I am also thankful for the friendship and support of the other members of the Vallance group during my time here: Hansjochen Köckert, Weiwei Zhou, Eleanor Morris, David Heathcote, Alfredo Quinto Hernandez, Bethanie Murray, James Bull, Simon-John King, Cécilia Cauchy, Sara Gardiner, Laura Lipciuc, Lorna Wilkinson, Haoyu Niu, and Ed Wilman.

The advice, hard work and expert skills of both the mechanical and electronic workshop teams has been invaluable in the design and construction of each of the cavities described in this thesis. In particular, I am grateful to Charlie Jones for providing training in the student workshop and patiently guiding me as I learned to generate slightly more pragmatic designs.

I would also like to thank those I have collaborated with throughout my D.Phil.:

- Prof. Matt Mowlem of the National Oceanography Centre, and Prof. Hywel Morgan of the University of Southampton for providing expertise on ocean sensing, marine nutrients, and microfluidic devices.
- Dr. Patrick Salter from the Department of Engineering for his assistance experimenting with monolithic waveguide cavities.
- Dr. Nick Barnett of Ocean Optics for going beyond the call of duty when one of our spectrometers suffered a catastrophic firmware failure.
- Immense thanks to Dr. Aurélien Trichet and Prof. Jason Smith from the Department of Materials for providing the opportunity to work with them on the microcavities in their labs. In particular, Aurélien's expertise, patient teaching, and great company truly made this collaboration the highlight of my D.Phil.

In addition, I would like to thank my examiners, Prof. Grant Ritchie and Prof. Andy Ruth, for an illuminating discussion and their helpful comments.

Finally, I would like to thank the Engineering and Physical Sciences Research Council, the Leverhulme Trust, and the Royal Society Paul Instrument Fund for funding my studentship and the microcavity experiments described in this work.

Abstract

Cavity enhanced spectroscopies (CES) are currently amongst the most sensitive spectroscopic techniques available for probing gas-phase samples, however their application to the liquid-phase has been more limited. Sensitive analysis of sub-microlitre liquid samples is highly desirable, as miniaturisation allows for the reaction and analysis of scarce or expensive reagents, produces less waste, and can increase the speed of separations and reactions, whilst having a small footprint and high throughput. Absorption spectroscopy is a particularly desirable technique due to its universal, label-free nature, however its application to small volume liquid samples is hampered by the associated short absorption pathlengths, which limit sensitivity. CES improve sensitivity by trapping light within a confined region, increasing the effective pathlength through the sample.

Three distinct types of optical cavity were constructed and evaluated for the purposes of making optical absorption measurements on liquid samples. The first incorporated a high optical quality flow cell into a "macrocavity" formed from two dielectric mirrors separated by 51.3 cm. Cavity losses were minimised by positioning the flow cell at Brewster's angle to the optical axis, and the setup was used to perform a single-wavelength cavity ringdown spectroscopy experiment to detect and quantify nitrite within aqueous samples. The detection limit was determined to be 8.83 nM nitrite in an illuminated volume of only 74.6 nL. Scattering and reflective losses from the flow cell surfaces were found to be the largest barrier to increased sensitivity, leading us to focus on the integration of cavity mirrors within a microfluidic flow system in the work that followed.

In the second set of experiments, cavity enhanced absorption spectroscopy (CEAS) measurements were performed on Thymol Blue using custom-made microfluidic chips with integrated cavity mirrors. Unfortunately, due to the plane-parallel configuration of the mirrors and the corresponding difficulty in sustaining stable cavity modes, the results were underwhelming, with a maximum cavity enhancement factor (CEF) of only 2.68. At this point, attention was focussed toward a more well-defined cavity geometry: open-access plano-concave microcavities.

The microcavities consist of an array of micron-scale concave mirrors opposed by a planar mirror, with a pathlength that is tunable to sub-nanometer precision using piezoelectric actuators. In contrast to the other experimental setups described, the

microcavities allow for optical measurements to be performed in which we monitor the change of wavelength and/or amplitude of a single well-defined cavity mode in response to a liquid sample introduced between the mirrors.

In the first microcavity experiment, we used 10 μm diameter mirrors with cavity lengths from 2.238 μm to 10.318 μm to demonstrate refractive index sensing in glucose solutions with a limit of detection of 3.5×10^{-4} RIU. The total volume of detection in our setup was 54 fL. Thus, at the limit of detection, the setup can detect the change of refractive index that results from the introduction of 900 zeptomoles (500,000 molecules) of glucose into the device.

The microcavity sensor was then adapted to enable broadband absorption measurements of methylene blue via CEAS. By recording data simultaneously from multiple cavities of differing lengths, absorption data is obtained at a number of wavelengths. Using 10 μm diameter mirrors with cavity pathlengths from 476 nm to 728 nm, a limit of detection, expressed as minimum detectable absorption per unit pathlength, of 1.71 cm^{-1} was achieved within a volume of 580 attolitres, corresponding to less than 2000 molecules within the mode volume of the cavity.

Finally, a new prototype was developed with improved cavity finesse, a much more intense and stable light source, and improved flow design. Using a single plano-concave microcavity within the array with a cavity pathlength of 839.7 nm, and 4 μm radius of curvature mirror, absorption measurements were performed on Methylene Blue. Analysis of this data indicated a CEF of around 9270, and a limit of detection based on the measured signal-to-noise ratio of 0.0146 cm^{-1}. This corresponds to a minimum detectable concentration of 104 nM Methylene Blue, which given the mode volume of 219 aL, suggests a theoretical minimum detectable number of molecules of 14.

Contents

List of Figures **xi**

List of Abbreviations **xiii**

1 Introduction **1**
1.1 Analysis of small liquid volumes 1
1.2 Existing analytical techniques 2
1.2.1 Absorption spectroscopy 5
1.2.2 Fluorescence spectroscopy 8
1.2.3 Raman spectroscopy 9
1.2.4 Electrochemical detection 10
1.3 Extending absorption pathlengths 11
1.3.1 Single pass techniques 11
1.3.2 Multi-reflection techniques 13
1.3.3 Multi-pass techniques 17
1.4 Thesis outline 17

2 Theory: Optical cavities **19**
2.1 Confinement of light 20
2.2 Cavity configurations 24
2.2.1 Plane parallel cavity 26
2.2.2 Plano-concave cavity 27
2.2.3 Symmetric cavity 27
2.3 Cavity enhanced spectroscopies 27
2.3.1 Cavity ringdown spectroscopy (CRDS) 28
2.3.2 Cavity-enhanced absorption spectroscopy (CEAS) 32
2.3.3 Detection limits 35
2.3.3.1 Minimum detectable absorption per unit pathlength, $\kappa_{\min}$ 35
2.3.3.2 Minimum detectable concentration, $C_{\min}$ 37
2.3.3.3 Absolute number of molecules 37
2.3.3.4 Cavity enhancement factor (CEF) 37

2.4 Sample containment 38
2.4.1 Filling the optical cavity 38
2.4.2 Flow cell in a cavity 41
2.4.3 Optical fibre cavities 45
2.4.4 Whispering gallery mode microcavity resonators 46
2.5 Chapter summary 48

3 Macrocavities 51
3.1 Nitrite detection 51
3.2 532 nm CRDS cavity set-up 55
3.3 Integrating a flow cell into an optical cavity 58
3.4 Experimental 60
3.5 Results 61
3.6 Discussion 64
3.7 Chapter summary 66

4 Cavity-in-a-chip 67
4.1 Chip design and manufacture 67
4.2 Experimental 70
4.3 Results 73
4.4 Discussion 75
4.5 Chapter summary 76

5 Open-access microcavities: refractive index measurements 77
5.1 Microcavity design and fabrication 79
5.2 Experimental setup 81
5.3 Refractive index measurements 86
5.3.1 Theory 86
5.3.2 Flow cell characterisation 90
5.3.3 Refractive index measurements 92
5.4 Chapter summary 97

6 Open-access microcavities: broadband cavity enhanced spectroscopy 99
6.1 Microcavity setup 99
6.2 Absorption measurements 104
6.3 Results 105
6.4 Discussion 108
6.5 Chapter summary 111

7 Open-access microcavities: single-wavelength cavity enhanced analysis **113**
7.1 Microcavity design and fabrication 113
7.2 Cavity-locking scheme 116
7.3 Absorption measurements 119
7.3.1 Optical setup 119
7.3.2 Sample preparation and handling 121
7.3.3 Measurement protocol 122
7.4 Analysis 122
7.4.1 Determination of pathlength 123
7.5 Results 124
7.6 Flow dynamics 126
7.7 Chapter summary 131

8 Concluding remarks **133**

References **139**

x

List of Figures

1.1 Beer-Lambert absorption 5
1.2 Extending absorption pathlengths 11
1.3 Extending single-pass pathlengths 12
1.4 Extending pathlengths with multi-reflection techniques 14

2.1 Stable longitudinal cavity mode 20
2.2 Excitation of multiple longitudinal cavity modes 21
2.3 Transverse modes 22
2.4 Gaussian mode within a plano-concave cavity 23
2.5 A selection of cavity geometries 24
2.6 A schematic of the CRDS process 29
2.7 Comparison of exact and approximate CEAS solutions for κ. 34
2.8 Methods for integrating liquid samples with two-mirror optical cavities 40
2.9 Methods of integrating liquid samples with optical fibre cavities . . 45

3.1 Formation of the azo dye product in the Griess Assay 53
3.2 Absorption spectrum of the azo dye product of the Griess assay. . . 54
3.3 Schematic of macrocavity setup used to detect nitrite 55
3.4 Typical ringdown signal and an Allan standard deviation 57
3.5 Transmission of light through an angled flow cell. 58
3.6 Predicted transmission as a function of incidence angle. 59
3.7 UV-vis absorption data for Griess assay 61
3.8 κ against concentration of nitrite. 62

4.1 Fabrication of a microfluidic chip with integrated cavity mirrors. . . 69
4.2 Schematic of setup used to detect Thymol Blue 70
4.3 Custom-made microfluidic chip with integrated cavity mirrors. . . . 72
4.4 UV-vis absorption data for Thymol Blue. 73
4.5 Microfluidic cavity absorption data for Thymol Blue. 74

5.1 Spectral output from a single microcavity 78
5.2 Open access microcavities 79
5.3 Schematics of custom-built microcavity flow cell. 82

5.4 Tilted wedge-shaped configuration of microcavities. 83
5.5 Schematic of microcavity setup used to detect changed in refractive index. 84
5.6 Mounted microcavity flow cell. 85
5.7 Expected form of wavelength shift as refractive index changes. . . . 91
5.8 White lamp transmission through microcavities. 93
5.9 Results of refractive index microcavity experiment 95
5.10 Allan variance analysis, and cavity displacement as a function of time. 96

6.1 Uniform array of 10 μm diameter concave mirrors, and redesigned mirror mounts. 100
6.2 Schematic of microcavity setup used to perform multi-wavelength CEAS. 103
6.3 UV-vis absorption data for Methylene Blue. 106
6.4 White lamp transmission through a single cavity as a function of concentration/time. 106
6.5 Cavity absorption data for three wavelengths, and plot of CEF and calculated mirror reflectivity as a function of wavelength. 107

7.1 Array of micron-scale concave mirrors, and transmission profile of LaserOptik microcavity mirrors. 114
7.2 Design of polymer seal for flow cell. 115
7.3 Schematic of cavity-locking optical arrangment. 116
7.4 Fabry-Pérot interferometer. 117
7.5 Lissajous circle and transmission profile for cavity-locking scheme. . 119
7.6 Schematic of microcavity optical arrangment used to detect Methylene Blue at a single wavelength. 120
7.7 Allan variance analysis for single wavelength microcavity experiment. 121
7.8 Calculating optical pathlength through a microcavity 123
7.9 Cavity absorption data, yielding absorption coefficient and cavity enhancement factor. 125
7.10 Cavity length fluctuation when pumping solution with Chemyx stepper-motor syringe pump. 127
7.11 Schematic of a pneumatic flow system 128
7.12 Cavity length fluctuation when pumping solution with Elveflow pneumatic syringe pump. 129
7.13 Computation fluid dynamics simulation of flow rate and force exerted on patterned mirror holder. 130

List of Abbreviations

μTAS . . . . . Miniaturised (Micro-) total analysis system.

BBO . . . . . Barium borate.

CCD . . . . . Charge coupled device.

CEAS . . . . . Cavity-enhanced absorption spectroscopy.

CEF . . . . . Cavity enhancement factor.

CFD . . . . . Computational fluid dynamics.

CMWS . . . . Cavity mode width spectroscopy.

CRDS . . . . . Cavity ringdown spectroscopy.

CW . . . . . Continuous wave.

DNA . . . . . Deoxyribonucleic acid.

DPSS . . . . . Diode pumped solid state.

EBPVD . . . . Electron beam physical vapour deposition.

ESI-MS . . . . Electrospray ionisation mass spectrometry.

ESRII . . . . . Enhanced-specular-reflector II film.

EU . . . . . European Union.

FDTD . . . . . Finite-difference time-domain.

FIB . . . . . Focussed ion beam.

FRET . . . . . Forster resonance energy transfer.

FSR . . . . . Free spectral range.

GC . . . . . Gas chromatography.

GCMS . . . . . Gas chromatography mass spectrometry.

HPLC . . . . . High performance liquid-chromatography.

IBD . . . . . Ion beam deposition.

ICOS . . . . . Integrated cavity output spectroscopy.

LC-MS . . . . Liquid chromatography mass spectrometry.

LCW . . . . . Liquid-core waveguide.

LED . . . . . Light emitting diode.

Nd:YAG . . . Neodymium-doped yttrium aluminium garnet.

NICE-OHMS Noise-immune cavity-enhanced optical heterodyne molecular spectroscopy.

NIR . . . . . Near-infrared.

NMR . . . . . Nuclear magnetic resonance.

PC . . . . . Personal computer.

PCR . . . . . Polymerase chain reaction.

PDMS . . . . . Polydimethylsiloxane.

PMMA . . . . Polymethylmethacrylate.

ppt . . . . . Parts per trillion.

rpm . . . . . Revolutions per minute.

SERS . . . . . Surface-enhanced Raman spectroscopy.

TEM . . . . . Transverse electromagnetic modes.

TRIS . . . . . Tris(hydroxymethyl)aminomethane.

UV . . . . . Ultraviolet.

UV-vis . . . . Ultraviolet-visible.

WGM . . . . . Whispering gallery mode.

WHO . . . . . World Health Organisation.

1 Introduction

Cavity enhanced spectroscopies are currently amongst the most sensitive spectroscopic absorption techniques available for gas-phase samples [1], however their application to the liquid-phase has been more limited. In this thesis, we will explore a number of approaches for performing cavity-enhanced spectroscopic measurements on small liquid samples, and evaluate the detection limits of such techniques. We begin in this chapter with a description of existing detection techniques, beginning with absorption spectroscopy. We explore a number of methods for improving the detection sensitivity of absorption spectroscopy by increasing the pathlength through the sample, before exploring the use of optical cavities in cavity enhanced spectroscopies. This chapter then concludes with an outline of the remaining chapters in this thesis.

1.1 Analysis of small liquid volumes

The ability to perform chemical synthesis and analysis on a microfluidic scale (defined as 10^{-9} to 10^{-18} L [2]) is highly desirable. Miniaturisation allows for the reaction and analysis of scarce or expensive reagents, produces less waste, and can increase the speed of separations and reactions, whilst having a small footprint and high throughput [3–5]. The concept of such a "miniaturised total analysis system

(μTAS)" was proposed by Manz *et al.* in 1990, and the aforementioned features have made such devices excellent candidates for a wide range of applications [6, 7], including molecular and cell biology [8, 9], pharmaceutical development [10], chemical synthesis [11–13], microanalysis [14, 15], and environmental sensing [16–22].

Since they were first mooted in 1990, these so-called "lab-on-a-chip" devices have undergone many advances in both sample handling capabilities and fabrication techniques [23–26]. However sensitive detection of the very small amounts of analyte the devices contain remains a significant challenge. Minute detection volumes and extremely short pathlengths severely limit the application of traditional single-pass spectroscopic absorption methods, and the high separation speeds achieved place a high demand on the time resolution of any detection method to be utilised. Section 1.2 details a number of analysis methods that have proved effective for certain applications, including fluorescence spectroscopy [27], electrochemical detection [28, 29], Raman spectroscopy [30, 31], NMR [32] and mass spectrometry [33].

In this thesis, we are particularly interested in the application of UV-visible absorption spectroscopy to microfluidic samples due to its universal nature: many analytes absorb light at a range of frequencies and, by selecting a frequency range over which the solvent is transparent, it is possible to perform label-free detection.

1.2 Existing analytical techniques

The analysis of liquid samples can be divided into five broad categories based on the relative distance of the analysis from the process of interest [34]:

1. **Off-line analysis:** The sample is removed from the process line and transported off-site to the measuring instrument. The core advantage of this method is that sophisticated instrumentation, such as liquid chromatography mass spectrometry (LC-MS), can be utilised in an economical time-sharing manner, with dedicated expert staff available for consultation. However, the concomitant time delay can lead to a bottleneck in operations, with competition for resources and increased administration limiting efficiency.

2. **At-line analysis:** The sample is removed from the process line and placed in an adjacent dedicated analysis instrument. Although this reduces time delays, the lack of automation and increased sample volumes often required limit the advantages offered by microfluidic devices.

3. **On-line analysis:** An automated sampling system is used to extract the sample, condition it, and present it to an analytical instrument for measurement. This can either be done in an intermittent flow (such as in LC analysis) or in a continuous fashion (spectroscopic methods). However, this requires the fabrication of a dedicated sampling line to deliver samples to the instrument, along with a concomitant loss of reagents/products.

4. **In-line analysis:** Analysis is performed *in situ* within the process line, using a probe that is chemically sensitive. Chemical sensitivity is obtained by a selective chemical reaction or by chem/physisorption to a chemically selective surface. At this point, some physical consequence of the chemically selective stage, such as release of heat or change of optical absorption, is monitored.

5. **Non-invasive analysis:** The ideal technique, this does not disturb the sample line or any of its processes in any way. Most techniques rely on UV, visible or near-infrared (NIR) spectroscopy.

Both off-line and at-line analysis are commonplace when employing more conventional analysis techniques such as NMR [13, 32], mass spectrometry [33], HPLC [11, 35], GC [36] and GCMS [37–39]. However, such techniques do not utilise some of the core advantages of microfluidic device, such as its small size and low cost. They also often require processes to be run for much longer than would otherwise be necessary, in order to generate sufficient volumes for analysis. In addition, sample integrity may be compromised during quenching or manual transfer processes.

On-line versions of some of these techniques have been demonstrated. On-line GCMS was utilised by Pang *et al.* [40] in the rapid, automated and sensitive determination of ambient gaseous formaldehyde. The μTAS device consisted of a

2 m long, 620 μm internal diameter reaction micro-channel, providing enhanced gas/liquid phase contact-area-to-volume ratio and high heat transfer rate, resulting in a fast and high efficiency derivatisation reaction. This device was coupled with the auto-sampler of a GCMS, and achieved continuous sampling and quantitative analysis of this derivative with a time resolution of around 30 minutes.

Yin *et al.* [41] presented a microfluidic approach to HPLC, integrating an enrichment column and separation column into a single microfluidic device. The fluid channel dimensions varied from 5 μm in width and depth, to 250 μm wide and 50 μm deep. The columns were packed using conventional reversed-phase chromatography particles. A face-seal rotary valve provided a means for switching between sample loading and separation configurations with minimum dead and delay volumes while allowing high-pressure operation. The HPLC chip and valve assembly were mounted within a custom electrospray source on an ion-trap mass spectrometer to enable on-line LCMS analysis. Microfluidic integration of the HPLC components enabled separations with subfemtomole detection sensitivity. Additionally, reducing the diameter of the emitter to microfluidic dimensions increases the probability of ionising the analyte, and since ESI-MS is a concentration sensitive technique, the flow rate can be reduced without loss of sensitivity, reducing the sample required for measurement.

In the case of NMR, for which it is not trivial to adopt an on-line version due to the need for large magnetic fields, at-line instruments have been specially adapted for microfluidic samples to reduce volumes required: solenoid radio-frequency coils less than 1 mm in diameter have achieved an improvement in mass sensitivity of more than two orders of magnitude on volumes of less than 5 nL, compared to conventional 5 mm NMR probes [42].

Detection and analysis of microfluidic samples has been the subject of a number of recent reviews [6, 43–47], and in recent years there has been a focus on the development of integrated probes for on-line, in-line, or non-invasive analysis as they are more in keeping with the concept of a μTAS system than their off-chip

counterparts. The remainder of this section will discuss these techniques, with a focus on non-invasive spectroscopic and electrochemical methods.

1.2.1 Absorption spectroscopy

Electromagnetic radiation can interact with atoms and molecules by being scattered, absorbed or dispersed. When a photon of a given energy is absorbed, there must be a corresponding equal change in the (quantised) energy of the molecule in order to conserve energy. The type of energy levels involved in these transitions depend upon the wavelength of light being absorbed, λ: electronic transitions can be induced by ultraviolet and visible light sources (150 nm $< \lambda <$ 750 nm); vibrational transitions can be induced by infrared light (750 nm $< \lambda <$ 0.1 mm); and rotational transitions can be induced by microwave radiation (0.1 mm $< \lambda <$ 1 cm). For liquid-phase absorptions, the absorption bands tend to be broad (*ca.* 100 nm). When a molecule is dissolved into a solution, the inherent disorder of a liquid provides numerous different solvent environments around the solute molecules. Each of these environments perturbs the molecular energy levels in a slightly different way. Each molecule therefore exhibits a slightly different absorption spectrum, and the measured spectrum is an amalgam of all the different spectra for each molecular environment. The lineshape is described as being inhomogenously broadened [48].

As all molecules absorb light in some part of the spectrum, absorption spectroscopy provides a label-free, universal, non-invasive, rapid and low cost method of detection. The basis of the technique is to irradiate a sample with a known intensity of incident light, I_0, and measure the intensity of the transmitted light, I. The proportion of light absorbed is given by the Beer-Lambert law:

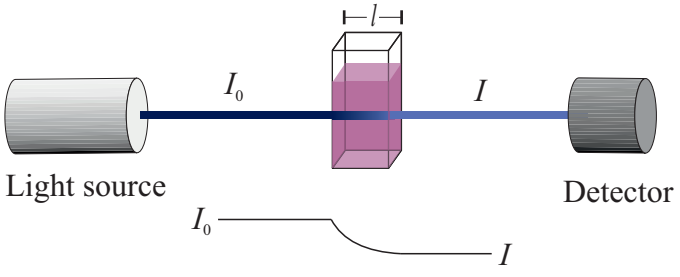

Figure 1.1: A schematic showing the process of Beer-Lambert absorption by a sample.

$$I = I_0 e^{-\alpha Cl} = I_0 10^{-\epsilon Cl} \tag{1.1}$$

where C and l are the concentration of the absorber and the pathlength of the light through the absorber respectively, α is the natural absorption coefficient, and ϵ is the decadic extinction coefficient. These are wavelength dependent properties, characteristic of a particular molecule, which determine the strength of the interaction between a molecule and light of a particular wavelength. In this work, the natural absorption coefficient has been used throughout and any literature or spectrometer values have been converted into this quantity for ease of comparison ($\alpha = 2.303\epsilon$).

Equation 1.1 can be rearranged to find the absorption per unit pathlength, $\kappa = \alpha C$:

$$\kappa = \alpha C = -\frac{1}{l} \ln \frac{I}{I_0} \tag{1.2}$$

The limit of detection ($\kappa_{\min}$) for a single-pass measurement is determined by the ability to detect very small changes in I due to absorption by the sample. In this case, $I \approx I_0$, so using the approximation $-\ln \frac{I}{I_0} \approx 1 - \frac{I}{I_0}$, Equation 1.2 can be reduced to:

$$\kappa_{min} = \frac{1}{l} \left(\frac{\Delta I_{\min}}{I_0} \right) \tag{1.3}$$

where $\Delta I_{\min}$ is the minimum detectable change in intensity due to absorption, usually defined as three times the standard deviation in repeated measurements of I_0.

Equation 1.3 shows that $\kappa_{\min}$ for single-pass absorption spectroscopy measurements is inversely proportional to the single-pass pathlength through the absorbing species, l. This makes absorption spectroscopy of small volumes of liquid a challenge, as the pathlength can be very small. In conventional spectrometers, cuvettes with a pathlength of 1 cm are used to analyse a few millilitres of sample, resulting in relatively sensitive measurements. As an example, the Varian Cary 100 Bio UV-vis spectrometer used during the course of this thesis for benchmark measurements has a detection limit of 3.8×10^{-3} cm^{-1} at 532 nm. Specially designed cuvettes

can allow for the interrogation of much smaller volumes with similar pathlengths, for example the Kratos Spectroflow 757 UV-vis absorption detector has an optical pathlength of 8 mm and a volume of only 12 µL [49]. Methods of enhancing the sensitivity of absorption spectroscopy using special flow cell geometries to increase the optical pathlength through the sample whilst maintaining a low sample volume will be discussed in Section 1.3. However, the exponential dependence of Equation 1.1 on both pathlength and concentration illustrates the incongruence of absorption spectroscopy with the field of microfluidics.

A further obstacle is encountered when attempting to construct an on-line absorption spectrometer for microfluidic devices, as it is difficult to couple light into and out of microfluidic channels with low losses, due to their small size and (often) optically imperfect surfaces. The most common method is to integrate optical fibres into a microfluidic chip to allow light to be pumped into the fluid channel and collected on the other side [50–54]. Typical detection limits for on-line absorption measurements are in the millimolar to micromolar range [55].

Although a key advantage of absorption spectroscopy is its universal, label-free nature, it is possible to greatly enhance the sensitivity of absorption measurements through colourimetric analysis [17]. By selectively chemically reacting the analyte to form a highly coloured compound, it is possible both to enhance the absorption coefficient of the target molecule by several orders of magnitude, and to shift the absorbed wavelength to a region that is not masked by other compounds present in solution. The latter is a common problem when working in the UV or NIR regions, where there are likely to be several overlapping spectra which can complicate quantitative analysis.

Sieben *et al.* [18] achieved a detection limit of 5.6×10^{-4} cm^{-1} through colourimetric analysis of nitrite using a 25 mm pathlength Z-shaped absorption cell (see Section 1.3) in a microfluidic device made from tinted polymethylmethacrylate (PMMA). Colourless nitrite undergoes a highly selective reaction to form a highly coloured azo dye, which is more easily detected, yielding a concentration detection limit of 14 nM. The tinted PMMA was used to prevent stray light that had not

passed through the sample region (a product of the difficulty experienced coupling light into microfluidic channels) from reaching the detector. This was found to improve the detection limit by a factor of ten compared to an identical absorption cell fabricated using untinted PMMA [19].

1.2.2 Fluorescence spectroscopy

In a laser-induced fluorescence experiment, a molecule is excited from its ground electronic state (S_0) to an excited electronic state (S_1) by a laser. Fluorescence is the emission of a photon from the excited state as it returns to the ground state. The wavelength emitted by a fluorescent molecule is typically longer (lower energy photon) than the absorption wavelength, as the excited state undergoes rapid vibrational relaxation prior to fluorescing, lowering its energy. Therefore, by monitoring only at the fluorescence wavelength, it is possible to achieve a background-free measurement, providing high sensitivity.

Fluorescence spectroscopy remains the most widely used optical method for on-chip microfluidic analysis [43, 56] due to the very favourable scaling of the signal-to-noise ratio with the length scale of the channel for a constant number of molecules. As the characteristic length scale, d, is decreased, the background signal generated by Rayleigh and Raman scattering decreases with a cubic relationship to d, whereas the fluorescence signal per molecule is independent of the length scale. In this way, as the length scale is decreased further, the signal-to-noise ratio for detecting very small absolute numbers of molecules increases as d^3. Single molecule fluorescence has been detected in this way in sub-nanolitre volumes [27].

The disadvantage of this method is that it is not universal. Unless the molecule of interest is intrinsically fluorescent, the first step in a fluorescence detection scheme is to selectively react the target molecule to install a moiety which is highly fluorescent when pumped with light of the appropriate wavelength (a process known as "tagging"). As well as introducing a pre-processing step, the mechanism for which may be complicated or expensive, installing a fluorescent tag may otherwise affect the behaviour of the system to be studied, particularly in biological samples.

Microfluidic fluorescence measurements have been used for many applications, for example: digital polymerase chain reaction (PCR) [57–61]; molecular counting and mutation detection with a sensitivity high enough to assess single cell quantities of DNA [60, 62–65]; studying DNA-protein interactions [66–68]; and monitoring of millisecond timescale reaction kinetics [43, 69, 70].

1.2.3 Raman spectroscopy

Raman spectroscopy is based on the weak inelastic scattering of light from a laser. A molecule is excited to a "virtual state" with a photon of excitation light, and releases a photon of different wavelength as the system relaxes to a different quantum state from the one it started in. As with an absorption spectrum, the Raman scattering spectrum provides structural information about the molecule. Not all molecules are Raman-active: Raman spectroscopy requires the molecule to undergo a change in polarisability upon absorption of a photon. Although this non-universal interaction would appear to limit Raman spectroscopy's usefulness, this conditional interaction can provide increased selectivity with respect to the universal UV-vis absorption technique, and can prove useful in condensed matter analysis [31] where a number of molecular species are likely to be present in the sensing region.

High sensitivity Raman spectroscopy has been demonstrated for on-chip chemical analysis in both continuous [30, 71–75] and droplet flow [31, 76–78]. In contrast to fluorescence spectroscopy, in its traditional form, Raman spectroscopy does not require any sample preparation [79]. However, the inherently weak nature of Raman scattering means that long integration times are often required, typically seconds to minutes [30, 71, 78].

For applications requiring improved detection limits, surface-enhanced Raman spectroscopy (SERS) can be used to enhance sensitivity by up to 10 orders of magnitude [71, 80, 81]. Typically, metallic nanoparticles (most commonly gold or silver) are introduced to the sample, to which the analyte binds. At the surface plasmon resonance frequency, conduction band electrons from the nanoparticle generate a large oscillation in the local electric field, enhancing the Raman signal

of the adsorbed analyte. Furthermore, bond formation between the analyte and the metallic surface increases its polarisability [81, 82].

SERS has enabled single molecule detection [80], which would imply that it could provide a potential alternative to fluorescence spectroscopy. However, experimental difficulties in maintaining reproducibility of the size, distribution and relative aggregation of metal nanoparticles, together with inhomogenous distribution of analyte over the surface of the nanoparticles, can lead to variation in the SERS signal that makes quantitative analysis difficult [81]. Furthermore, over time and with each use, fouling of the surface of the metal nanoparticles causes the sensitivity enhancement of SERS to decay.

1.2.4 Electrochemical detection

Thus far we have focussed on optical methods of detection. However, electrochemical detection offers several desirable characteristics: microscaling of electronic systems is a well established field, with most devices proving low cost and possessing low power requirements [83]. There are a considerable number of electrochemical detection methods used in microfluidic devices including potentiometric, amperometric and conductimetric methods [28]. In their simplest form, an amperometric measurement, the working electrode is set to a fixed potential optimised for the analyte of interest, and current is monitored as a function of time. As the analyte approaches the electrode, the applied potential causes oxidation or reduction, and an associated spike in the current is observed. The frequency of this event is directly related to the concentration of analyte present.

Typical on-chip detection limits are in the nanomolar region [84–86], although picomolar and single molecule detection limits have been demonstrated [87, 88]. Whilst optical techniques often suffer from reduced sensitivity as the channel dimensions are reduced, the increased surface to volume ratio this provides enhances analyte flux at the surface of the electrode and can reduce background noise [83, 84, 86]. However, these devices often suffer from fouling of the electrodes, which affects sensitivity over time [89], and often require significant calibration. In addition,

for less electroactive analytes, a pre-processing step may be required in which the analyte is selectively converted into a more detectable derivative [83]. Finally, whilst redox reaction may be thermodynamically favourable, charge-transfer kinetics can limit the usefulness of this technique for certain analytes.

1.3 Extending absorption pathlengths

In section 1.2.1 we discussed the core advantages of absorption spectroscopy for the analysis of liquid samples: it can provide universal, label-free detection, and is experimentally relatively simple. However the small pathlengths intrinsic to microfluidic volumes limit sensitivity, and coupling of light into microchannels can complicate experiments.

One solution is to alter the flow cell geometry such that the optical pathlength is increased whilst attempting to limit any resulting increase in sample volume required. Such strategies can be divided into three categories, illustrated in Figure 1.2: single-pass techniques [90], multi-reflection techniques [91], and multi-pass techniques [92].

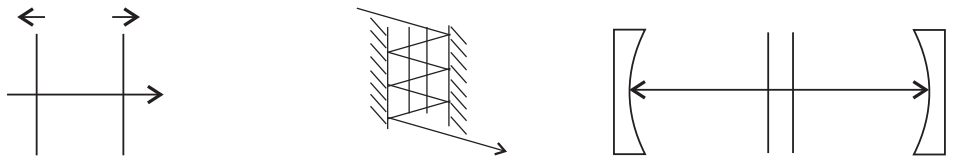

Figure 1.2: Methods of extending pathlengths for absorption measurements: (a) Extending the single-pass pathlength through the sample; (b) Multi-reflection techniques; (c) Multi-pass techniques.

1.3.1 Single pass techniques

The most facile alteration to experimental design is to increase the physical length of channel through which the light can travel without increasing the total volume of liquid. Care must also be taken to ensure that light remains collimated through the length of the channel, to reduce overall losses, and that all light reaching the detector has travelled through the bulk of the sample. This is often achieved through the use of microlenses [93] and optical masks [18], respectively.

Schematics of a selection of single pass schemes are illustrated in Figure 1.3, with literature examples and their experimental parameters reported in Table 1.1.

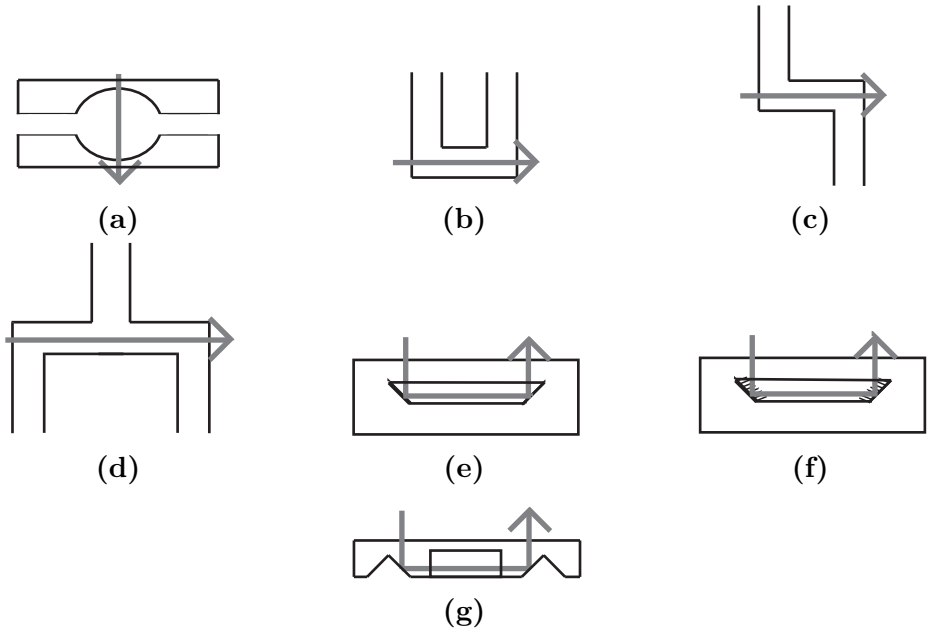

Figure 1.3: A selection of techniques used to extend the pathlength in a single-pass measurement: a) Bubble cell; b) U-shaped cell; c) Z-shaped cell; d) T-shaped cell; e) Prism based cell with reflections at uncoated 45° features in silicon; f) Prism based cell with reflections at mirrored 45° features; and g) Prism based cell with total internal reflection from a pair of V shaped grooves. Adapted from reference [6].

The bubble cell in Figure 1.3a simply increases the width of the channel in the sensing region, resulting in a small increase in the overall flow volume. This method was first used by Xue *et al.* in 1994 [94] in capillary chromatography, enhancing the absorption signal by a factor of 8 relative to measurement across a 50 μm capillary channel. More recently, this method has been used in concert with a colourimetric reaction to detect chromate (VI), achieving a 170 nM detection limit [95].

The channel geometries described by Figures 1.3b through 1.3d incorporate bends into the flow channel, such that the excitation light can pass along the direction of flow. This increases the pathlength of light without increasing the sample volume required, assuming the total length of microfluidic channels on the device does not increase significantly in order to incorporate the sensing region. Sieben *et al.* reported an impressive detection limit of 5.6×10^{-4} cm^{-1} using a

Table 1.1: A comparison of single-pass extended pathlength techniques. Tabulated parameters are the absorption pathlength, l; the probed volume, V; the minimum detectable concentration of the analyte, $C_{\min}$; and the minimum detectable absorption per unit pathlength, $\kappa_{\min}$. The final column states the measured enhancement in absorption signal relative to an equivalent measurement through a 50 μm microchannel. Entries marked with a * indicate analytes that weren't detected directly, instead undergoing a colourimetric reaction to form a strongly coloured product whose concentration is directly proportional to the concentration of analyte. Details of each reaction and the calculated values can be found in the respective references. Adapted from reference [6].

Author	Fig.	Analyte	l/ mm	V/ nL	$C_{\min}$/ μM	$\kappa_{\min}$/ cm^{-1}	Enhance-ment
Xue[94]	1.3a	Malachite green	0.57	0.72	0.004	-	8
Alves-S.[95]	1.3a	Chromate(VI)*	0.6	26680	0.170	-	12
Petersen[90]	1.3b	Caffeine	0.75	0.27	300	4.5	7
Chervet[96]	1.3c	Nucleosides	3.0	5.9	0.89	-	6
Moring[93]	1.3c	DMSO	3.0	13	0.030	-	13
Mainka[97]	1.3c	Formaldehyde*	3.0	.9	0.17	-	20
Ro[98]	1.3c	Fluorescein	0.50	0.68	1.2	4.6×10^{-2}	9
Sieben[18]	1.3c	Nitrite*	25	2250	0.014	5.6×10^{-4}	500
Suhyeon[99]	1.3d	Fluorescein	3.0	13	0.32	-	6
Tiggelaar[100]	1.3e	Indigo carmine	6.0	700	-	-	-
Noda[101]	1.3e	Amaranth	5.0	5000	3.3	1.4×10^{-1}	100
Tiggelaar[100]	1.3f	Indophenol blue	6.0	700	0.002	-	120
Grumann[102]	1.3g	Glucose*	10	10000	120	1.1×10^{-2}	200
Steigert[103]	1.3g	Haemoglobin*	5.0	5000	45	8.1×10^{-2}	100

25 mm long Z-shaped cell (Figure 1.3c) for the colourimetric detection of nitrite in seawater, achieving a detection limit of 14 nM.

An alternative approach is illustrated in Figures 1.3e through 1.3g, in which reflective surfaces are used to reflect light into the plane of the microfluidic chip and along a microchannel, where a second reflective surface then reflects light back towards a detector. This can be achieved through total internal reflection, or by depositing mirror coatings onto angled surfaces, with the latter often demonstrating improved signal levels [100].

1.3.2 Multi-reflection techniques

Another approach to increasing absorption sensitivity within short pathlengths is to induce light to pass through the sample several times before reaching the

detector. Such experimental configurations can be differentiated into multi-reflection techniques, in which the light passes through *different* regions of the sample with each pass (discussed here), and multi-pass techniques, in which light passes through the *same* region of sample (discussed in Section 1.3.3).

Schematics of a selection of multi-reflection schemes are illustrated in Figure 1.4, with literature examples and their experimental parameters reported in Table 1.2.

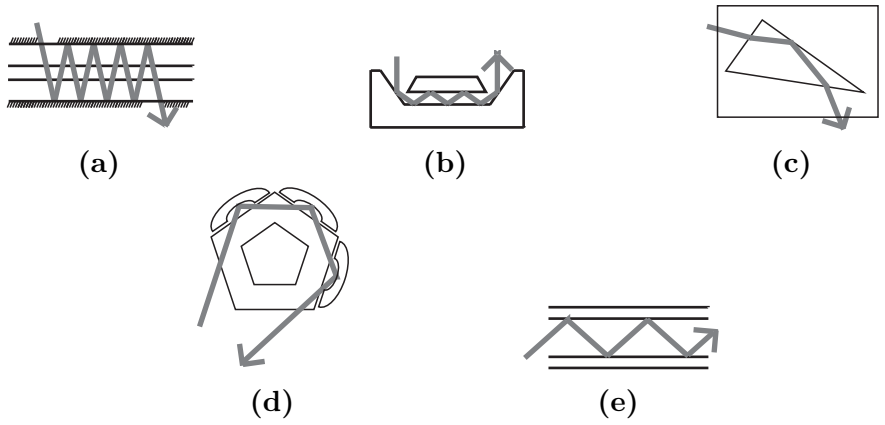

Figure 1.4: A selection of multi-reflection methods to extend the absorption pathlength: a) mirror-coated capillary; b) silicon flow cell; c) hollow Abbé prism; d) "air mirror" flow cells; and e) liquid core waveguide. Adapted from reference [6].

Figure 1.4a illustrates one of the first attempts to utilise multiple reflections to increase optical pathlength through a capillary channel. Wang *et al.* coated the exterior surface of a capillary tube with a silver mirror, with gaps in the mirror coating to allow coupling of light into and out of the capillary [91]. Salimi-Moosavi *et al.* integrated a similar approach into a microfluidic device by patterning aluminium mirrors above and below the microchannel, with input and output coupling regions separated by 200 μm, and demonstrated an increase in optical pathlength by factors between 5 and 10 compared to absorption measurements made perpendicular to the microchannel flow [104].

Figure 1.4b takes a different approach, by utilising total internal reflection to couple light into and along the microfluidic channel. Verpoorte *et al.* demonstrated such a device constructed from silicon, in which a surface angled at 54.7° couples

light into the microfluidic channel such that it reflects from the two opposing surfaces of the channel up to five times before being angled towards the detector [105].

Although such increases in pathlength would appear promising, the poor quality of these reflective surfaces leads to a relatively large loss of coupled light upon each reflection, reducing the signal measured. In the case of Verpoorte *et al.*, only 0.15% of light coupled into the cell reached the detector after five reflections [105]. Therefore, the optimum number of reflections is a compromise between increased optical pathlength and decreased signal levels.

Table 1.2: A comparison of multi-reflection techniques. Tabulated parameters are the absorption pathlength, l; the probed volume, V; the minimum detectable concentration of the analyte, $C_{\min}$; and the minimum detectable absorption per unit pathlength, $\kappa_{\min}$. The final column states the measured enhancement in absorption signal relative to an equivalent measurement through a 50 μm microchannel. Entries marked with a * indicate analytes that were not detected directly, instead undergoing a colourimetric reaction to form a strongly coloured product whose concentration is directly proportional to the concentration of analyte. Details of each reaction and the calculated values can be found in the respective references. The stated $C_{\min}$ for the work of Patey *et al.* is the combined detection limit for nitrite and nitrate. Adapted from reference [6].

Author	Fig.	Analyte	l/ mm	V/ nL	$C_{\min}$/ μM	$\kappa_{\min}$/ cm^{-1}	Enhance-ment
Wang[91]	1.4a	Brilliant green	0.70	6.6	0.065	5.3×10^{-3}	40
Salimi-M.[104]	1.4a	Bromothymol blue	0.20	0.14	3.4	0.25	1.4
Ellis[106]	1.4a	Reactive P	10	5000	0.097	-	2.5
Mishra[107]	1.4a	Bromothymol blue	20	510	0.0044	3.8×10^{-4}	0.85
Verpoorte[105]	1.4b	Cibacron blue 3G	10	15	-	-	1
Llobera[108]	1.4c	Fluorescein	3.58	1777	2.3	-	-
Llobera[109]	1.4d	Fluorescein	14.26	5.340	0.041	1.4×10^{-3}	-
Duggan[110]	1.4e	Crystal violet	5.0	350	0.54	6.5×10^{-2}	-
Patey[111]	1.4e	Nitrate/nitrite*	20000	4×10^{6}	1.5	-	-
Pan[112]	1.4e	Cholesterol	15	100	260	-	-

The hollow Abbé prism (Figure 1.4c) used by Llobera *et al.* is designed to reflect light at a solution/poly(dimethylsiloxane) (PDMS) boundary, increasing pathlength through the sample [108]. Although microlenses were installed at the input and output optical fibres to improve light delivery and collection across this increased pathlength, a large amount of divergence was observed, limiting the proportion of transmitted light reaching the detector. Furthermore, given the low reflection

coefficient at the solution/PDMS boundary ($R < 6.2\%$), long integration times were required to achieve a reasonable signal-to-noise ratio.

These concerns were addressed by Llobera *et al.* in a revised design two years later [109], in which air pockets were introduced at the channel wall such that total internal reflection occurs between the high refractive index PDMS ($n \approx 1.4$) and the air pocket ($n \approx 1.0$). A number of configurations were tested, one of which is illustrated in Figure 1.4d. These "air mirrors" were designed in a curved geometry such that light remains collimated over the extended pathlength, greatly reducing the integration times required. Although detection limits on the order of 10^{-3} cm^{-1} were achieved, the sample volume probed is relatively large (> 1 μL in most designs), and fabrication of the air mirror structures is fairly complicated.

Another approach based on total internal reflection within the microfluidic channel is the use of liquid core waveguides (LCW) [110–112]. If the interior surface of a microfluidic channel is coated with a material of lower refractive index than the solution to be studied, any light coupled into one end of the LCW will be guided down its length in an analogous way to an optical fibre. This is commonly achieved using low refractive index, chemically-resistant polymers such as Teflon ($n \approx 1.3$). In theory, given the low loss of light at each reflection, optical pathlengths can be increased dramatically over single-pass measurements. However, practically, there are often a few complicating factors relating to the use of LCWs.

The first obstacle is the coupling of light into and out of an LCW when integrated with a flow system. The most common approach is the use of T-connectors, in which an optical fibre is placed in line with the end of the LCW, and liquid is introduced at a 90° angle. However, this can result in a significant "dead volume" within the connector, reducing the sensitivity of the system. The need for a T-connector can be removed by introducing bends at the beginning and end of the LCW, such that light can be coupled in and out when striking a surface at less than the critical angle (θ_c) required for total internal reflection to occur. This technique was demonstrated by Pan *et al.* in the point-of-care analysis of DNA and blood-serum cholesterol, achieving a detection limit of 260 μM in a sample volume of just 100 nL [112].

Another problem faced when using LCWs is that any bubbles or contaminants within the liquid core will scatter light, limiting their effectiveness. For this reason it is generally necessary to clean LCWs on a periodic basis in order to maintain performance, and it is generally sensible to limit the length of LCW used in order to reduce the probability of encountering microbubbles on the channel walls.

1.3.3 Multi-pass techniques

Whilst the techniques discussed up to this point show varied levels of success in increasing the pathlength of sample through which absorption can occur, all of them result in some degree of concomitant increase in sample volume, sometimes beyond the realm of microfluidics. In an ideal technique, the *optical* pathlength would be increased whilst maintaining the *physical* pathlength/dimensions of the microfluidic channel. Such a system is known as an "optical cavity": light is confined to a fixed region, reflecting across the same region many times. Multi-pass absorption spectroscopies based on optical cavities are known as cavity enhanced absorption spectroscopies (CEAS), and are a well-developed technique for the analysis of trace analytes in the gas phase [113, 114]. In recent years there has been much interest in adapting these techniques to analyse small liquid volumes [6, 114, 115]. The focus of this thesis has been the development of optical cavity enhanced techniques to analyse liquid volumes ranging from microlitres to attolitres.

1.4 Thesis outline

In Chapter 2, we cover the theory of optical cavities and CEAS in detail, deriving the key equations used throughout this thesis. In Chapter 3, we characterise the integration of microfluidic volumes into a "macrocavity" (a term coined for optical cavities with dimensions on the order of centimetres or more), and apply this technique to the colourimetric analysis of nitrite. Chapter 4 details initial attempts to integrate cavity mirrors into a low-cost rapid-fabrication microfluidic chip, and characterises their sensitivity. In Chapters 5 through 7 we detail the development of a new type of cavity: tunable open-access optical microcavities

based on arrays of high-reflectivity micron-scale hemispherical mirrors with sample volumes <1 fL. We characterise this system, exploring its application to refractive index measurements and multi-wavelength absorption analysis, before developing a new generation of microcavities for high-sensitivity single-wavelength measurements. Finally, we finish with some concluding remarks in Chapter 8 and discuss future work arising from this thesis.

2

Theory: Optical cavities

Cavity enhanced spectroscopies can can be broadly divided into three variants: cavity ringdown spectroscopy (CRDS), cavity-enhanced absorption spectroscopy (CEAS), and phase-shift cavity ringdown spectroscopy (PS-CRDS). The first two techniques are employed in this work. Born out of the aerospace industry as a means of measuring the reflectivity of highly reflective mirrors [116, 117], these cavity-enhanced techniques were first applied to absorption spectroscopy of trace analytes in the gas phase in 1988 by O'Keefe and Deacon [92].

The basis of the approach involves forming an optical cavity, usually from two highly reflective mirrors (reflectivity greater than 99%) positioned opposite each other. By directing a light source onto the back of the first mirror, a small quantity of light (<1%) can be coupled into the cavity, and will be reflected repeatedly between the two mirrors. Placing a detector behind the second mirror allows the measurement of the decay of the small amount of light that escapes the optical cavity upon each reflection, giving information about the rate of any loss processes, from which the loss due to absorption can be separated. In this way, absorption spectroscopy can be performed on samples introduced between the two mirrors. In the gas phase, cavity-enhanced methods are now well established, with routinely high sensitivity; sophisticated variants such as NICE-OHMS have led to detection sensitivities of 8×10^{-11} cm^{-1}, corresponding to a detection limit of 4.5 ppt for ethyne [118].

As light is reflected through the *same* region of the sample multiple times, cavity enhanced techniques benefit from a similar pathlength enhancement over single-pass measurements as the multi-reflection methods described in the previous chapter, but without the associated increase in sample volume, making cavity-enhanced techniques ideally suited for microfluidic applications. In this work, centimeter-scale optical cavities (referred to as "macrocavities") and micron-scale optical cavities (referred to as "microcavities") are developed for measuring the concentration of analytes in microfluidic samples.

2.1 Confinement of light

The use of optical cavities for sensing relies on the ability of the cavity to trap light within it, in the form of a stable standing wave. For a wave to be stable within the cavity there therefore needs to be no phase difference introduced after one round trip of the cavity. This condition is summarised in Equation 2.1:

$$d = \frac{q\lambda_0}{2n} \tag{2.1}$$

where λ is the wavelength of light through vacuum, n is the refractive index of the medium within the cavity, d is the cavity length and q is the cavity mode number (which can take any integer value larger than zero), as illustrated in Figure 2.1.

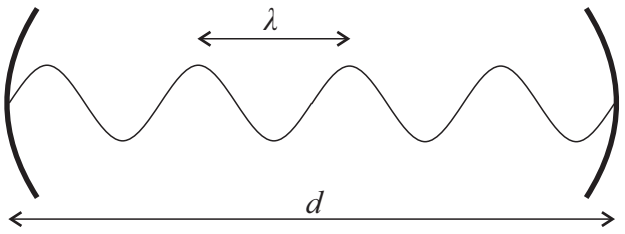

Figure 2.1: A stable, longitudinal cavity mode (with $q = 8$) supported in an optical cavity

Using $\lambda = \frac{c}{\nu}$, with c the speed of light and ν its frequency, Equation 2.1 can be rearranged to give the frequency of the light in a cavity mode:

$$\nu = \frac{qc}{2nd} \tag{2.2}$$

The supported cavity modes are therefore equally spaced in frequency by a quantity known as the free spectral range (FSR), $\Delta\nu$:

$$\Delta\nu = \nu_q - \nu_{q-1} = \frac{qc}{2nd} - \frac{(q-1)c}{2nd}$$

$$= \frac{c}{2nd}$$

In a macrocavity, the cavity length, d, is generally so large compared to the wavelength of light trapped in the cavity that there are multiple longitudinal cavity modes supported in the cavity (see Figure 2.2). A 50 cm long cavity has a FSR of 300 MHz, which is much smaller than the bandwidths of most pulsed lasers, such as the Nd:YAG microchip lasers used in our macrocavity experiments. As our laser source has a bandwidth that will overlap many cavity modes, mode-matching the light to the cavity is not a requirement.

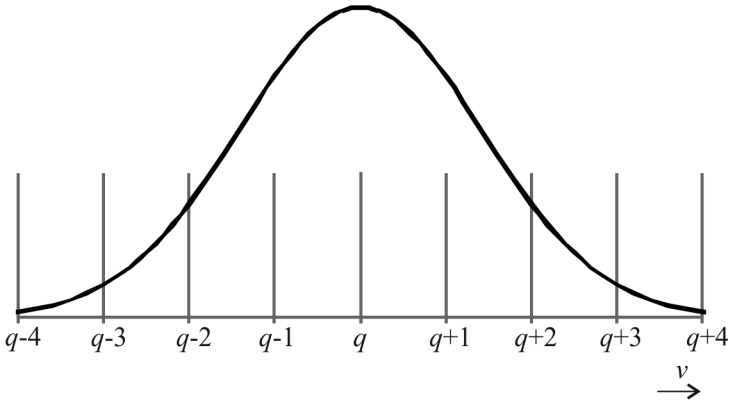

Figure 2.2: Excitation of multiple longitudinal cavity modes using a pulsed laser.

However, in a microcavity d is so small that the FSR is very large, and there are usually only one or two resonant wavelengths supported by the cavity. In this environment there are two possibilities, both of which are explored in this thesis: using a light source with a broad bandwidth allows us to tune the cavity length to select a particular frequency from within its range [119]; alternatively if coupling to a narrowband laser, tuning the laser and cavity mode to achieve resonance is a key consideration [120].

So far, we have only considered longitudinal modes, in which the positions of zero electromagnetic field intensity (known as nodes) occur in the direction of light propagation. There are also a set of transverse optical modes associated with each longitudinal mode that a cavity will support, which possess nodes in the plane perpendicular to the direction of light propagation, resulting in distinctive spatial structures. Figure 2.3 shows the cross sections of a set of transverse modes. Multiple longitudinal and transverse mode excitation results in multiexponential decays, because each mode has a different cavity lifetime. Transverse modes are usually populated by light entering the cavity at a slight angle, by imperfections in the mirrors, or through the incident light being improperly focussed onto the mirrors and therefore being poorly mode-matched with the longitudinal mode(s). For the experiments in this work, the populations of any transverse modes other than the fundamental Gaussian TEM_{00} mode are generally minimised through careful alignment, in order to simplify the data analysis.

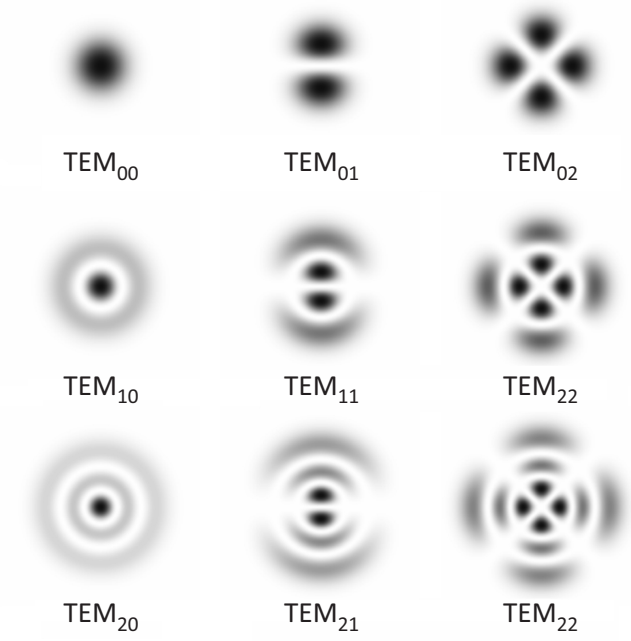

Figure 2.3: A set of transverse modes in cylindrical symmetry. For TEM_{nm}, n refers to the number of radial nodes and m refers to the number of angular nodes. Adapted from [121].

Assuming that the mirrors are perfectly aligned, such that all light is coupled into a Gaussian longitudinal mode, then the beam radius, $\omega(z)$, is given by the

radius of a cross-section of the mode taken normal to the direction of propagation. This is described by [122]:

$$\omega^2(z) = \omega_0^2\left(1 + \left(\frac{\lambda z}{\pi\omega_0^2}\right)^2\right) \tag{2.3}$$

where ω_0 is the beam waist, the point where the wavefronts have zero curvature and the beam radius is at a minimum, and z is the distance along the propagation axis from this point. This function is illustrated for a plano-concave cavity in Figure 2.4.

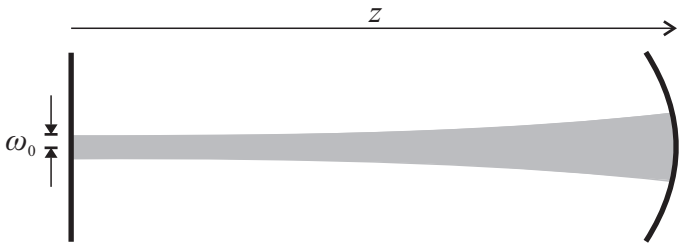

Figure 2.4: Schematic of the contour of a Gaussian mode in a plano-concave cavity, with the beam waist ω_0 shown as the radius of the beam at the surface of the planar mirror.

For a cavity constructed from two identical concave mirrors, as in Figure 2.1, the beam waist occurs at the centre of the cavity, and can be shown to be [122]:

$$\omega_0 = \left(\frac{\lambda l}{2\pi}\right)^{\frac{1}{2}}\left(\frac{2r}{l} - 1\right)^{\frac{1}{4}} \tag{2.4}$$

while for the plano-concave cavities, shown in Figure 2.4, the beam waist occurs at the surface of the planar mirror, and can be shown to be:

$$\omega_0 = \left(\frac{\lambda l}{\pi}\right)^{\frac{1}{2}}\left(\frac{r}{l} - 1\right)^{\frac{1}{4}} \tag{2.5}$$

where l is the optical cavity length, distinct from the geometric cavity length as it includes the penetration depth of the mirrors, and r is the radius of curvature of the mirrors.

Using the Gaussian beam model, the mode volume, V, is then taken to be:

$$V = \frac{\pi\omega_0^2 l}{4} \tag{2.6}$$

This mode volume is important for the purposes of miniaturization, as it allows us to calculate the volume within the cavity that is probed by a measurement.

2.2 Cavity configurations

There are a number of feasible arrangements of mirrors that can support a stable cavity mode. For the purposes of this thesis we will limit our discussion to the three configurations used in our experiments: plane-parallel, plano-concave, and symmetric cavities, shown schematically in Figure 2.5.

Figure 2.5: (a) A plane parallel cavity arrangement; (b) A plano-concave cavity arrangement; (c) A symmetric cavity arrangement.

By treating the light propagating within the cavity as a Gaussian beam, we can use ray transfer matrices to derive the stability criterion for the cavity [122]. As seen in Section 2.1, a cavity is stable when a standing wave is formed - i.e. a beam of light reflecting back and forth reproduces itself exactly on each round-trip in terms of wavefront, curvature, beam size and phase. A beam can be described at some point z along its axis of propagation in terms of its waist, ω_0, the radius of curvature of its wavefronts, R, and the wavelength, λ. These properties are usually written in terms of the complex beam parameter, ζ:

$$\frac{1}{\zeta(z)} = \frac{1}{R(z)} - \frac{i\lambda}{\pi {\omega_0}^2} \tag{2.7}$$

Ray transfer matrices allow for the change in ζ during its propagation through an optical system to be considered in terms of a transformation matrix, which is written as:

$$\begin{bmatrix} \zeta_2 \\ 1 \end{bmatrix} = \begin{bmatrix} A & B \\ C & D \end{bmatrix} \begin{bmatrix} \zeta_1 \\ 1 \end{bmatrix} \tag{2.8}$$

where ζ_1 and ζ_2 are the complex beam parameters entering the optical system and after the transformation has been applied by the optical system, respectively. The ray transfer matrices for many optical elements are well-established and available

in the literature [122]. The ray matrices required to describe a simple optical cavity are: (i) the ray matrix for travelling through empty space (the cavity) of length d

$$\begin{bmatrix} 1 & d \\ 0 & 1 \end{bmatrix} \tag{2.9}$$

and (ii) the ray matrix for light undergoing reflection at a mirror with radius of curvature R:

$$\begin{bmatrix} 1 & 0 \\ -\frac{2}{R} & 1 \end{bmatrix} \tag{2.10}$$

It is possible to rewrite R in terms of the stability parameter of the mirror g, where $g = 1 - \frac{d}{R}$, such that Matrix 2.10 becomes:

$$\begin{bmatrix} 1 & 0 \\ -\frac{2g-2}{d} & 1 \end{bmatrix} \tag{2.11}$$

Remembering that in order to form a standing wave, the propagating wave must superimpose upon itself exactly, then if the ABCD matrix represents the transformation from one position in the cavity to the same position after one round-trip, it must be true that $\zeta_2 = \zeta_1$. The ABCD matrix must describe the reflection of the beam at one mirror (with radius of curvature R_1), propagation through the cavity of length d, reflection at the second mirror (with radius of curvature R_2) and propagation through the cavity of length d once again. The resulting matrix after this round trip is therefore found by multiplying the matrices of the mirrors (with stability parameters g_1 and g_2) and the matrices of propagation in space:

$$\begin{aligned} \begin{bmatrix} A & B \\ C & D \end{bmatrix} &= \begin{bmatrix} 1 & d \\ 0 & 1 \end{bmatrix} \begin{bmatrix} 1 & 0 \\ -\frac{2g_2-2}{d} & 1 \end{bmatrix} \begin{bmatrix} 1 & d \\ 0 & 1 \end{bmatrix} \begin{bmatrix} 1 & 0 \\ -\frac{2g_1-2}{d} & 1 \end{bmatrix} \\ &= \begin{bmatrix} 4g_2g_1 - 2g_2 - 1 & 2g_2d \\ \frac{4g_1g_2-2g_2-2g_2}{d} & 2g_2 - 1 \end{bmatrix} \end{aligned} \tag{2.12}$$

Given that $\zeta_2 = \zeta_1 = \zeta$, we can rearrange Matrix 2.8:

$$\frac{1}{\zeta} = \frac{C + D\frac{1}{\zeta}}{A + B\frac{1}{\zeta}} \tag{2.13}$$

$$B\left(\frac{1}{\zeta}\right)^2 + (A-D)\frac{1}{\zeta} - C = 0 \tag{2.14}$$

It is now possible to solve for $\frac{1}{\zeta}$ using the quadratic formula. As ζ must be a complex number in order for the beam waist ω_0 to have a real value (see Equation 2.7), we know that the discriminant must be negative - i.e.:

$$(A-D)^2 + 4BC < 0 \tag{2.15}$$

Substituting in A, B, C and D from Matrix 2.12, and simplifying gives:

$$g_1^2 g_2^2 - g_1 g_2 < 0 \tag{2.16}$$

This gives the condition for cavity stability as:

$$0 < g_1 g_2 < 1 \tag{2.17}$$

For a stable cavity, the product of the mirrors' stability parameters should be between 0 and 1. Substituting in $g = 1 - \frac{d}{R}$ for each mirror, we can now consider the three cavity configurations used in this thesis.

2.2.1 Plane parallel cavity

For the case of a plane-parallel cavity, $R_1 = R_2 = \infty$, and so $g_1 g_2$ is equal to 1 for all cavity separations. As a result, using a plane parallel configuration in principle allows stable cavity modes for any cavity length. A disadvantage, however, is that the mirror alignment is critical, and a small deviation in alignment angle will result in the modes "walking" out of the cavity. In addition to this, the mode volume for these types of cavities is poorly defined.

A solution is to use at least one concave mirror. The mode volume then becomes well defined (see Equation 2.6), and alignment is easier to achieve.

2.2.2 Plano-concave cavity

In this case, $R_2 = \infty$, such that $g_2 = 1$. This results in a stability criterion of:

$$0 < \left(1 - \frac{d}{R_1}\right) < 1 \tag{2.18}$$

and therefore:

$$0 < d < R_1 \tag{2.19}$$

The cavity length is limited to less than the radius of curvature of the curved mirror.

2.2.3 Symmetric cavity

For a symmetrical cavity, with two concave mirrors of equal radius of curvature R, the stability condition becomes:

$$0 < \left(1 - \frac{d}{R}\right)^2 < 1 \tag{2.20}$$

and therefore:

$$0 < d < R \qquad \text{or} \qquad R < d < 2R \tag{2.21}$$

For a stable cavity, cavity length can either be between 0 and R, or between R and $2R$.

2.3 Cavity enhanced spectroscopies

As discussed at the beginning of this chapter, in CRDS and CEAS, excitation light is trapped within an optical cavity and reflects repeatedly between two highly reflective mirrors. If a sample is placed between the mirrors, any light coupled into the cavity will be reflected through the sample many times, thereby increasing the optical pathlength without altering the physical pathlength. On each pass, a very small proportion of the light is transmitted through the mirror rather than

being reflected, and this output can be measured. This is illustrated in Figure 2.6. Comparison of the cavity output with and without sample present allows us to isolate sample absorption from other loss processes. Both CRDS and CEAS have been the subject of many excellent reviews, some of which are highlighted [113–115, 120, 123–127], and of particular interest are those reviews relating to liquid analysis using optical cavities [6, 114, 115].

The experimental technique is essentially the same for CRDS and CEAS, the difference being that the output is time-resolved in CRDS, but time-integrated in CEAS. As detailed in the following sections, the data analysis differs between the two techniques. CRDS or CEAS can be used in the macrocavities discussed in this work, but only CEAS can be used in the microcavities, as the light is confined in the cavity for such a small period of time that a time-resolved measurement would be very difficult to make. The equations required to analyse the data from such measurements will be derived in the following section.

2.3.1 Cavity ringdown spectroscopy (CRDS)

The CRDS experiments performed within the course of this thesis have utilised pulsed laser sources, although there are continuous wave (CW) variants. For the derivation of the governing equations, consider initially the case in which the duration of the pulse of excitation light is shorter than the amount of time it takes the pulse of light to make a complete round trip of the optical cavity; the cavity output will then be observed as a train of pulses with decreasing intensity as given by the following equations.

When the incident light, with intensity I_{laser}, impinges on the back of the first mirror with reflectivity R[1], a small fraction, $1-R$, is coupled into the cavity. As the coupled light travels through the cavity it interacts with any absorbing species in the cavity, which can usually be modelled as Beer-Lambert absorption (see Equation 1.1). It then impinges on the surface of the second mirror and the fraction of the

[1] R is taken as the geometric average, $R = \sqrt{R_1 R_2}$, in the case of non-identical mirrors

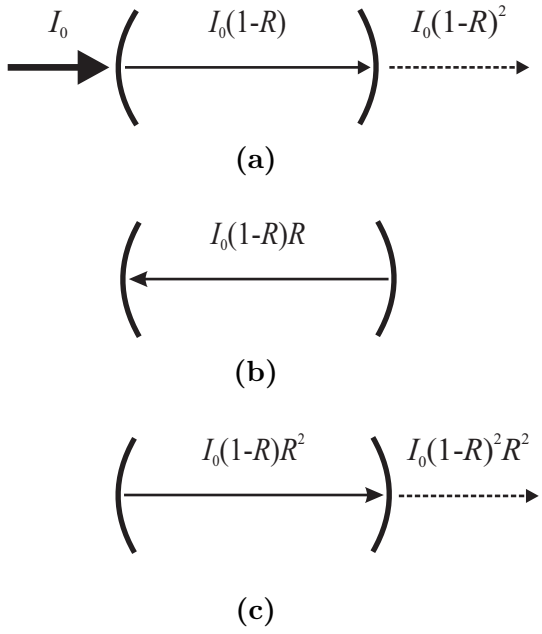

Figure 2.6: A schematic of the CRDS process: a) Light is directed on the back of the first mirror, and a small portion is coupled into the cavity. It makes one pass through the cavity and a small portion is coupled out of the rear mirror and is detected as the first peak in the pulse train; b) Most of the light is reflected by the mirror coating and remains in the cavity to make a second pass; and c) Most of the light again remains in the cavity and makes a third pass, at which point a small amount of light is coupled out of the rear mirror and is detected as the (smaller) second peak in the pulse train

remaining intensity coupled out of the cavity is again, $1 - R$. Thus, after one pass the transmitted light intensity (Figure 2.6a) will be given by:

$$I_0 = I_{\text{laser}}(1 - R)^2 e^{-\alpha C l} \tag{2.22}$$

The light remaining in the cavity makes another pass through the absorbing species (Figure 2.6b). When the light reaches the first mirror again, the same proportion is reflected back through the cavity a third time. After this round trip of the cavity, $1 - R$ is again transmitted through the second mirror and reaches the detector (Figure 2.6c). The cavity output after the first round trip is therefore given by:

$$\begin{aligned} I_1 &= I_{\text{laser}}(1 - R)^2 e^{-\alpha C l} R^2 e^{-2\alpha C l} \\ &= I_0 R^2 e^{-2\alpha C l} \end{aligned} \tag{2.23}$$

Taking R and αCl as constant over the course of a single measurement, and by following the same logic, the intensity of the cavity output after n round trips can be given as:

$$I_n = I_0 R^{2n} e^{-2n\alpha Cl} \tag{2.24}$$

Using the relationship $R^{2n} = e^{2n \ln R}$ this can be written as:

$$I_n = I_0 e^{-2n(\alpha Cl - \ln R)} \tag{2.25}$$

If the laser pulse duration is shorter than the cavity round-trip time, the signal observed consists of a train of pulses with exponentially decaying intensities. Consecutive peaks in the pulse train correspond to consecutive values of n in Equation 2.25, but n can also be expressed in terms of time, $t = \frac{2nd}{c}$, where c is the speed of light in the cavity medium and d is the cavity length, including the penetration depth of the light into the mirrors. This penetration depth can be neglected in the macrocavities as it is so small (<1 μm) compared to the total length of the cavity. However, in the microcavities the cavity length is small enough for it to become significant, so must be considered. Rearranging for n and substituting in to Equation 2.25 gives:

$$I(t) = I_0 e^{-\frac{ct}{d}(\alpha Cl - \ln R)} \tag{2.26}$$

The ringdown time, τ, is defined as the time it takes for the cavity output to decay to $\frac{1}{e}$ of the intensity of the cavity output after the first pass through the cavity:

$$I(t) = I_0 e^{-\frac{t}{\tau}} \tag{2.27}$$

Comparing Equation 2.26 and Equation 2.27:

$$\tau = \frac{d}{c(\alpha Cl - \ln R)} \tag{2.28}$$

Given that the reflectivity of optical cavity mirrors, R, is very close to 1, the approximation $-\ln R \approx 1 - R$ can be used, yielding:

$$\tau = \frac{d}{c(\alpha C l + 1 - R)} \tag{2.29}$$

Thus far we have assumed an ideal cavity, in which the only losses from the optical cavity are due to absorption by the sample and transmission through the mirrors. In reality, for a non-ideal cavity, the term $(1 - R)$ is replaced by the summative loss term, L, which incorporates all losses intrinsic to the cavity.

$$\tau = \frac{d}{c(\alpha C l + L)} \tag{2.30}$$

In the case of no sample absorption (i.e. the blank measurement) the baseline ringdown time, τ_0, which characterises the intrinsic losses from the cavity itself, is given by:

$$\tau_0 = \frac{d}{cL} \tag{2.31}$$

By comparing Equation 2.30 with Equation 2.31 we can write an expression for the absorption per unit pathlength, $\kappa = \alpha C$:

$$\kappa = \frac{d}{cl}\left(\frac{1}{\tau} - \frac{1}{\tau_0}\right) \tag{2.32}$$

where d is the cavity length, l the single-pass pathlength through the sample, and c the speed of light. Thus, if a measurement is made with and without a sample present in the cavity, we can determine the sample absorption.

Ringdown times can be seen to depend only on the losses from the cavity, and are therefore independent of the intensity of light used. Thus CRDS has the advantage of being largely immune to shot-to-shot noise in the intensity of the laser pulses [128]. In principle, the sensitivity of such a technique increases with the mirror reflectivity as the effective pathlength of light through the sample increases. However, practically, detector noise becomes a limiting factor as light output from the cavity decreases.

CRDS measurements can also be made for optical cavities within which the round trip time is shorter than the pulse duration, using the same equations. The

advantage of being able to resolve a pulse train is that the time separation between peaks in a ringdown gives a real-time measure of the cavity length, d.

2.3.2 Cavity-enhanced absorption spectroscopy (CEAS)

For applications in which time-resolved detection electronics are not desired, or simply not practical, such as in the microcavities discussed in this work, CEAS provides an alternative approach to CRDS. Also known as integrated cavity output spectroscopy (ICOS), in contrast to CRDS, the cavity output is time integrated, requiring simpler (and often less expensive) detection electronics [120]. The total cavity output is measured for a constant integration time, such that the total number of passes is approximately the same, and in any case is sufficiently large that it can be approximated to be infinite for the purposes of deriving analytical expressions to describe the signal. The measured intensity is simply the sum of the cavity output from every odd number of passes, and can be expressed as a geometric series involving terms from inherent cavity losses and from absorption by the sample [129]:

$$I = I_{\text{laser}}(1-R)^2 e^{-\alpha C l} \sum_{n=0}^{\infty} R^{2n} e^{-2n\alpha C l} \tag{2.33}$$

As $R^2 e^{-2\alpha C l} < 1$ the series converges to give:

$$I = I_{\text{laser}} \frac{(1-R)^2 e^{-\alpha C l}}{1 - R^2 e^{-2\alpha C l}} \tag{2.34}$$

As with CRDS, if measurements are made with and without a sample present in the cavity, losses due to sample absorption can be isolated. Without a sample the intensity, I_0, is given by:

$$\begin{aligned} I_0 &= I_{\text{laser}} \frac{(1-R)^2}{1-R^2} \\ &= I_{\text{laser}} \frac{1-R}{1+R} \end{aligned} \tag{2.35}$$

Dividing Equation 2.35 by Equation 2.34 gives:

$$\frac{I_0}{I} = \frac{1 - R^2 e^{-2\alpha C l}}{(1-R^2) e^{-\alpha C l}} \tag{2.36}$$

Equation 2.36 can be rearranged into a quadratic equation in terms of $e^{-\alpha Cl}$ and solved:

$$R^2(e^{-\alpha Cl})^2 + (1-R^2)\frac{I_0}{I}e^{-\alpha Cl} - 1 = 0 \tag{2.37}$$

$$e^{-\alpha Cl} = \frac{1}{2R^2}\left(\frac{I_0}{I}(R^2-1) \pm \sqrt{\left(\frac{I_0}{I}(R^2-1)\right)^2 + 4R^2}\right) \tag{2.38}$$

The desired quantity is usually the absorption per unit pathlength, $\kappa = \alpha C$, which can be found by rearranging Equation 2.38:

$$\kappa = -\frac{1}{l}\ln\left(\frac{1}{2R^2}\left(\frac{I_0}{I}(R^2-1) + \sqrt{\left(\frac{I_0}{I}(R^2-1)\right)^2 + 4R^2}\right)\right) \tag{2.39}$$

and when absorption losses are small and reflectivity is high, such that $\frac{I_0}{I}$ and R both tend to 1:

$$\kappa \approx \frac{1}{l}\left(\frac{I_0}{I} - 1\right)(1-R) \tag{2.40}$$

Again the term $(1-R)$ in Equation 2.40 assumes an ideal cavity, so it is often replaced with a term that encompasses all intrinsic cavity losses, L. Figure 2.7 plots κ against $\frac{I_0}{I}$ for both the exact and approximate forms (Equation 2.39 and Equation 2.40, respectively) for the cavity used in the nitrite detection experiment in Chapter 3, i.e. $l = 0.127$ cm and $R = 99.8\%$. The dotted line shows the value of κ below which the approximate form deviates by less than 1% from the exact expression, and corresponds to 22.49% attenuation per pass. Table 2.1 gives details of the cavity configurations used in the experiments discussed in this work, and the attenuation per pass below which the approximation is taken to be valid.

The sensitivity of CEAS is dependent on the initial light intensity (Equation 2.40), unlike CRDS which only depends on the rate of losses from the cavity (Equation 2.32). This dependence has a number of important consequences. Firstly, to be able to determine absolute absorption values, either a calibration measurement must be performed, or the mirror reflectivities must be known over the entire wavelength range of the cavity output. Secondly, an intense light source is required

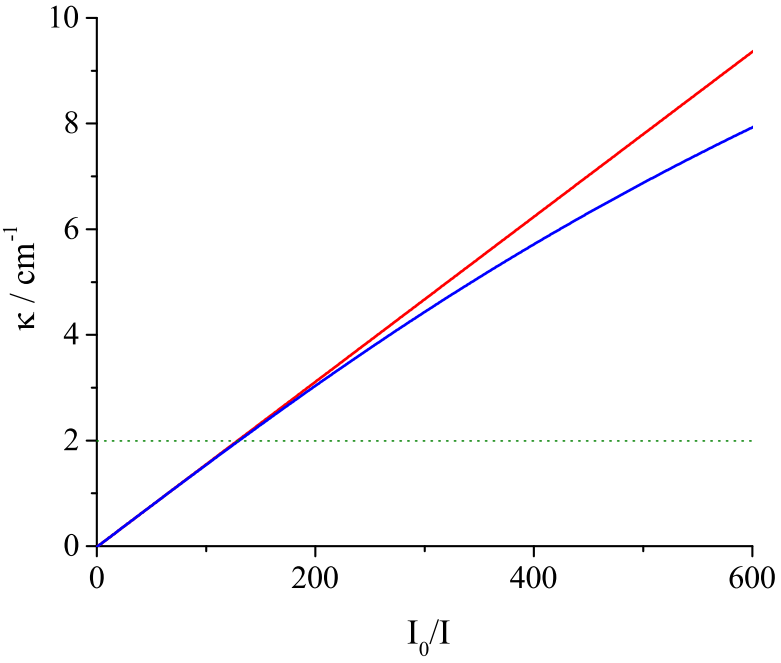

Figure 2.7: Plot comparing κ for the exact (Equation 2.39, red line) and approximate (Equation 2.40, blue line) equations. The green dotted line shows the value for κ corresponding to 22.49% attenuation per pass.

	Macrocavity	Microcavity
Reflectivity, R	0.998	0.9974
Cavity length, d /cm	51.3	0.0001
Single-pass pathlength, l /cm	0.127	0.0001
$\frac{I_0}{I}$ at 1% deviation	129.7	88.3
Maximum valid attenuation per pass / %	22.49	22.84

Table 2.1: A table summarising the validity of the approximate equation for the optical cavities used in the course of this thesis.

in order to achieve a large signal-to-noise ratio at the detector, and increasing the mirror reflectivity beyond a certain point will not improve the sensitivity, as the signal levels will become the limiting factor. Finally, CEAS measurements are not laser-noise immune: if there are significant fluctuations in the light source intensity, this will result in reduced sensitivity for CEAS measurements relative to CRDS.

However, CEAS has a number of advantages over CRDS, including a simpler experimental set-up and simpler data analysis, and has been demonstrated as being at least as sensitive as CRDS in some cases [113, 114]. Therefore, the major disadvantage of CEAS tends to be the requirement for calibration of the

mirror reflectivity at each wavelength. This calibration usually takes the form of a series of absorption measurements using a range of concentrations, C, of a chemical species with known absorption coefficient, α, such that R can be determined from Equation 2.40.

2.3.3 Detection limits

A number of different metrics are used to discuss the sensitivity of different cavity-enhanced experiments depending on the context, each of which will be discussed in this section:

1. **Minimum detectable absorption per unit pathlength, κ_{min}:** often used in the literature as a pathlength and analyte independent comparison of absolute sensitivity.

2. **Minimum detectable concentration, C_{min}:** for a given pathlength and absorption coefficient, this provides a useful metric when the application (and therefore likely concentration of analyte to be detected) is known.

3. **Absolute number of molecules:** a special case for when the detection volume is particularly small, such as in the case of microcavities. As concentrations are usually reported in some molar quantity per dm^{-3}, it can be more useful to consider the exact number of molecules within the detection volume.

4. **Cavity enhancement factor (CEF):** a measure of the proportional enhancement in sensitivity over an equivalent single-pass measurement.

Methods for determining each of these metrics are discussed in the following section.

2.3.3.1 Minimum detectable absorption per unit pathlength, κ_{min}

There are two methods typically used to determine κ_{min} experimentally: a regression measurement; and a spectroscopic method [130]. The regression method involves making repeated measurements of κ at several concentrations, and extrapolating

back to zero concentration. $\kappa_{\min}$ is then defined as three times the standard error in the y-intercept of this plot. This method always gives a larger value for $\kappa_{\min}$ than the spectroscopic method because it is affected by all sources of experimental error, for example errors in making up solutions of a nominal concentration. The spectroscopic method is dependent on the error associated with making repeated baseline measurements and is only affected by the inherent signal-to-noise ratio of the instrument. This metric therefore gives a fairer measure of the best possible limit of detection of the set-up [130].

Spectroscopically, for CRDS measurements the limit of detection is determined by the minimum measurable change in the ringdown time. From Equation 2.32:

$$\begin{aligned} \kappa &= \frac{d}{cl}\left(\frac{1}{\tau} - \frac{1}{\tau_0}\right) \\ &= \frac{d}{cl}\left(\frac{\tau_0 - \tau}{\tau\tau_0}\right) \end{aligned} \tag{2.41}$$

The minimum detectable absorption, $\kappa_{\min}$, corresponds to the smallest detectable change in ringdown time, $\Delta\tau_{\min}$. In this case $\tau \approx \tau_0$ and $\tau_0 - \tau = \Delta\tau_{\min}$. Therefore:

$$\kappa_{\min} = \frac{d\Delta\tau_{\min}}{cl\tau_0^2} \tag{2.42}$$

In practice, $\Delta\tau_{min}$ is generally taken to be three times the standard deviation in repeated measurements of the baseline ringdown time, τ_0.

For CEAS measurements, the limit of detection corresponds to the ability to detect very small changes in intensity output from the cavity. Equation 2.40 can be rewritten:

$$\begin{aligned} \kappa &= \frac{1}{l}\left(\frac{I_0 - I}{I}\right)(1 - R) \\ &= \frac{1}{l}\left(\frac{\Delta I}{I}\right)(1 - R) \end{aligned} \tag{2.43}$$

As above, setting $I \approx I_0$ and $\Delta I_{\min} = I_0 - I$ at the smallest detectable absorption, gives:

$$\kappa_{\min} = \frac{1}{l}\left(\frac{\Delta I_{\min}}{I_0}\right)(1-R) \tag{2.44}$$

In this case, $\Delta I_{\min}$ is defined as three times the standard deviation, 3σ, in the measurement of the baseline intensity, I_0, output from the cavity.

2.3.3.2 Minimum detectable concentration, $C_{\min}$

Once the minimum absorption per unit pathlength has been established, a corresponding minimum detectable concentration *for the pathlength used* can be found simply by dividing by the absorption coefficient, α and pathlength, l:

$$C_{\min} = \frac{\kappa_{\min}}{\alpha l} \tag{2.45}$$

2.3.3.3 Absolute number of molecules

Using Equation 2.6 to calculate the volume of sample being probed and multiplying by the minimum detectable concentration and Avogadro's number gives the minimum absolute number of molecules which could be detected. This is a useful quantity for measuring the limit of detection in microcavities because the very small volumes involved means that the absolute number of molecules being detected can be on the order of tens to hundreds.

2.3.3.4 Cavity enhancement factor (CEF)

The final quantity often used for comparing sensitivities is the cavity enhancement factor (CEF). This is a measure of the proportional enhancement in sensitivity over an equivalent single-pass measurement. For CEAS, comparing Equation 2.44 with the minimum absorption per unit pathlength for an equivalent single-pass measurement, given in Equation 1.3, shows that the gain in sensitivity from the cavity is equal to $\frac{1}{1-R}$, or the reciprocal of the intrinsic cavity losses, L.

For CEAS, the CEF is simply the reciprocal of the inherent cavity losses. For CRDS we can therefore draw a parallel with the blank ringdown time, τ_0, which is inversely proportional to all of the intrinsic cavity losses, L. By comparison

to Equation 2.31, the CEF for CRDS measurements is given by $\frac{c\tau_0}{d}$. This can otherwise be described as the number of passes coupled light makes through the sample in the cavity within one ringdown time, τ_0.

The CEF is a useful quantity for comparing similar types of cavities, however, it is not particularly useful when comparing gas phase measurements with condensed phase measurements. The cavity enhancement factors achieved in cavities designed for liquid-phase measurements are typically much lower than those for gas phase experiments due to the much higher intrinsic cavity losses. However, the much larger number density in the liquid phase means that even modest CEFs can provide acceptable limits of detection.

2.4 Sample containment

Whilst there are many reported uses of cavity-enhanced spectroscopy in the gas phase, with reported sensitivities typically in the range 10^{-6} to 10^{-11} cm^{-1} [1, 118], there has been more limited success in the analysis of liquid phase samples, with sensitivities in the range 10^{-2} to 10^{-7} cm^{-1} [115]. For the most part, this is due to the difficulties associated with introducing liquid samples into an optical cavity without a marked loss of sensitivity due to increased scattering and reflection losses from the sample and its container.

A number of different techniques for integrating liquids with optical cavities have been developed. Several of these are illustrated in Figure 2.8, with literature examples and their experimental parameters summarised in Table 2.2.

2.4.1 Filling the optical cavity

In theory, the approach illustrated in 2.8a, in which the analyte solution fills the entire space between the cavity mirrors, should result in the lowest losses and therefore highest sensitivity. In practice, several factors complicate the implementation of this technique: even with short pathlengths, filling the cavity with solvent greatly increases the scattering losses in the cavity; placing liquids in direct contact with mirrors usually lowers their reflectivity due to the altered

Table 2.2: Chronological overview of two-mirror liquid-phase cavity enhanced spectroscopies. l is the optical pathlength, V_{sample} is the total volume of sample required for the measurement, and V_{illum} is the total volume illuminated by the light beam during the measurement. C_{min} is the lowest detectable concentration. Where possible, concentration detection limits have been calculated from three standard deviations (3σ) of the reported baseline noise, but limits marked with * have been estimated using other reported data. C_{min} is converted into the minimum detectable absorption per unit pathlength, κ_{min} using the literature absorption coefficient value for the respective analyte at the appropriate wavelength. CEF is the cavity enhancement factor, the number of passes measured compared to a single-pass experiment.
$^{+}$ calculated from the stated cavity finesse as τ_0 was not stated in this case.

Author	Fig.	Analyte	l / mm	V_{sample} (V_{illum})	C_{min} / nM	κ_{min} / cm^{-1}	CEF
CRDS							
Xu [133]	2.8c	Benzene	10	Few mL	-	2×10^{-7}*	750
Xu [133]	2.8d	Benzene	20	Few mL	-	5×10^{-7}*	428
Hallock [131]	2.8a	Laser dyes	210	50 mL	0.001	10^{-6}	423
Hallock [136]	2.8a	Methylene blue	230	60 mL	-	1×10^{-6}	-
Snyder [137]	2.8c	Quinalizarin	0.30	10 μL (500 nL)	30	6.2×10^{-4}	750
Bahnev [138]	2.8a	Crystal violet	2.0	12 μL (4 μL)	3.75	4.7×10^{-4}	2765
Bechtel [139]	2.8c	Anthraquinones	0.30	10 μL (500 nL)	-	7.8×10^{-6}	1739
Sneppen [140]	2.8a	Azo dyes	2.0	12 μL	15*	4.8×10^{-4}	9369^{+}
Sneppen [141]	2.8a	Direct red 10	2.0	12 μL	17*	5.9×10^{-4}	8487
Sneppen [141]	2.8a	2-nitrofluorene	2.0	12 μL	75*	1.8×10^{-3}	2425
Alexander [134]	2.8e	Malachite green	0.023	-	71	1.6×10^{-2}	848
Sneppen [49]	2.8b	2-nitrofluorene	10	80 μL	40*	9.4×10^{-4}	487
Sneppen [49]	2.8b	Benzopurpurine	10	80 μL	500*	3.7×10^{-2}	142
CEAS							
Fiedler [132]	2.8b	Benzene	1 - 100	$>$ mL	-	9×10^{-6}	10
McGarvey [142]	2.8a	Bacterio-chlorophyll a	1.75	10 μL	0.2	3×10^{-6}	23,000
Islam [143]	2.8b	Brilliant blue-R	2.0	0.9 nL	0.62	5.1×10^{-5}	51
Seetohul [144]	2.8b	Rhodamine B	10	0.07 nL	0.27	1.9×10^{-5}	45
Seetohul [130]	2.8a	Sudan black	200	98 nL	0.018	1.0×10^{-6}	82
Seetohul [130]	2.8a	Methylene blue	200	98 nL	0.0046	2.8×10^{-7}	429
Kiwanuka [145]	2.8b	Rhodamine 6G	54	2.7 nL	0.2	9.1×10^{-6}	-

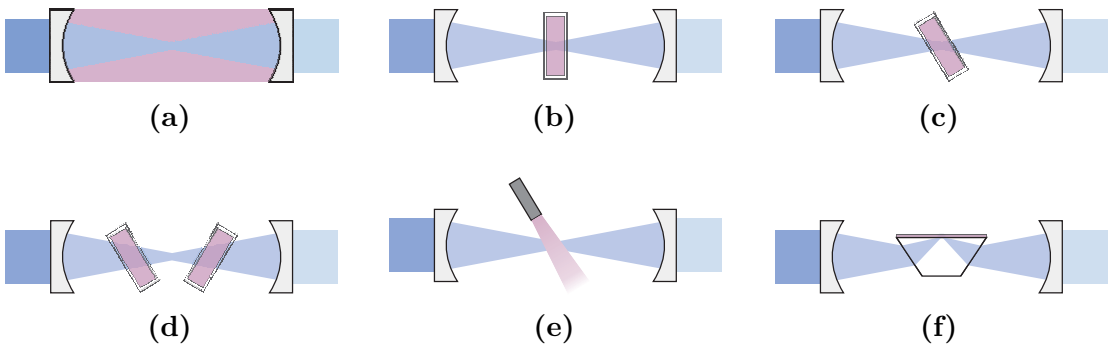

Figure 2.8: A selection of methods of integrating liquid samples with two-mirror optical cavities: a) Entire cavity filled with liquid [131]; b) Optically transparent flow cell inserted at normal incidence [132]; c) Optically transparent flow cell inserted at Brewster's angle [133]; d) Two optically transparent flow cells inserted at Brewster's angle [133]; e) flowing liquid sheet jet [134]; and f) Dove prism with integrated microfluidic channels (evanescent wave probes sample) [135].

refractive index at the mirrored surface; and in the case of harsh chemicals, placing a liquid in direct contact with the mirror coating can lead to chemical degradation and a reduction in reflectivity. Furthermore, as short pathlengths ($\approx$ mm) are required when dealing with small volumes of liquid, CRDS becomes increasingly challenging, as it becomes difficult to measure the short ringdown time accurately. In this regard, CEAS has an advantage when miniaturisation is desired: much shorter cavities can be used, as the time-integrated nature of CEAS means there is no longer a requirement to achieve nanosecond timescale detection.

Despite these complications, the first CRDS experiments utilising the filled-cavity approach reported by Hallock *et al.* [131, 136] demonstrated impressive detection limits on the order of 10^{-6} cm^{-1}. However as relatively long pathlengths were used (>20 cm), large volumes of around 50 mL were required for analysis. In later work, both Bahnev *et al.* [138] and van der Sneppen *et al.* [140, 141] used this approach in a miniaturised cavity with a pathlength of only 2 mm, reducing the cavity volume from millilitres to microlitres. However, due to the shortened length of the cavity, the baseline ringdown time was reduced to around 70 ns, reducing sensitivity.

The reflectivity of a dielectric mirror is dependent on the difference in refractive index between the boundary layer of dielectric coating and the surrounding medium (most reported reflectivities being for the case of air or vacuum):

$$R = \left(\frac{n_0 n_2^{2N} - n_t n_1^{2N}}{n_0 n_2^{2N} + n_t n_1^{2N}} \right)^2 \tag{2.46}$$

where R is reflectivity, N is the number of pairs of layers of different refractive index, and n_0, n_1, n_2, n_t are the refractive indices of the medium of incident light, the alternating media of high and low refractive indices, and the terminating medium at the back of the dielectric mirror, respectively. Placing the mirrors in contact with solution changes n_0, and thus the reflectivity of the mirrors. This can cause particular frustration for CEAS measurements, in which the mirror reflectivity must be accurately known in order to determine absolute absorption coefficients (see Equation 2.40) [132]. Despite this, with proper calibration, it remains possible to make highly sensitive measurements - for example, Seetohul *et al.* reported a detection limit of 2.8 $\times 10^{-7}$ cm^{-1} when filling a 20 cm long cavity with sample, using 99.9% reflective mirrors [130]. However, it should be noted that the reported CEF of 419 is approximately half that expected for 99.9% reflectivity mirrors (CEF = 1000), indicating that contact with the liquid sample reduced reflectivity to $\approx$ 99.8%.

A result of particular note for this approach is the CEF of 23,000 achieved by McGarvey *et al.* in a 1.75 mm cavity [142]. This impressive CEF was achieved due to the use of high reflectivity mirrors (99.998%), in combination with a short pathlength which reduced scattering and absorption losses from the solvent. Again, it should be noted that a CEF of 23,000 is approximately half that which would be predicted from the stated mirror reflectivity, indicating that mirror reflectivity has been reduced through contact with the solution. Despite this, McGarvey moots the possibility of single molecule detection (of bacteriochlorophyll a) if a shorter cavity of around 10 μm were utilised.

2.4.2 Flow cell in a cavity

An alternative technique is to place an optically transparent absorption cell containing the liquid sample into the cavity. This has the advantage of keeping potentially corrosive liquids away from the mirror surfaces, as well as allowing for longer cavity lengths (required for more sensitive CRDS measurements) without requiring an

increase in sample volume. The absorption cell can be introduced either at normal incidence (Figure 2.8b) or at Brewster's angle (Figure 2.8c). At an interface between two media with refractive indices n_1 and n_2, Brewster's angle (θ_B) may be defined as $\theta_B = \tan^{-1} \frac{n_2}{n_1}$. At this angle, there is theoretically no reflection loss for light plane-polarized parallel to the plane of incidence [137]. Thus, if linearly polarised light is used to pump the cavity, it is possible to minimise the loss of light from the cavity caused by introducing an optical element, and thereby maximise the sensitivity of the experiment. However, it should be noted that when an absorption cell is introduced to an optical cavity, there are four additional interfaces that must be considered: refraction and reflection occur at the air/glass, glass/liquid, liquid/glass and glass/air interfaces as light passes through the cell, and it is difficult to achieve Brewster's angle for all of the interfaces simultaneously. Section 3.3 discusses the optimisation of angle of incidence for such systems.

Xu *et al.* reported the first application of CRDS to liquid samples, using both the single (Figure 2.8c) and double (Figure 2.8d) Brewster's cell approach, and achieved an impressive detection limit of 10^{-7} cm^{-1} [133]. Later, Snyder demonstrated this approach using a custom-made flow cell which results in light striking each interface at the correct θ_B [137], achieving a detection limit of 6.2×10^{-4} cm^{-1} in a pathlength of 300 μm. Bechtel *et al.* used the same custom-designed Brewster's angle flow cell, and achieved an improvement in sensitivity (7.8×10^{-6} cm^{-1}) by changing from a pulsed to a more stable continuous wave light source [139].

In some cases, introducing the flow cell at normal incidence may be the preferred approach. For example, a number of CRDS experiments have been designed to improve the sensitivity of high-performance liquid chromatography (HPLC). A change in refractive index of the sample during column elution would cause a corresponding change in Brewster's angle, making a Brewster cell impractical. Using a sample cell at normal incidence allows absorption by the sample to be measured without being perturbed by additional and unpredictable losses arising from changes in refractive index. To counter the increased reflections observed at normal incidence,

van der Sneppen *et al.* used a shorter cavity length of only 4 cm, such that the majority of surface reflections from the cuvette were trapped within the cavity [49].

In the case of CEAS and for broadband measurements, the absorption cell is almost always placed at normal incidence. The unpolarised light sources generally used in CEAS experiments mean that inserting a cell at Brewster's angle for *one* polarity results in a large reduction in light intensity during the first pass as the *other* polarisations are reflected out of the cavity, reducing sensitivity (Equation 2.40). Also, refractive index is a wavelength-dependent property, such that Brewster's angle can only be optimised for a single wavelength. Furthermore, Fiedler *et al.* have previously noted that for incoherent broadband light sources, such as the Xe lamp used in their experiments, the light rays coupling into the cavity have an angular distribution, causing the Brewster angle to be poorly defined, leading to higher losses at Brewster's angle than at normal incidence [132]. Finally, on an experimental note, Brewster's angle of incidence can preclude the use of standard cuvettes, which may not have sufficient width to allow for rays at Brewster's angle incidence to pass through the cuvette front faces without encountering one of the cuvette side walls.

The first example of liquid-phase CEAS provided by Fiedler *et al.* [132] employed a relatively simple modification to a commercial double-beam UV-vis absorption spectrometer, in which two 99% reflectivity mirrors were placed around sample cuvettes with a range of pathlengths from 0.1 to 100 mm. This yielded a CEF of 10. Although the mirror reflectivity would predict at CEF of 100, the CEF is reduced substantially as a result of additional losses caused by the insertion of a cuvette into the cavity. Given that CEF $= \frac{1}{1-R}$, these additional losses can be estimated to be around 9% per pass.

In a later study, Islam *et al.* [143] placed a 2 mm cuvette into cavities at normal incidence, and used mirror reflectivities ranging from 99 to 99.9%. They achieved detection limits ranging from 10^{-5} cm^{-1} to 10^{-3} cm^{-1}, although counter-intuitively it was the lower reflectivity mirrors that provided improved detection limits. This was attributed to the increased CCD integration times required to enhance the poor signal reaching the detector when higher reflectivity mirrors were used. Islam *et al.*

found that increasing the integration time above 100 ms caused the dark noise to increase in a non-linear fashion, owing to the lack of thermoelectric cooling of the CCD array [143], such that the decreased signal-to-noise ratio decreased sensitivity.

An interesting technique demonstrated by Alexander *et al.* achieved detection through the shortest pathlength of sample (only 23 μm), whilst avoiding losses caused by a sample container. This was achieved by utilising a flowing liquid-sheet jet combined with CRDS (Figure 2.8e). However, although only a small volume of liquid is probed by the cavity at any one time, the reservoir volume required to maintain a liquid jet across a cavity is larger than would be confluent with the field of microfluidics.

The final technique illustrated in Figure 2.8, utilises a Dove prism integrated into a two-mirror cavity. The two exterior faces of the Dove prism encountered by cavity light are cut such that light entering each face refracts towards the upper surface where it undergoes total internal reflection, then exits the Dove prism and continues to propagate in the cavity. The evanescent wave generated at the point of total internal reflection can be used to probe samples introduced on the upper surface of the Dove prism, most often through flow cells or microfluidic channels [49]. These techniques have achieved high levels of sensitivity, and are well suited to interrogating small volumes of liquid by virtue of the very short distance over which an evanescent wave propagates from the surface. However, they are fundamentally surface sensitive techniques [2]. This makes them an excellent choice for surface-based studies or for detecting small numbers of molecules by functionalising a surface, but fundamentally insensitive to the bulk liquid, which remains the focus of this thesis. In studies on the effects of magnetic fields on a cryptochrome magnetoreceptor, van der Sneppen *et al.* have demonstrated enhancements over equivalent single-pass measurements of up to 800 using a Dove prism integrated into a microfluidic chip to interrogate fluids at the surface [147].

[2] An exception to this is described in [146], in which the refractive index of the liquid sample causes total internal reflection to occur at the upper liquid/air interface, as opposed to the boundary between the Dove prism and liquid. As such, this allows for probing of the bulk of the liquid sample.

2.4.3 Optical fibre cavities

A variant of the two-mirror approach is to utilise optical fibres to generate an optical cavity. This is attractive because optical fibres are inherently very good at transmitting light and their small size make studying small volumes of liquid a possibility, with picolitre sample volumes having been reported [148]. Experimental set-ups employing optical fibre cavities can be divided broadly into two configurations: a linear configuration (Figure 2.9a) or a loop configuration (Figures 2.9b-2.9c). Linear fibre configurations are directly analogous to two-mirror optical cavities, with confinement of light inside the fibre achieved by mirror-coating [149–151] the ends of the fibre or manufacturing Bragg gratings [152] at the ends of the fibre. Liquid samples are usually studied by stripping a section of the fibre cladding from the fibre core, so that the evanescent field generated at the fibre surface interacts with any liquid sample in close proximity to the exposed section of core, shown in Figure 2.9a.

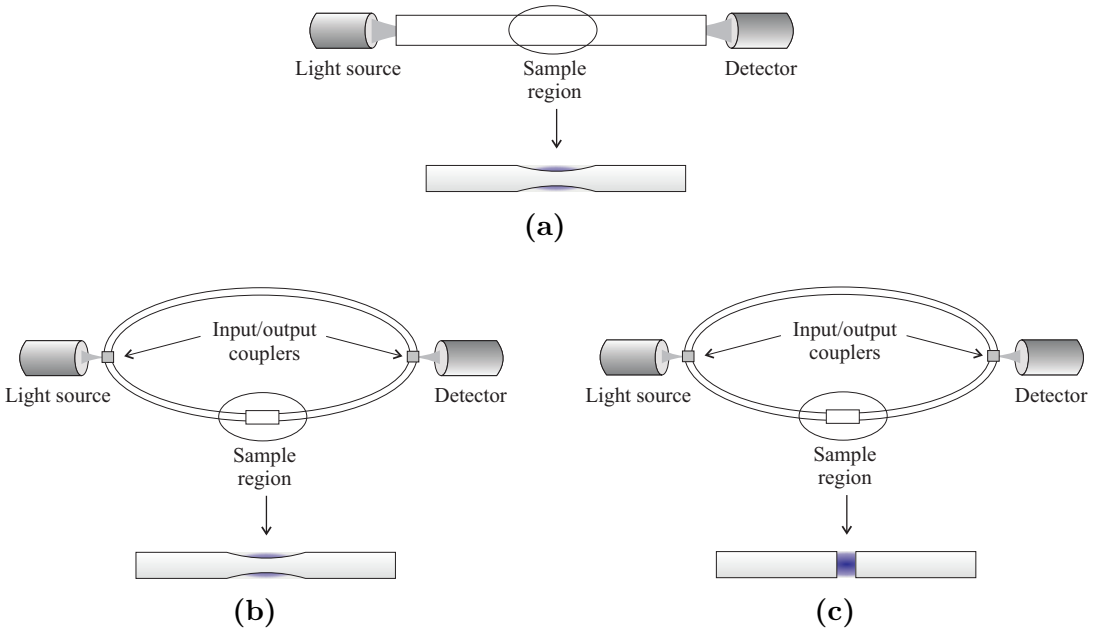

Figure 2.9: Methods of integrating liquid samples with optical fibre cavities: (a) Linear fibre with evanescent wave sensing region; (b) Fibre-loop with evanescent wave sensing region; (c) Fibre-loop with separated fibre ends.

Fibre-loop configurations usually employ a length of fibre with the two ends spliced together. Light can be injected into the fibre-loop cavity through the side of the fibre and the light remains circulating until it is coupled out of the fibre,

or is absorbed by a sample. A liquid sample can be introduced to the cavity by separating the two ends of the fibre by a short distance and immersing the gap in the liquid (shown in Figure 2.9c), although this usually results in extremely large losses from the cavity. An alternative, lower loss method is to use the evanescent field at the surface of the fibre core (shown in Figure 2.9b). Bending the fibre to sharp angles at two places in the loop allows light to be coupled in, and also to be coupled out for measurement. This method is experimentally simple and has the advantage of not requiring the expensive, high quality dielectric coatings normally necessary for the high cavity finesse required for cavity enhanced measurements. The disadvantage is that the losses from the cavity itself are typically on the order of 20%, although this has been reduced to around 8% by integrating the sample, light input and light output into the same region of the fibre [148]. This was done by microfabricating a reflective notch into the sampling region of the fibre to allow facile, tunable coupling of the light into and out of the fibre.

Due to the multiple high loss processes intrinsic to fibre-loop cavity enhanced spectroscopies, cavity enhancement factors and sensitivity are often rather modest (CEF generally <10). Table 2.3 summarises a selection of examples from the literature.

Fibre-loop cavities have also been spliced to liquid core waveguides, discussed in Section 1.3.2, to create a continuous loop with the sample contained within it, achieving a detection limit of 4×10^{-4} cm^{-1} [160].

2.4.4 Whispering gallery mode microcavity resonators

Whispering gallery mode (WGM) resonators are micron-scale optical cavities that confine light to the circumference of a spherical, cylindrical or toroidal resonator through total internal reflection at the inside surface [161]. Their small size results in very small mode volumes ($V \approx 100$ μm) and short pathlengths, leading to highly specific resonance wavelengths (Equation 2.1) [162]. Generally formed from glass microspheres or microtoroids [163], their ultra-high quality factors ($Q \approx 10^8$) enable very long cavity lifetimes and ultra-narrow cavity mode linewidths.

Table 2.3: Chronological summary of liquid-phase fibre-loop CRDS techniques. Tabulated parameters are the wavelength, λ,; the fibre core diameter, d_{fc}; the pathlength l; the volume of liquid probed, V; the minimum detectable concentration, $C_{\min}$; the minimum absorption per unit pathlength, $\kappa_{\min}$; and the cavity enhancement factor, CEF (the number of passes measured compared to a single-pass experiment). Where possible, concentration detection limits have been calculated from three standard deviations (3σ) of the reported baseline noise, but limits marked with * have been estimated using other reported data. Adapted from reference [6].
Unmarked references represent pulsed fibre-loop CRDS. References marked $^+$ represent phase-shift fibre-loop CRDS.
"L" refers to the use of a microlensing system to collimate light over the sensing region and reduce losses.
**DDCI is an abbreviation of the dye 1,1'-diethyl-4,4'-dicarbocyanine iodide. AWS805DS dye is available from American Dye Source, Inc.

Author	Analyte	λ / nm	d_{fc} / μm	l / μm	V / nL	$C_{\min}$ / μM	$\kappa_{\min}$ / cm^{-1}	N_τ
Brown [153]	DDCI**	825	50	3.8	0.0074	250*	100	11
Tong [154]	DDCI**	810	400	47	0.70	200*	67	4
Tong$^+$ [155]	DDCI**	810	400	42	5	30*	10	-
			100	31	0.24	15*	5	-
Li$^+$ [156]	AWS805DS**	810	100	10	0.079	50*	18	2
				25 L	0.20	10*	4	2
Andachi [157]	Methylene blue	660	50	100	0.2	50*	6	2
Waechter$^+$ [158]	Tartrazine	405	200	190	6	5	0.25	3
Waechter$^+$ [159]	Tartrazine	405	400	800 L	100	0.9	0.046	2
Rushworth [148]	Rhodamine 6G	532	400	180	19	0.93	0.11	18

Typically, light is coupled into a WGM resonator by coupling to a tapered optical fibre (see Section 2.4.3). A small amount of light travelling through the optical fibre is coupled out of the tapered region and into the microresonator via an evanescent wave. However, this technique can suffer from large amounts of noise due to mechanical vibrations of the fibre taper, as well as unspecific and random binding of chemical species to the taper, which can interfere with the sensing signal and degrade transmission between the fibre and microresonator [164]. An alternative scheme that mitigates these problems is based on coupling through a prism. A microresonator is placed in close proximity to a prism interface, and light is focussed to a diffraction-limited beam spot at this interface, leading to evanescent coupling [164, 165].

The interaction of light coupled into the WGM resonator with any object within its mode volume is enhanced by a factor proportional to $\frac{Q}{V}$, such that nanoscale objects within the evanescent field of the WGM lead to detectable variations in its spectrum [162]. These variations present as shifts in the wavelength of the resonant mode due to change in the optical pathlength [166, 167] (Equation 2.1), broadening of the cavity mode due to shortening of the cavity lifetime [168, 169], or splitting of the cavity mode due to induced interaction between the two counter-propagating modes around the microsphere/toroid [170, 171].

As the whispering gallery mode propagates around the resonator by total internal reflection, it generates an evanescent field that penetrates a short distance into the surroundings and may interact with species near the resonator surface. WGM resonators are therefore a surface-sensitive technique, in which detection of molecules or nanoparticles relies on selective binding of an analyte to a functionalised surface. This makes WGM resonators highly analyte-specific, although limits the versatility of the technique. Armani *et al.* were the first to report single molecule detection using this method, reporting a sensitivity of 0.1 femtomolar IL-2 protein [172]. The sensitivity of WGM resonators can also be further increased by using plasmon resonance [164]. A plasmonic nanoparticle can enhance the optical field strength at the microcavity surface, amplifying the resonance wavelength shift upon binding of an analyte. For example, Baaske *et al.* used 12 nm $\times$ 12 nm $\times$ 42 nm gold nanorods to achieve sensitivity gains reported to be in excess of several thousand, enabling detection of much smaller nucleic acids and even small intercalating molecules [164]. WGM resonators can also be used as refractive index sensors, with Hanumegowda *et al.* having reported a limit of detection of 10^{-7} RIU [173].

2.5 Chapter summary

In this chapter, we have discussed the characteristics of optical cavities, establishing their respective stability criteria and deriving their mode volumes. From there we derived the equations necessary for CRDS and CEAS, and discussed methods of analysing detection limits. Finally, we explored different techniques for integrating

small liquid volumes with cavity enhanced techniques, providing an overview of literature examples to place the experimental work within this thesis in context.

Given our focus on bulk-sensitive absorption spectroscopy (as opposed to some of the surface-sensitive evanescent-wave techniques discussed in this chapter), in the subsequent chapters we will explore two varieties of liquid integration:

- **Chip-in-a-cavity:** Placing an optically transparent sample container within an optical cavity allows for facile introduction of small liquid volumes into larger macrocavities, but suffers from reduced sensitivity due to increased losses from the additional surfaces of the sample container.
- **Cavity-in-a-chip:** Placing the cavity mirrors within the microfluidic flow channels removes these additional sources of loss, which has the potential to increase sensitivity, but poses significant engineering challenges.

3
Macrocavities

In the previous chapter, we have discussed the theory of optical cavities, the CRDS and CEAS techniques, and methods for integrating liquid samples with these analytical methods. We have also derived the equations necessary to analyse data obtained from these experiments.

This chapter describes initial experiments performed by integrating a 1 mm pathlength flow cell into a two-mirror macrocavity, in order to analyse sub-microlitre liquid samples. A single-wavelength CRDS instrument was constructed and used to determine nitrite concentrations in water (Section 3.1). The key consideration was minimisation of losses caused by the introduction of the flow cell, and use of colourimetric chemistry to enhance absorption coefficients in a wavelength region within the cavity mirrors' range of reflectivity.

3.1 Nitrite detection

The properties of microfluidic systems discussed in Chapter 1 are well matched to the requirements of remote sensing. Remote sensors require high sensitivity, coupled with the capability for rapidly collecting, processing and analysing samples autonomously, all within a small instrument with low power requirements and only requiring small reserves of reagents.

As an example of a remote sensing application, we have chosen the measurement of nitrite concentrations in water courses. Nitrite is a reactive chemical species, and also a micronutrient essential for the growth of phytoplankton. Nitrite levels are an important factor in marine ecology, and in driving global carbon and nitrogen cycles [174, 175]. In the ocean, concentrations vary between 0.1 and 50 μM, but are most often below 0.2 μM [176]. In excess, nitrite is harmful to both humans and aquatic life; the guidelines published by the World Health Organisation (WHO) suggest a maximum concentration of nitrite of 62.5 μM for short term exposure [177], and European Union guidelines set a maximum of 0.22 μM for rivers supporting salmon fisheries [178, 179]. In fact, the WHO lists nitrite as one of the chemicals presenting the greatest health concern in some natural waters [177]. Excess nitrite is implicated in methemoglobinemia (colloquially known as "blue baby syndrome"), and in the production of several known carcinogens [180].

Table 3.1: Concentrations of nitrite in different aquatic environments. Maximums refer to WHO guidelines.

Water sample	Typical [Nitrite] / μM	Maximum recommended [Nitrite] / μM
Tap water	-	62.5
Rivers	-	0.22
Oceans	0.1 - 50	-

Remote sensing platforms, such as the Argo float programme [181, 182] are already prolific, with thousands of floats distributed throughout the world's oceans, providing power, positional monitoring, and the machinery to descend to depths of around 2 km to gather depth-stratified samples. The floats have on-board systems for measuring properties such as temperature, pH and salinity, but as yet, chemical detection sensors have proved relatively impractical due to their size and the reservoirs of reagents often required. A true μTAS microfluidic device that could perform all of the sample processing, separation and spectroscopy required to detect nitrite would be ideally suited to such applications, and would allow remote three-dimensional mapping of the oceans.

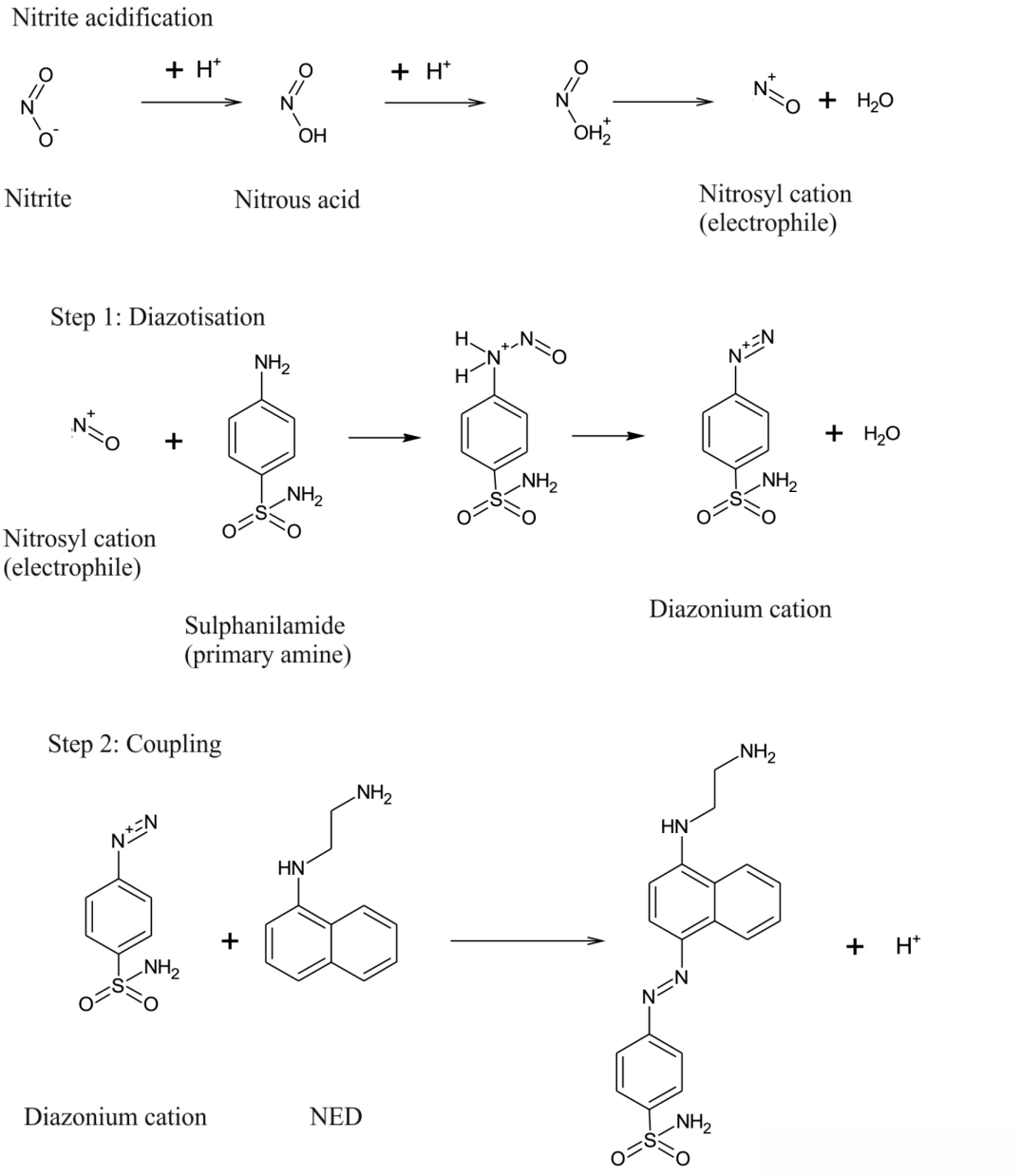

Figure 3.1: Formation of the azo dye product in the Griess assay.

Nitrite (and nitrate, its oxidised form) sensing has been the subject of four relatively recent reviews [111, 183–185]. Of the spectroscopic methods used to detect nitrite, the Griess assay is the most common [186]. The assay is based on a colourimetric reaction (see Figure 3.1) that selectively converts nitrite into a highly absorbing diazo compound. The reaction involves acidifying the nitrite so that it forms the nitrosyl cation, which goes on to diazotise by reaction with a primary amine. The resulting diazonium salt reacts with an aromatic compound to form

an azo dye which, in aqueous solution, has an absorption maximum at 520 nm of around 80,000 M^{-1} cm^{-1}. The absorption spectrum for the diazo product of our variant of the Griess assay is shown in Figure 3.2. The nitrite in the sample is converted quantitatively in a one-to-one ratio into the strongly absorbing azo dye, as long as the assay reagents are in excess of the nitrite in the sample (for trace nitrite detection, this will always be the case). Thus, by monitoring the reaction using spectrophotometry, measurement of the nitrite concentration can be made.

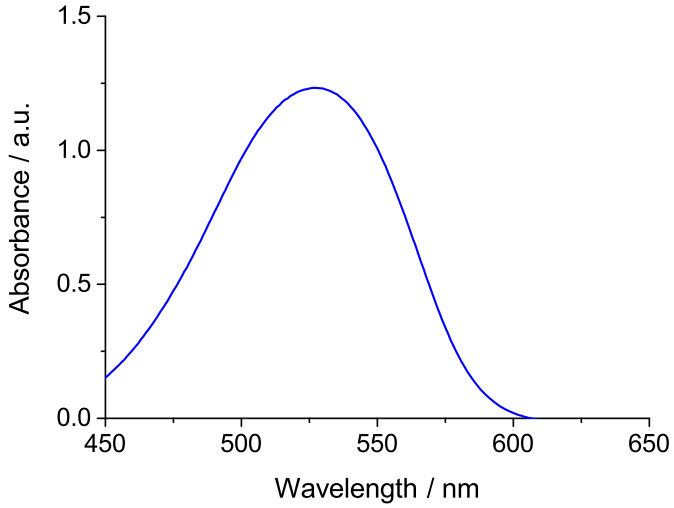

Figure 3.2: The absorption spectrum of the pink azo dye product of the Griess reaction, measured in a commercial UV-vis spectrometer.

The popularity of the Griess assay is due to the high nitrite-specificity of the diazotisation, and the high sensitivity that can be achieved due to the dye's large peak absorbance. As a result, samples can be analysed on-line without any pre-treatment.

There are several variants of the Griess assay, optimised for different detection wavelengths; the reagent used in this work was prepared as reported by Sieben *et al.* [18], and produces a pink azo dye with strong absorption at 532 nm (the wavelength of our laser). Figure 3.1 shows a schematic of the reaction mechanism. The rate limiting step is the internal rearrangement required to form the diazonium ion [187]. In all experiments, we ensure that sufficient time is allowed for the reaction to complete before analysing samples.

3.2 532 nm CRDS cavity set-up

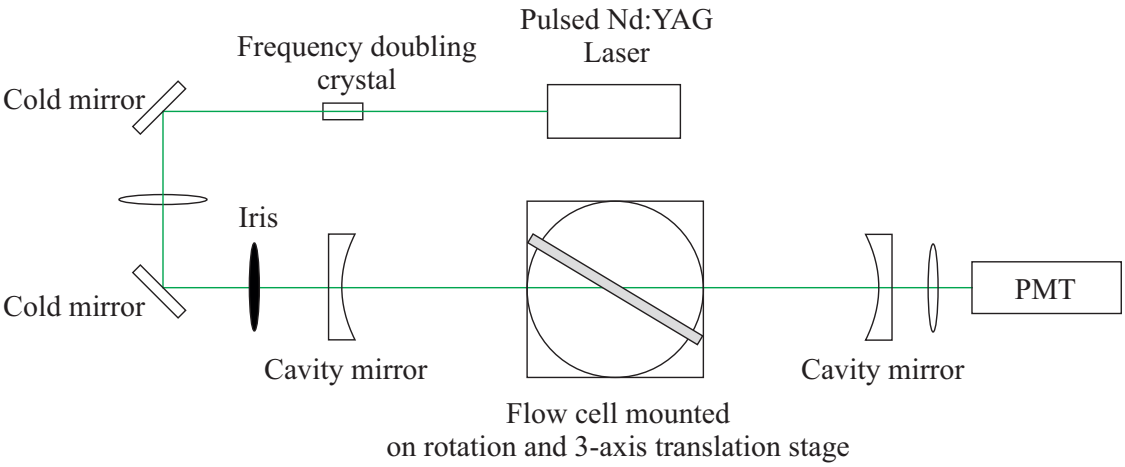

Figure 3.3: Schematic of the experimental set-up used to detect nitrite in an optical macrocavity. PMT refers to a photomultiplier tube. Unlabelled optics are lenses.

The monochromatic light source employed for our single-wavelength CRDS measurements is a microchip Nd:YAG laser (Teem Photonics, NP-10620-100, producing 0.9 ns, 6 μJ pulses with a repetition rate of 7.4 kHz). The 1064 nm light from the laser is passed through a frequency-doubling BBO crystal to produce 532 nm light. This is separated from the fundamental by steering the beam into the cavity with two cold mirrors, which reflect 532 nm and transmit 1064 nm. A focussing optic is used to bring the beam to a focus at the midpoint of the symmetric optical cavity. The laser is passively Q-switched, such that laser pulses cannot be externally triggered; we use a signal from a photodiode that detects a fraction of the laser pulse scattered from the frequency doubling crystal to trigger the rest of the experiment from the laser pulse.

The optical cavity is formed from two 25 mm concave dielectric mirrors (CVI Melles Griot, radius of curvature 1 m, reflectivity $\approx$ 99.8% at 532 nm). The mirrors are positioned 51.3 cm apart. As the laser pulse duration is shorter than the cavity round-trip time, the signal observed consists of a train of pulses with exponentially decaying intensities.

The light that is coupled out of the second cavity mirror is diffused by a short focal-length lens over the entire sensing region of a photomultiplier tube (PMT,

Hamamatsu H6780-20). The signal amplification of a PMT is not homogenous across the entire light-sensitive region, so small deviations in the position of a collimated beam can lead to intensity fluctuations; diffusing the beam across the entire detector reduces this source of variance. The signal from the PMT is displayed on a digital oscilloscope (LeCroy, SDA 6020), which has a vertical resolution of 11 bits and a time resolution of 20 picoseconds. The high bit depth ensures that peak heights can be accurately resolved, even with weak signals, and time resolution becomes limited only by the detector (which has a rise time of 780 ps).

The oscilloscope is interfaced to a personal computer (PC) via an ethernet link to allow fast data transfer, and the waveforms are acquired by a LabVIEW (National Instruments) program, which also performs the data fitting and peak analyses on-the-fly. Fifty ringdown signals were averaged on-board the oscilloscope before being transmitted to the PC, as this matched the acquisition and data transfer rates. An Allan variance measurement [188] was then performed using the blank cavity, with minimum variation observed when averaging around four hundred oscilloscope-averaged waveforms, as shown in Figure 3.4a. A decision was made to average only two hundred oscilloscope-averaged waveforms, as the difference in variance was small, but the acquisition time for an experimental run was reduced by a factor of two. Overall, this results in 10,000 laser shots being averaged for each measurement. An example ringdown trace is shown in Figure 3.4b.

A commercial high optical-quality quartz flow cell with a 1 mm channel depth (Starna Scientific Ltd. 45/Q/1) is positioned in the centre of the cavity on a double-rotation (Thorlabs, RP01) and three-axis translation stage (Newport Corporation, 443), equipped with micrometer resolution actuators (Newport Corporation, SM-25). This provides full control over the position and angle of the flow cell within the cavity, allowing optimisation of these parameters to minimise cavity losses, yielding the longest possible ringdown time. Liquid was delivered to the flow cell using a syringe pump (Chemyx, Fusion 400).

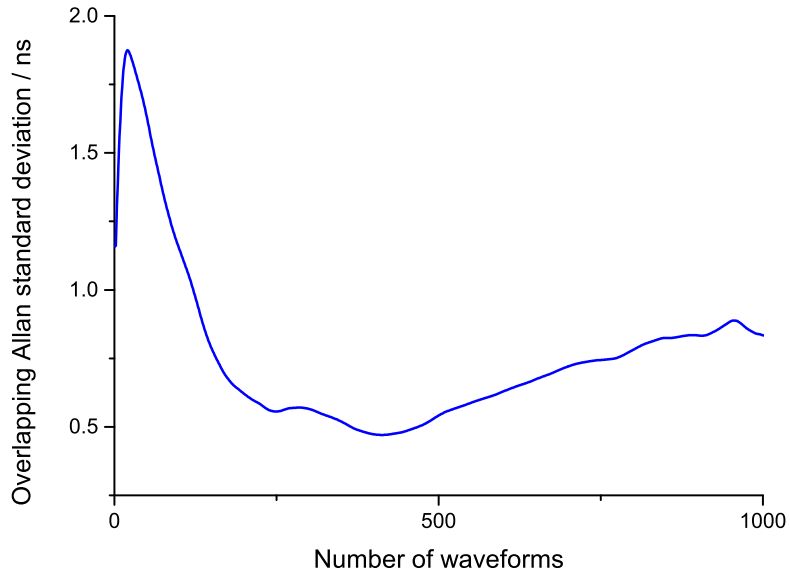

(a)

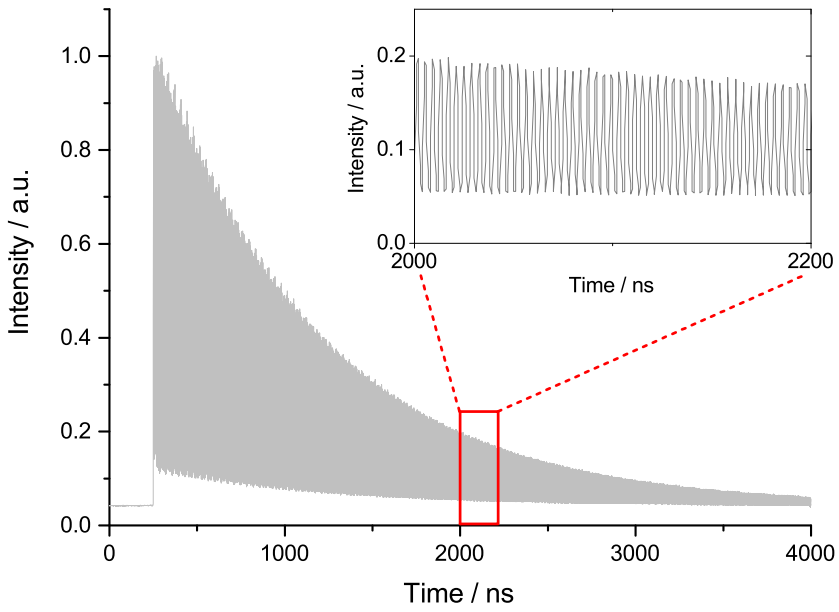

(b)

Figure 3.4: (a) A plot of Allan standard deviation against number of waveforms averaged; (b) A typical ringdown signal for an empty cavity. Inset illustrates resolved train of pulses.

3.3 Integrating a flow cell into an optical cavity

As stated in Section 2.4.2, if a plane-polarised light source is used (such as our microchip laser), it is possible to minimise reflective losses from a surface introduced into an optical cavity by positioning it at Brewster's angle. However, it is impossible to achieve Brewster's angle for a flow cell with parallel surfaces, as there are four separate interfaces to consider. For a given angle, the amount of light transmitted through each of the four interfaces shown in Figure 3.5 can be calculated using the relevant Fresnel equation for plane polarised light:

$$T_{\mathrm{p}} = 1 - \left[\frac{n_1\sqrt{1-(\frac{n_1}{n_2}sin\theta_{\mathrm{i}})^2} - n_2 cos\theta_{\mathrm{i}}}{n_1\sqrt{1-(\frac{n_1}{n_2}sin\theta_{\mathrm{i}})^2} + n_2 cos\theta_{\mathrm{i}}}\right]^2 \tag{3.1}$$

where n_1 and n_2 are the refractive indices of the two components of the interface and θ_{i} and θ_{t} are respectively the angles of incidence and transmission from the normal. The product of the fractions of light transmitted at each interface gives the total proportion of incident light which is transmitted. Finding the angle for which this total is maximum gives the optimum angle for insertion.

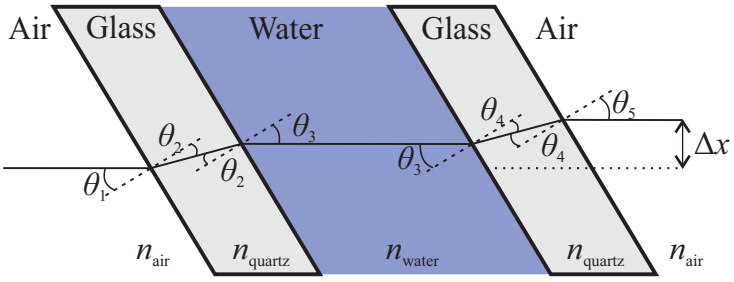

Figure 3.5: The transmission and refraction of light passing through an angled flow cell.

For the first interface, θ_{i} is simply the angle of the flow cell relative to normal incidence, but for all subsequent interfaces, the angle of incidence is equal to the angle of transmission, θ_{t}, for the previous interface. θ_{t} for an interface can be calculated from Snell's Law:

$$\frac{n_1}{n_2} = \frac{\sin\theta_{\mathrm{t}}}{\sin\theta_{\mathrm{i}}} \tag{3.2}$$

A plot of the predicted transmission versus θ_1 is shown in Figure 3.6, for $n_{\text{air}} = 1.00$, $n_{\text{quartz}} = 1.46$, $n_{\text{liquid}} = 1.33$. In this case the optimum angle is 55.8°, with a reflection loss of only 0.09%. Placing the flow cell at this angle to the cavity axis increases the pathlength through the liquid from 1 mm to 1.27 mm. This is in close agreement with the value of 1.23 mm found from a calibration experiment for an identical cell performed by a previous group member [6].

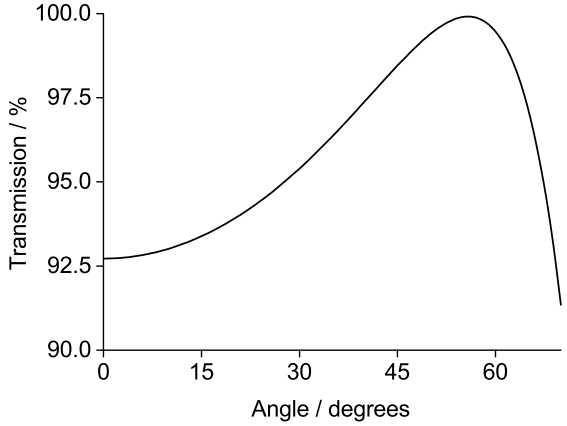

Figure 3.6: Plot of predicted transmission against angle of incidence, θ_i, generated by iterative use of Equations 3.1 and 3.2.

In addition to reflective losses, any optical imperfections in the region probed by the laser will increase scattering losses, reducing sensitivity. These losses are minimised by using high-optical-quality flow cells, and any dust or smears are removed from the external surfaces of the cell by thoroughly cleaning the cell prior to insertion into the cavity. The internal surfaces are cleaned by flushing solvent through the cell for several minutes before taking any measurement. Finally, once the angle of incidence has been optimised, the flow cell is typically translated in both axes perpendicular to the cavity axis to maximise the ringdown time, and hence find the optimum point of incidence on the cell.

It should be noted that in addition to reflection and scattering losses, by aligning the surface of the cell away from normal incidence, we introduce losses from refraction, as light undergoes a sideways displacement in the plane of polarisation, illustrated in Figure 3.5 as Δx. This can be accounted for in monochromatic experi-

ments by offsetting the second cavity mirror from the first in the plane of polarisation, such that the displaced beam still impinges on the second mirror at the centre.

Before insertion of the 1 mm flow cell into the cavity, the ringdown time of a 532 nm light pulse was measured to be 802 ns. This corresponds to a mirror reflectivity of 99.786%, close to the manufacturer's specification of 99.8%. The average ringdown time for a cavity with a 1 mm flow cell angled at 55.8° to the cavity axis and filled with distilled water was determined to be 312.5 ns. Using Equation 2.32 the loss per pass associated with the flow cell can be quantified, and is found to be around 0.33%. At this angle, we would expect total losses from Fresnel reflections to be only 0.08%, suggesting that losses due to imperfections in the flow cell are around 0.25%.

3.4 Experimental

All reagents were purchased from Sigma-Aldrich and used without further purification. However, as previous experiments in the group had been hampered by high (and varied) concentrations of nitrite in the "blank" samples [6], a number of steps were taken to limit contamination. All glassware and sample handling apparatus were leached with 2M HCl overnight before use, then rinsed thoroughly with MilliQ water. When not in use, all solutions and sample containers were sealed to form a closed system, as work by Yao *et al.* noted that samples left exposed to air in laboratories overnight acquired nitrite concentrations between 73 and 170 nM [189]. Finally, as the purest distilled water source available was a communal MilliQ water purification system (introducing potential for contamination from other experiments), all experiments were performed using the same batch of distilled water.

A stock solution of "Griess reagent" was prepared and used for all samples. 0.5 g of sulphanilamide (S9251, Sigma-Aldrich) was dissolved in 50 mL of MilliQ water and 5 mL of concentrated hydrochloric acid (96208, Sigma-Aldrich) in a 500 mL volumetric flask. 0.05 g of N-(1-napthyl)ethylene diamine dihydrochloride (33461, Sigma-Aldrich) was added and the volume made up to 500 mL with MilliQ water.

A series of standard solutions of nitrite were made by serial dilution of a stock 1 M solution of sodium nitrite (35271, Sigma-Aldrich). Nine concentrations between 0.05 μM and 5 μM were mixed in a 1:1 ratio with the stock Griess reagent and left to develop for at least ten minutes. A "blank" solution was also made by mixing MilliQ water in a 1:1 ratio with the stock Griess reagent. The blank ringdown time, τ_0, was monitored between each sample to ensure that the flow cell had been completely flushed. The solutions were flowed through the quartz flow cell using a sterile syringe and the two hundred waveforms were acquired and averaged in the LabVIEW program.

These solutions were also analysed in a commercial UV-vis spectrometer (Varian, Cary 100 Bio UV-vis) in 1 cm polystyrene cuvettes for comparison.

3.5 Results

The single-pass data collected using a commercial UV-vis spectrometer is presented in Figure 3.7. Figure 3.7a shows absorption spectra recorded for different nitrite concentrations. Figure 3.7b shows a plot of absorption at 532 nm versus nitrite concentration, the gradient of which yields a natural absorption coefficient for the azo dye product of the Griess assay of 90400 ± 590 M^{-1} cm^{-1} at this wavelength.

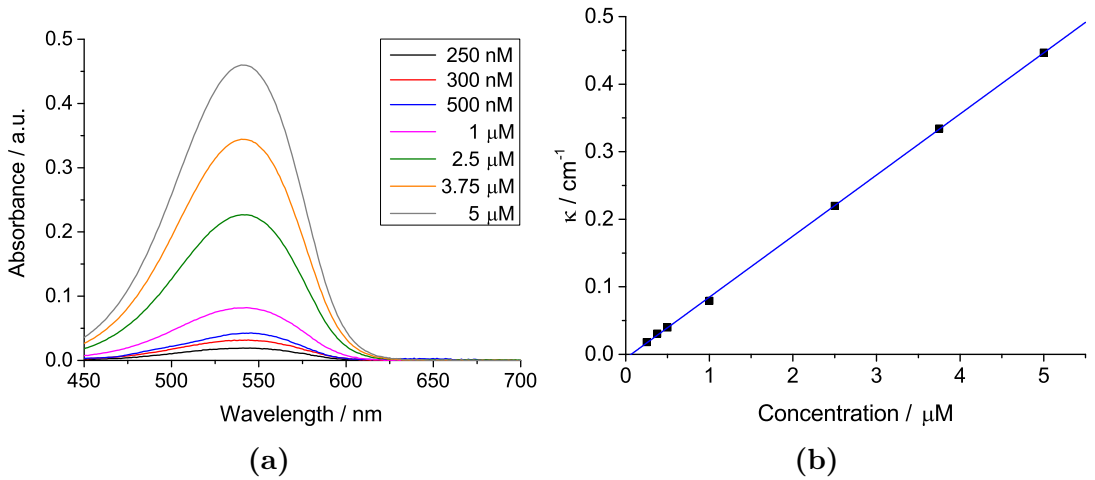

Figure 3.7: (a) A plot of absorption against wavelength for different nitrite concentrations 0.25 - 5 μM, determined in a commercial UV-vis spectrometer; (b) A plot of κ against concentration. The gradient of the graph is 0.0904 μM^{-1} cm^{-1}, which equates to 90400 M^{-1} cm^{-1}.

As described in Section 2.3.3.1, there are two methods of determining the detection limit of a spectroscopic measurement system: the 3σ error in repeated measurements of the blank light intensity (I_0) at 532 nm yields a minimum detectable absorption per unit pathlength of $\kappa_{\mathrm{min,s}} = 3.80 \times 10^{-3}$ cm^{-1}; whereas the 3σ error in the y-intercept of Figure 3.7b yields $\kappa_{\mathrm{min,r}} = 4.58 \times 10^{-3}$ cm^{-1}. Given the determined absorption coefficient, these correspond to a minimum detectable concentration of $C_{\mathrm{min,s}} = 42$ nM and $C_{\mathrm{min,r}} = 51$ nM in a 1 cm cell. Although, as discussed in Section 2.3.3.1, we would expect the regression-based detection limit to be larger as it includes all sources of error, the relatively small disparity between these two figures indicates that the decontamination protocols adopted in this experiment have removed a large degree of the variable nitrite contamination observed within previous work in the group [6].

In the CRDS measurements the value of κ was calculated using Equation 2.32 for each concentration using the previously determined single-pass pathlength, l of 1.27 mm. These values of κ were plotted against concentration, and the gradient yields a natural absorption coefficient of 90500 ± 1740 M^{-1} cm^{-1}. This value is in close agreement with the value of 90400 ± 590 M^{-1} cm^{-1} measured in the UV-vis spectrometer, supporting the single-pass pathlength calculated from the angle of incidence.

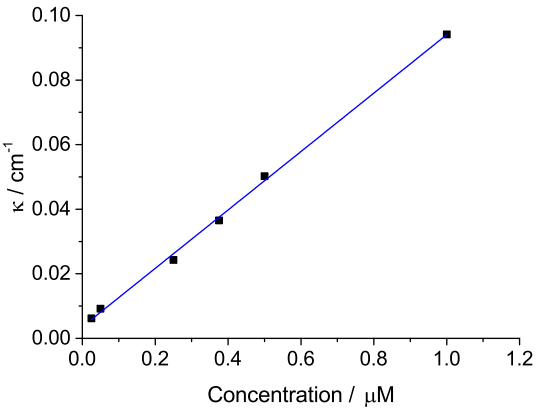

Figure 3.8: A plot of κ against concentration as measured by CRDS. The gradient of the graph is 0.0905 μM^{-1}, which equates to 90500 M^{-1} cm^{-1}.

The spectroscopic limit of detection for the macrocavity setup was determined by repeatedly measuring the ringdown time of the blank solution between each

sample measurement. The cavity length, d, was 51.3 cm, the single-pass pathlength through the sample, l, was 1.27 mm, the average ringdown time for all of the blank measurements, τ_0, was measured as 290.70 ns and the standard deviation of the measurements was 2.47 ns, giving $\Delta\tau_{\text{min}} = 7.41$ ns (three standard deviations). Using Equation 2.42 gives $\kappa_{\text{min,s}} = 8.00 \times 10^{-4}$ cm^{-1} corresponding to a minimum detectable concentration $C_{\text{min,s}} = 8.83$ nM for this pathlength.

The standard error in the y-intercept was 8.53×10^{-4} cm^{-1}, yielding $\kappa_{\text{min,r}} = 2.56 \times 10^{-3}$ cm^{-1}. Given the determined absorption coefficient, this corresponds to a minimum detectable concentration $C_{\text{min,r}} = 28.5$ nM for this pathlength. Again, as discussed in Section 2.3.3.1, the larger value is expected for the value calculated by regression, and is likely to be due to errors in making up the concentrations accurately. Additionally, despite our decontamination protocols, there is likely to be a non-zero concentration of nitrite in the MilliQ water.

If we assume that absorption from the reagents in the Griess assay can be entirely neglected, the concentration of nitrite in the "blank" Griess reagent can be estimated by comparing the average ringdown time when the flow cell is filled with the blank Griess reagent (290.70 ns) with that when the flow cell is filled with deionised MilliQ water (312.50 ns), using Equation 2.32. This yields a blank concentration of nitrite of 35 ± 10 nM. This is significantly lower in magnitude and variation than was found during previous work carried out both within our research group [121] and by Yao *et al.* [189], suggesting that our decontamination protocols have been moderately successful.

Since the cavity is so large, and the flow cell is positioned in the centre of the cavity, the detection volume can be approximated as a cylinder (Equation 2.6) with a radius equal to the beam waist, calculated from Equation 2.4. This gives an illuminated volume of 74.6 nL. Using the spectroscopically calculated minimum detectable concentration of 8.83 nM, this corresponds to a limit of detection of 4.12×10^8 molecules.

Given the average ringdown time for the blank solutions, $\tau_0 = 290.70$ ns, as shown in Section 2.3.3.4 the cavity enhancement factor for this cavity can be shown to be 170.

Table 3.2 summarises the detection limits achieved. For ease of comparison and in the context of evaluating techniques for *low volume* liquid analysis, it is useful to convert $C_{\min}$ for the UV-vis spectrometer to that predicted for a 1.27 mm pathlength.

Table 3.2: A summary of the limits of detection for each of the measurements made on the Griess assay samples. The minimum detectable concentration is calculated for a 1.27 mm pathlength through the sample for comparison.

Method	$\kappa_{\min}$ / cm^{-1}	$C_{\min}$ / nM	Number of molecules	CEF
UV-vis regression	4.58×10^{-3}	402	-	1
UV-vis spectroscopic	3.80×10^{-3}	330	-	1
CRDS regression	2.56×10^{-3}	28.5	1.33×10^{9}	170
CRDS spectroscopic	8.00×10^{-4}	8.83	4.12×10^{8}	170

3.6 Discussion

The results detailed in the previous section illustrate that our CRDS experiment provides sufficient sensitivity to detect nitrite at the nanomolar ambient concentrations listed in Table 3.1, utilising a channel depth of only 1 mm. Thus, this proof-of-concept experiment implies that CRDS measurements can provide a useful analytical tool for microfluidic devices. It is helpful at this point to compare our CRDS measurement with other techniques for sensing nitrite. Table 3.3 summarises a selection of literature examples and their experimental parameters.

It can be seen that detection limits in the nanomolar concentration range are readily achieved with optical pathlengths of a few centimeters, whilst the longer pathlengths provided by liquid core waveguides (LCWs, see Section 1.3.2) are required for sub-nanomolar detection limits. Although LCWs provide an attractive approach, achieving high sensitivity with relatively small volumes of analyte, they suffer from high blank signals, significant dead volume at the light coupling region, and measurements are prone to disruption from micro-air bubbles that tend to form

Table 3.3: Chronological overview of nitrite detection using the Griess assay. l is the optical pathlength in mm, V_{sample} is the total volume of sample required for the measurement, and V_{illum} is the total volume illuminated by the light beam during the measurement. C_{min} is the lowest detectable concentration of nitrite. Where possible, concentration detection limits have been calculated from three standard deviations (3σ) of the reported baseline noise. Values left blank were not reported.
LCW is an abbreviation of liquid core waveguide.
70×Preconc. refers to a preconcentration by factor of 70.

Reference	Notes	Location	Optical l / cm	V_{sample} (V_{illum}) / mL	C_{min} / nM
Raimbault [190]	-	Shipboard	5	5	1.24
Yao [189]	LCW	Lab	450	2 (1.1)	0.5
Greenway [191]	On-chip	Lab	-	-	200
Zhang [192]	LCW	Shipboard	200	0.5	0.1
Manzoori [193]	70×Preconc.	Lab.	1	500	3.8
Steimle [194]	LCW	*In situ* (500 m depth)	100	(0.52)	2.5
Adornato [195]	LCW	*In situ* (200 m depth)	97	(0.5)	1
Patey [111]	LCW	Shipboard	200	-	1.5
Sieben [18]	On-chip	Lab	2.5	0.08	14
Beaton [20]	On-chip	*In situ* (1 m depth)	2.5	0.25	15
Rushworth [6]	CRDS	Lab	0.123	1 (196 nL)	1.9
Czugala [196]	On-chip	Lab (portable)	2.4	0.037	740
Liu [197]	On-chip	Lab	1.2	1.5	20
This work	CRDS	Lab	0.127	0.4 (74.6 nL)	8.83

on the internal surfaces of the LCW, disrupting total internal reflection and thus causing fluctuations in measured absorbance. For measurements able to tolerate a slightly poorer detection limit, CRDS measurements provide a long effective pathlength whilst maintaining a short physical pathlength, and avoid most of the problems associated with LCWs.

Sample preconcentration is a relatively facile method of improving detection limits in a laboratory environment [193], but requires large sample volumes, and adds sufficiently to system complexity and power requirements that it is often impractical for *in situ* devices.

The second column of Table 3.3 indicates the location of operation: laboratory-based experiments, shipboard-based experiments, and *in situ* measurements. As

demonstrated by the contamination of blanks in our experiments, when quantifying nitrite, it is often the sample integrity rather than sensitivity that is the issue. By performing analysis *in situ*, sample integrity is more easily maintained. Moving from a laboratory environment towards *in situ* detection places increased engineering requirements upon a detection system: miniaturisation, reduced power consumption, increased system stability, and automation are all required of a system to be deployed for autonomous remote sensing.

3.7 Chapter summary

In this chapter, a single-wavelength CRDS experiment was constructed and applied to the field of nitrite detection in aqueous samples. An 8.83 nM detection limit was achieved using a 1 mm depth flow cell, angled to minimise the additional Fresnel reflections encountered when introducing a sample container to an optical cavity. These losses were quantified as 0.33% loss per pass.

Clearly, despite achieving detection limits appropriate for sensing nitrite at ambient levels in water courses, with a 51.3 cm macrocavity requiring careful alignment, a mains-powered microchip Nd:YAG laser as the light source, and high-performance oscilloscope required for high-speed acquisition, this experiment is not currently confluent with either a μTAS or remote sensing environment. Packaging a cavity enhanced detection scheme into a sensor that can be automated and operated *in situ* is the next challenge in demonstrating the applicability of cavity enhanced techniques for seawater analysis (and other remote sensing applications). Chapters 4 through 7 will explore the potential for miniaturisation of our detection scheme, as well as attempting to enhance sensitivity by removing losses due to the sample container through integration of the cavity mirrors into the liquid channel (a so-called "cavity in a chip" configuration).

4
Cavity-in-a-chip

Having achieved modest cavity enhancement factors in the previous chapter, using flow cells integrated into a macroscopic optical cavity, we have demonstrated that the additional surfaces of the flow cell are the largest source of loss of light from the cavity, and thus the greatest barrier to enhanced sensitivity. In addition, the large footprint of a macroscopic cavity is incongruent with the aims of a μTAS device. For these reasons, an alternative experimental setup was devised in which the cavity mirrors are integrated into the microfluidic channel during fabrication. This chapter discusses the production of these cavities, and the evaluation of their optical properties through absorption measurements.

4.1 Chip design and manufacture

For the purposes of this investigation, we utilised custom-made microfluidic chips with integrated cavity mirrors. These were designed and fabricated by a collaborator from the University of Southampton, Dr. Cathy Rushworth, and provided for the experiments described here to evaluate their suitability for chemical sensing. All microfluidic chips were manufactured in a Class 1000 (ISO 6) cleanroom to reduce the number of particulate contaminants that are incorporated during the curing process, which would lead to high scattering losses.

The chip fabrication is discussed in detail in [198], and summarised below. The optical cavity is formed from commercially available 3M Vikuiti^{TM} enhanced-specular-reflector II (ESRII) film. ESRII film is a 32 μm thick multi-layer polyester film, and exhibits >98% reflectivity across the visible spectrum [199]. At 532 nm, the wavelength of our light source, the reflectivity is reported as 99.7%. To prevent chemical degradation of the mirrors, a thin layer of polydimethylsiloxane (PDMS) is incorporated between the mirrored surface and the fluid channel, as illustrated in Figure 4.1b. PDMS is an optically clear polymer often used in microfluidic chip fabrication.

To produce the microfluidic channel, an inverse master of the channel design was created on a 10 cm diameter glass wafer, the process of which is shown schematically in Figure 4.1a. First, SU-8 photoresist (Microchemicals GmbH, SU-8 3050) was applied to the glass wafer, and it was spun at 3000 rpm for 30 seconds to achieve an even coating. After baking [200] for several minutes to create a slightly hardened layer, an acetate photomask was used to define the channel design, and the SU-8 was exposed to a UV dose of 400 mJ cm^{-2} (EVG, EVG620TB). The master wafer was then baked again and placed in SU-8 developer (Microposit EC solvent) to remove the uncured SU-8. For our experiment, it is important that the surfaces of the microfluidic channel are flat, with well defined edges, else the optical cavity finesse is greatly reduced. Figure 4.1c shows the profile of the SU-8 photoresist after curing (measured using KLA Tencor, Alpha-Step): the channel height is 47.3 μm $\pm$ 0.33 (3σ), and the width of the channel is 500 μm. The total volume of the fluid channel is approximately 1 μL.

PDMS (Dow Corning, Sylgard 184) was prepared by mixing the monomer and radical-initiator curing agent in a 10:1 mass ratio, and degassing in a desiccator under vacuum for 30 minutes. The liquid PDMS was then applied to the master wafer and spun at high speed to form a thin, even layer, which was then baked to form the cured polymer. The PDMS was carefully peeled from the master wafer and 1 mm fluid access holes were punched to create inlet and outlet regions. Similar unfeatured layers of PDMS were formed over the cavity mirrors, with a thicker

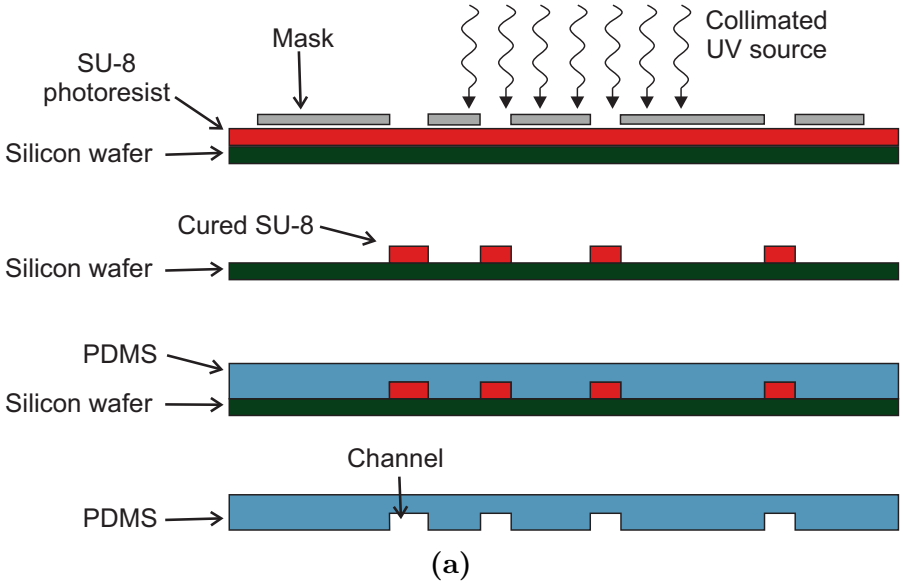

(a)

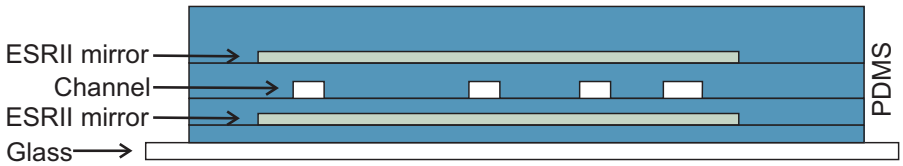

(b)

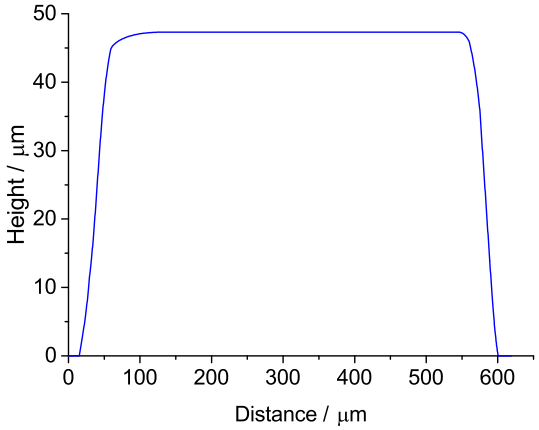

(c)

Figure 4.1: (a) Fabrication of microchannels in PDMS using an SU-8 inverse master of the channel design; (b) Side profile schematic of completed microfluidic chip (not to scale); (c) Height profile of the SU-8 inverse master for the channel, giving a channel height of 47.3 μm $\pm$ 0.33 (3σ error).

layer on one face of the microfluidic chip to allow for the attachment of inlet and outlet fluid connectors. A 200 μm glass cover slip was used on the opposite face to provide additional rigidity and stability (Figure 4.1b).

The separate layers were placed in a oxygen plasma asher (Diener Electronic GmbH, FEMTO) and oxidised for 30 seconds. This "activates" the glass and PDMS surfaces by generating hydroxyl (-OH) functional groups that undergo a condensation reaction when two surfaces are pressed together firmly and baked at 80 °C for 15 minutes, covalently bonding the two layers. By using layers of ESRII mirror film significantly wider than the channel dimensions, positioning of the layers becomes relatively facile. The cavity length, defined by the distance between the two faces of the ESRII film, was estimated to be 200 μm.

4.2 Experimental

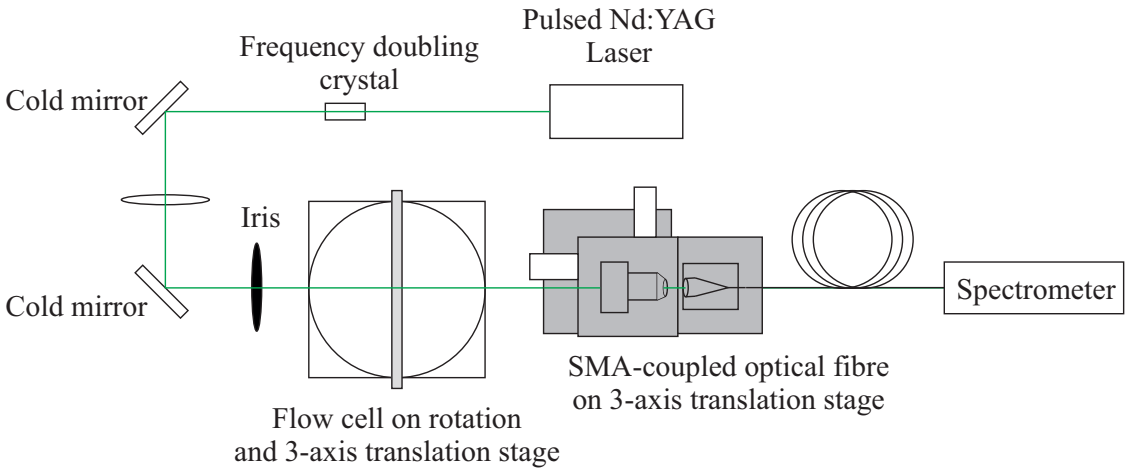

Figure 4.2: A schematic of the experimental setup used to detect Thymol Blue in a microfluidic chip with integrated optical cavity mirrors.

A 200 μm cavity length would result in a sub-nanosecond ringdown time (Equation 2.30), which is well beyond the capabilities of our detection electronics. Instead, CEAS was employed for this experiment, as the time-integrated nature of the measurement simplifies the experimental setup. Although the ESRII mirrors have a wide reflectivity bandwidth, to avoid any complications from achromatic transmission through the prototype microfluidic chip in this initial proof-of-concept

experiment, we placed the chip at normal incidence and employed a monochromatic light source: a microchip Nd:YAG laser (NP-10620-100, Teem Photonics, producing 0.9 ns, 6 μJ pulses with a repetition rate of 7.4 kHz). The 1064 nm light from the laser is passed through a frequency-doubling crystal to produce 532 nm light. This is separated from the fundamental by steering with two cold mirrors, which are also used for beam steering through the microfluidic channel, and a 532 nm bandpass filter. A focussing optic is used to collimate the laser output.

Light is coupled from the cavity into the detector using a 400 μm core multimode fibre (Thorlabs, FT400EMT). A USB spectrometer (Ocean Optics, HR4000) was used to wavelength resolve the output, allowing us to detect and correct for any residual fundamental and/or ambient light reaching the detector. The spectrometer is interfaced to a PC via USB 2.0, and spectra are acquired by a home-written LabVIEW (National Instruments) program, which also performs the data fitting. Spectra can be collected individually or continuously acquired. The readout rate of the spectrometer is 20 Hz and the integration time can be set from 3.8 ms to 10 s. A series of Allan variance measurements [188] were performed using the blank cavity, with minimum variation observed when integrating for 100 ms, and averaging 50 sequential spectra within the LabVIEW program. Overall, this results in 37,000 laser shots being averaged for each measurement.

To reduce the impact of changes in ambient light on the experiment, a blackout box was constructed around the experiment. In addition, a "dark" background measurement was recorded with the laser switched off, using the same spectrometer settings, and this measurement was subtracted from all subsequent spectra by the acquisition programme.

The custom-made microfluidic chip was placed in the beam path on a double-rotation (Thorlabs, RP01) and three-axis translation stage (Newport Corporation, 443), equipped with micrometer resolution actuators (Newport Corporation, SM-25). This provides full control over the position and angle of the chip, allowing them to be optimised to ensure light travels through the centre of fluid channel, and that the mirrors are at normal incidence to the laser light. A foil pinhole was attached to

the chip (Comar Optics, diameter = 300 ± 8 μm) to ensure that all light reaching the detector had passed through the fluid channel. Alignment of the pinhole was optimised by using a video microscope (Watec, LCL-902HS).

The microfluidic chip was connected to a flow system by inserting syringe needles into the PDMS, and sealing rubber tubing to the connectors using UV-curing optical adhesive (Norland Products Inc., NOA61). This is shown in Figure 4.3. All tubing was kept as short as possible to minimise pumping volumes, whilst care was taken to reduce torsional strain on the connectors. The output rubber tubing was submersed in a beaker to collect the outflow whilst preventing vibrations from droplet formation. The inlet was connected to a syringe pump (Chemyx, Fusion 400).

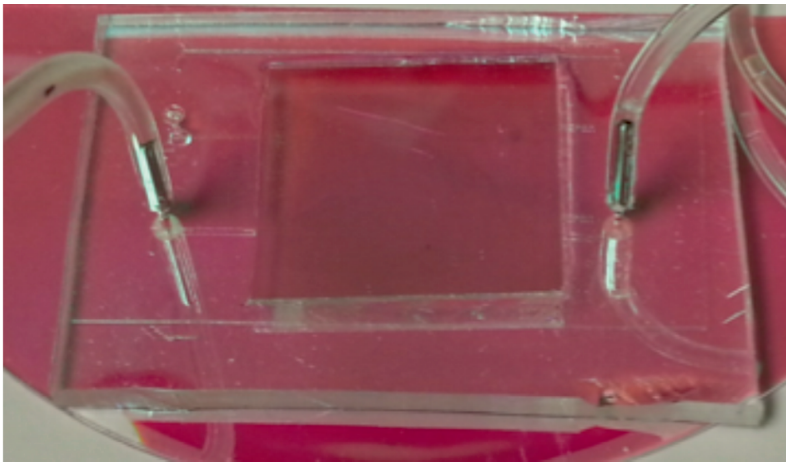

Figure 4.3: A custom-made microfluidic chip with integrated cavity mirrors, and attached connectors and tubing.

Use of PDMS to construct the microfluidic chip places restrictions on the analyte and solvent that can be used within the channel. PDMS has a propensity to swell in size when exposed to certain solvents, particularly organic solvents [73]. Any analyte must also be chemically inert with respect to PDMS. For this investigation, we used thymolsulphonephthalein (known as "Thymol Blue"), a water-soluble pH indicator that exhibits blue colouring at basic pH.

A series of seven solutions of Thymol Blue between 0.5 and 4 mM were made by serial dilution in 50 mM TRIS buffer (tris(hydroxymethyl)aminomethane). The pH of this buffer was measured to be 8.80 using a Jenway pH electrode (Jenway,

3510). The TRIS buffer solution was prepared using 5.1328 g Trizma base (T1503, Sigma-Aldrich) and 1.2335 g Trizma hydrochloride (T3253, Sigma-Aldrich) and making the volume up to 1 L with MilliQ water in a volumetric flask. The TRIS buffer was used as a "blank" solution, and the blank light intensity, I_0, was recorded between each sample to ensure that the microfluidic chip had been completely flushed. The solutions were flowed through the chip using a sterile syringe and fifty spectra acquired and averaged in the LabVIEW program.

In addition to the CEAS measurements performed using the microfluidic chip, the same solutions were analysed in 0.1 cm quartz cuvettes using a commercial UV-vis spectrometer (Cary 100 Bio UV-vis) for comparison.

4.3 Results

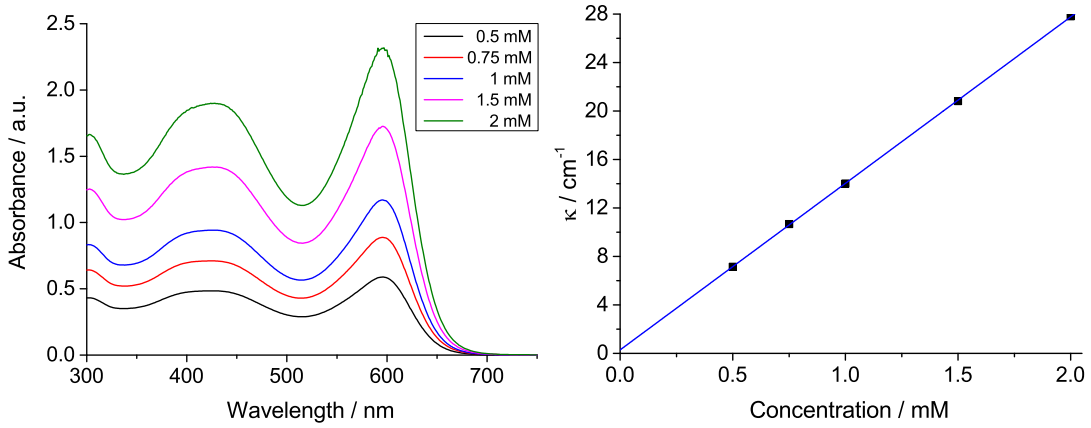

Figure 4.4: (a) A plot of absorption against wavelength for different Thymol Blue concentrations 0.5 - 2 mM, determined in a commercial UV-vis spectrometer; (b) A plot of κ against concentration at 532 nm. The gradient of the graph is 13.646 mM^{-1} cm^{-1}, which equates to 13646 M^{-1} cm^{-1}.

The single-pass data collected using a commercial UV-vis spectrometer is presented in Figure 4.4. Figure 4.4a shows absorption spectra recorded for different Thymol Blue concentrations. Figure 4.4b shows a plot of absorption at 532 nm versus Thymol Blue concentration, the gradient of which yields a natural absorption coefficient of 13646 ± 60 M^{-1} cm^{-1} at this wavelength. The spectroscopic detection

limit of this spectrometer was determined to be $\kappa_{\text{min,s}} = 3.8 \times 10^{-3}$ cm^{-1} in Section 3.5, which corresponds to a $C_{\text{min,s}} = 2.8$ μM of Thymol Blue in a 0.1 cm pathlength.

For the cavity enhanced measurements, a plot of $\left(\frac{I_0}{I} - 1\right)$ against C allows us to determine the cavity enhancement factor, using Equation 2.40. The gradient of the plot, shown in Figure 4.5, yields $\frac{\alpha l}{1-R}$. The single-pass pathlength through the sample, l, was 47.3 μm, and the absorption coefficient, α was taken to be that determined using the UV-vis spectrometer.

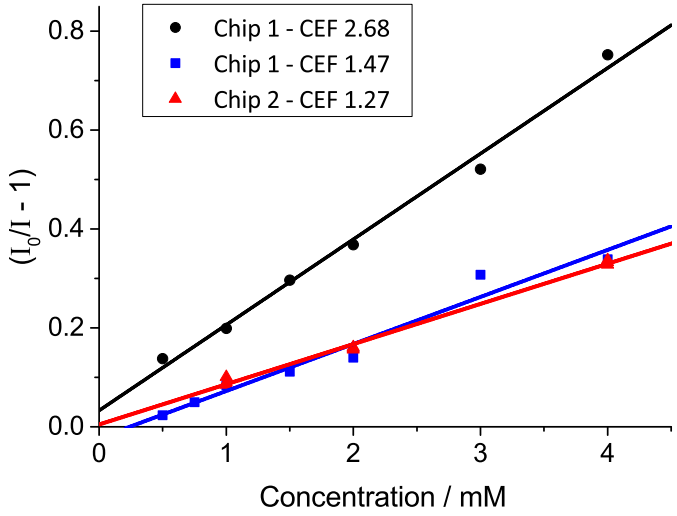

Figure 4.5: A plot of $\left(\frac{I_0}{I} - 1\right)$ against concentration for three experimental runs. The gradients indicate CEFs of 2.68, 1.47 and 1.270.

The first experimental run, shown in black in Figure 4.5, yielded a cavity enhancement factor of only 2.68. From the reported reflectivity of the ESRII film at this wavelength, $R > 99.7\%$, an optimum CEF of around 333 would be expected. Previous experience with PDMS chips has demonstrated that the external PDMS surfaces remain "tacky" after plasma cleaning and can attract dust and other particulate matter over time, that scatter laser light [121, 201]. Therefore, the microfludic chip was removed from the system and thoroughly cleaned before repeating the experiment in as short a timeframe as possible. Repeated measurements, shown in blue in Figure 4.5, provided a CEF of only 1.474.

At this point, the microfluidic chip was replaced with an unused one to eliminate contamination through repeated handling as the cause of low sensitivity. Shown in red in Figure 4.5, this iteration yielded a CEF of only 1.27.

4.4 Discussion

The experiments detailed in this chapter demonstrate essentially no cavity-enhancement, with the number of passes through the fluid channel proving worse than the multi-reflection experiments described in Section 1.3.2 and summarised in Table 1.2, which do not involve the formation of a true optical cavity. Based on the reported mirror reflectivity, an enhancement of at least one to two orders of magnitude would be expected. The poor CEF achieved can likely be attributed to non-parallel mirror alignment, scattering/refractive losses from the thin layers of PDMS between the mirrors and the channel, and/or a reduction in reflectivity of the ESRII film due to the increased refractive index (of PDMS *cf.* air) at the mirror surface.

As discussed in Section 2.2.1, the stability criterion $g_1 g_2$ for a plane-parallel cavity is equal to 1 for all cavity separations *only* if the two mirrors are aligned perfectly parallel to each other. Any small deviation in alignment angle will result in the modes "walking" out of the cavity, as the coupled light does not retrace the same path on each round-trip through the cavity. Although care was taken to ensure flat and well-defined channel dimensions during the fabrication of the microfluidic chip, achieving such precise alignment is experimentally challenging.

The effects of placing a thin layer of PDMS over the ESRII mirrors are unclear, although it is possible that PDMS expansion could lead to a lensing effect, causing increased scattering and refractive losses. Furthermore, the exterior PDMS surfaces proved difficult to keep clean within a non-cleanroom environment, likely causing additional scattering losses from the experiment.

In theory, it would be possible to deconstruct the experiment in order to separate and eliminate the different possible sources of error in a stepwise manner. First building a free standing cavity with ESRII film and optimising; then introducing thin PDMS layers on the mirrored surfaces and characterising them; and finally, introducing liquid samples with increasingly shortened cavity lengths, optimising at each stage until microfluidic dimensions were achieved. However, given the relatively modest CEF possible with even optimal alignment, and with poorly defined mode volumes (see Section 2.2.1) and greater than expected experimental

complexity, it was judged that an alternative configuration would prove a more fruitful avenue for further study: open-access microcavities. These microcavities are the topic of the remaining chapters of this thesis.

It should be noted that two years after these initial experiments, our collaborator, Dr. Cathy Rushworth, did have some moderate success with another iteration of these custom-made microfludic chips, achieving a maximum CEF of 28 at 544 nm [198]. However, this paper notes that the "sensitivity enhancement" (measured as the factor by which $C_{\mathrm{min,s}}$ improved by integrating mirrors into the microfluidic chip) was only a factor of 5. This was attributed to a poorer signal-to-noise ratio, due to the limited amount of light reaching the detector.

4.5 Chapter summary

In an attempt to improve sensitivity by eliminating losses from the surfaces of flow cells introduced into macrocavities (as in Chapter 3), we have integrated cavity mirrors within a microfluidic chip. Custom-made microfluidic chips containing plane-parallel mirrors formed from commercially available ESRII film were designed and manufactured by a collaborator, then characterised in our lab. Unfortunately, the results were underwhelming, with almost no cavity enhancement observed. Given the expected investment of time and resources required to perfect this plane-parallel mirror technique, a strategic decision was made to focus on a more well-defined cavity geometry: open-access plano-concave microcavities.

The following three chapters discuss the development of these microcavities, and characterise their application to optical sensing.

5

Open-access microcavities: refractive index measurements

The "cavity-in-a-chip" sensor described in the previous chapter suffers from a number of performance limitations, and proved to be difficult to troubleshoot. The plane-parallel optical cavity geometry has a poorly defined mode volume, and can prove difficult to align. As an integrated monolithic device, no adjustments can be made to the alignment or cavity length after fabrication, nor can the mirrored surfaces be exposed to chemical contaminants as it is not possible to clean them should they become fouled. Furthermore, the monolithic nature of the device makes it extremely difficult to isolate the impact of individual components, short of requesting that our collaborator produce a whole series of marginally different devices. This chapter describes an alternative method devised to integrate cavity mirrors within a flow cell, whilst avoiding these limitations: open-access optical microcavities.

"Open-access" is a term used to describe optical cavities formed from two separate, independently movable mirrors, an arrangement that allows the length and alignment of the cavity to be modified readily. Sophisticated tracking methods coupled with piezoelectric translation stages allow the cavity length, and therefore the wavelength of the resonant cavity mode, to be controlled to sub-nm precision - a key feature that will be discussed in greater detail later in this chapter. The

open-access nature also makes the mirrors easy to clean, which is very useful when the detection sensitivity is so acutely sensitive to the quality of the cavity mirrors, and also allows for the modification of individual components within the experiment without the need to generate an entirely new prototype each time.

The term "microcavities" has been coined to describe micron-scale optical cavities. In this chapter, we discuss the fabrication of a high-finesse plano-concave microcavity array, which is then integrated into a flow cell system and characterised in an optical sensing experiment. As in the previous chapter, the integration of mirrors into a flow channel is intended to increase sensitivity by removing the largest source of loss of light from the cavity, namely reflection and scattering from the additional surfaces of the flow cell. Switching to a plano-concave cavity configuration leads to a very well-defined mode volume.

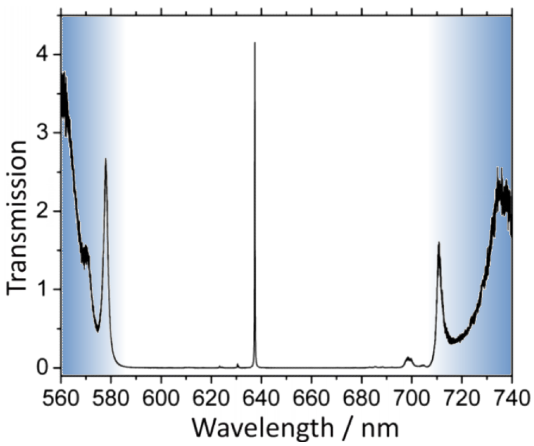

Figure 5.1: The spectral output from a single cavity with a short enough optical pathlength ($d_{\text{opt}} \approx 1.5$ μm) that only one resonant mode is supported. The blue fringes indicate the edges of the photonic stop band, where the increased intensity is due to decreased reflectivity of the cavity mirrors. Adapted from [202].

Using the fabrication technique outlined in Section 5.1, concave microcavity mirrors have been generated with diameters and radii-of-curvature from 2 to 25 μm, enabling us to construct cavities with optical pathlengths from 1 to 25 μm. The large free spectral range associated with such short cavities (Equation 2.3) provides a unique advantage, in that a small number of (often only one) cavity modes will be resonant in each cavity, as seen in Figure 5.1. Given the high finesse of these microcavities, the modes are very well defined, and the open-access nature of the

cavities augments this wavelength specificity with tunability achieved by adjusting the cavity length. The microcavities therefore allow for optical measurements to be performed in which we monitor the change of wavelength and/or amplitude of a *single* well-defined cavity mode in response to a liquid sample introduced between the mirrors. For this reason, high-finesse optical microcavities have attracted significant attention in recent years as a means of sensing refractive index changes and spectroscopic absorption, for trapping and characterising of nanoparticles, and in studying cavity quantum electrodynamics [202–204].

5.1 Microcavity design and fabrication

The microcavity work described in this thesis is a result of a collaboration with Prof. Jason Smith's Photonic Nanomaterials research group in the Department of Materials Science. Prof. Smith and his research group originally developed the open-access microcavities for their work in quantum electrodynamics [202, 205, 206], but have been working with our research group to explore applications in chemical sensing. All microcavity mirrors used in the experiments described within this thesis were manufactured in-house by Dr. Aurélien Trichet (a postdoctoral fellow in Prof. Smith's group).

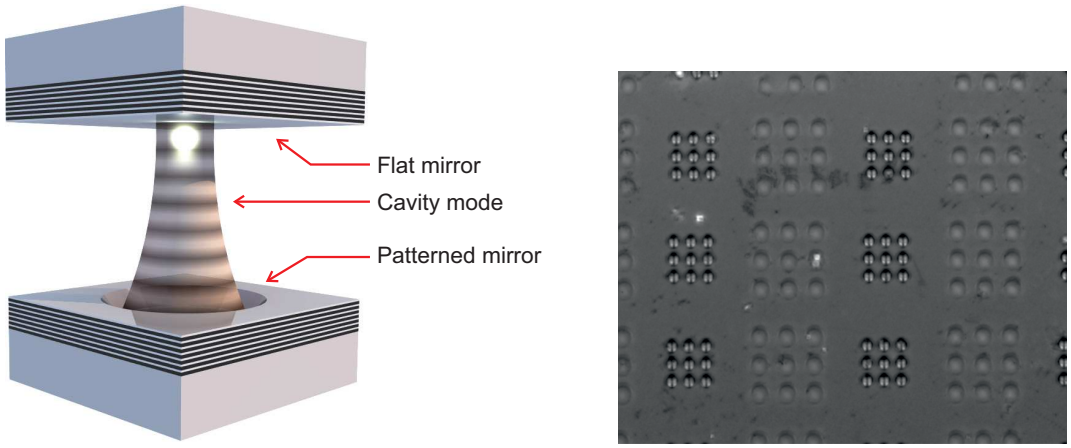

(a) **(b)**

Figure 5.2: (a) Schematic representation of an open-access cavity array; (b) Microscope image of a patterned mirror containing 3×3 arrays of concave features of different diameter, milled into silicon. Adapted from [119].

A schematic diagram of an open-access microcavity array is shown in Figure 5.2a. The plano-concave cavity is formed from two mirror-coated silica substrates: one unfeatured planar substrate, and one with an array of micron-scale concave features milled into it (Figure 5.2b). The array of concave mirrors is fabricated using focussed ion beam (FIB) milling. A beam of gallium ions is focussed onto the surface of the silica substrate to remove atoms from the substrate at the point where they strike. By changing the dwell time of the beam as a function of position, the depth of the feature can be controlled to sub-nanometre precision. FIB milling is used firstly as it allows features to be fabricated with a small enough radius of curvature to yield the desired small mode volume, and secondly as it yields a low surface roughness of 0.7 nm, close to the atomic resolution of the material, resulting in high cavity finesse upon mirror deposition [202]. In this first prototype, a series of 3×3 arrays of micromirror substrates were fabricated, with each mirror having a diameter of 10 μm and a radius of curvature of 25 μm.

The patterned substrates and flat substrates are dielectrically coated to produce the cavity mirrors. For rapid prototyping, this was done by electron beam physical vapour deposition (EBPVD) by the Thin Film Facility in Oxford's Department of Physics. This process involves using a beam of electrons to evaporate the coating material, silicon dioxide, into a vacuum. The material then condenses onto the substrate. Once the silicon dioxide layer has reached the desired thickness the coating material is changed to titanium dioxide and the process repeated. This continues until the desired number of layer pairs has been deposited. The reflectivity stop band, defined as the wavelength range over which the mirrors are reflective, is centred by monitoring the transmission through the substrate at the desired wavelength to optimise the layer thicknesses for maximum reflectivity at this wavelength. EBPVD leads to cavity mirrors with a slightly lower reflectivity than is predicted from the refractive indices of the two materials, due to the formation of pockets within the layers, but it is low-cost and rapid. The mirrors generated by this process are reflective over a wavelength range spanning approximately 590 to 690 nm, with the photonic stop band centred at 640 nm and a reflectivity of 99.74% at this wavelength.

5.2 Experimental setup

The array of concave mirrors (the "patterned" mirror) and the planar mirror are fixed to custom mirror mounts (Figure 5.3a) with optically transparent, solvent-resistant thiolene glue (Norland Products Inc., NOA61). The mirror mounts have integrated fluid inlets and outlets, such that when the mounts are placed opposite each other and sealed with silicone rubber (as illustrated in Figure 5.3), a rudimentary flow cell is formed, allowing liquid to flow into all cavities within the array. The micromirror array is mounted on a kinematic mount (Thorlabs, KC1/M), which allows the cavity lengths to be adjusted manually. In addition, the planar mirror mount is affixed to two cylindrical piezo actuators (NAC2125-A01, Noliac and HPSt 150/20-15/12, Piezomechanik), which allow for control of the cavity length with sub-nanometer precision.

By adjusting the three screws within the kinematic mount, a small angle can be introduced between the two mirrors, producing a tilted wedge-shaped configuration, as shown in Figure 5.4. This allows a range of cavity lengths to be examined at once. The bottom edge of the flow cell is brought together until the mirrors are in contact, whilst at the top of the flow cell, the longest cavity is set to be approximately 10 μm, with the cavity length being determined from the free spectral range of the cavity (Equation 2.3). Pushing the planar and patterned mirrors against each other along the bottom edge has a stabilising effect on the cavities, and the cavity lengths are not observed to change significantly over the course of an experiment. In this way, the cavity length is both known and maintained.

The tilted wedge-shaped configuration of the two mirrors results in optical pathlengths, d_{opt}, varying from 2.238 μm to 10.318 μm across the array of cavities, which spans a width of 165 μm within the flow cell. This gives an angle of 2.8° between the two mirrored substrates.

In the top view of Figure 5.4, the sample is illuminated by 532 nm ($\pm$1 nm) light, and the observed fringes are a result of the variation of cavity length in the vertical direction. The cavities are arranged in 3×3 arrays. For the experiments discussed in this chapter, only the middle column has been selected, corresponding

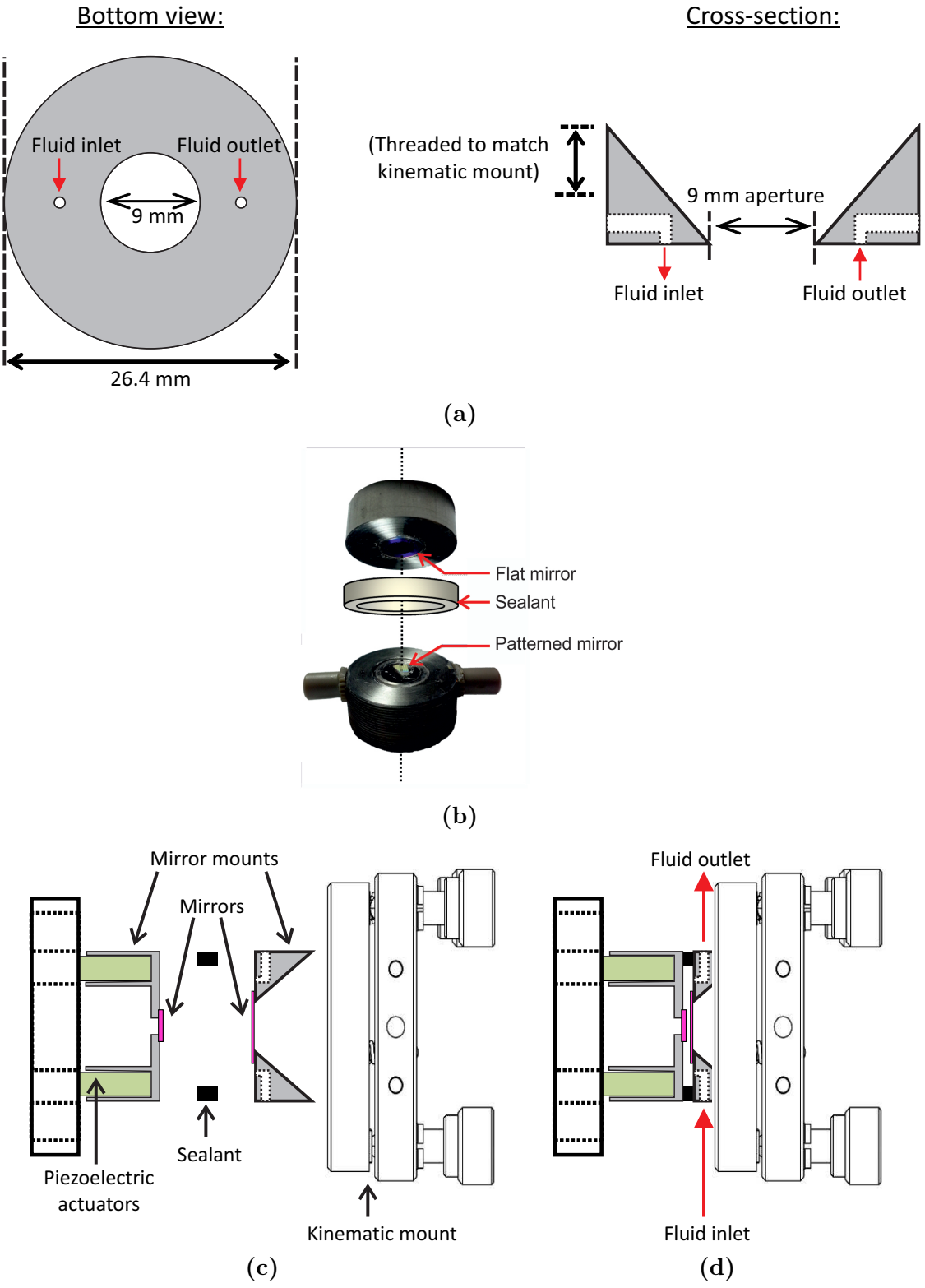

Figure 5.3: (a) Schematic of custom built mirror mounts with integrated fluid inlet/outlet; (b) Expanded view of mirror mounts and sealant ring; (c) Expanded schematic of the custom-designed flow cell for the microcavities, with key features labelled; (d) Schematic of fully constructed microcavity flow cell.

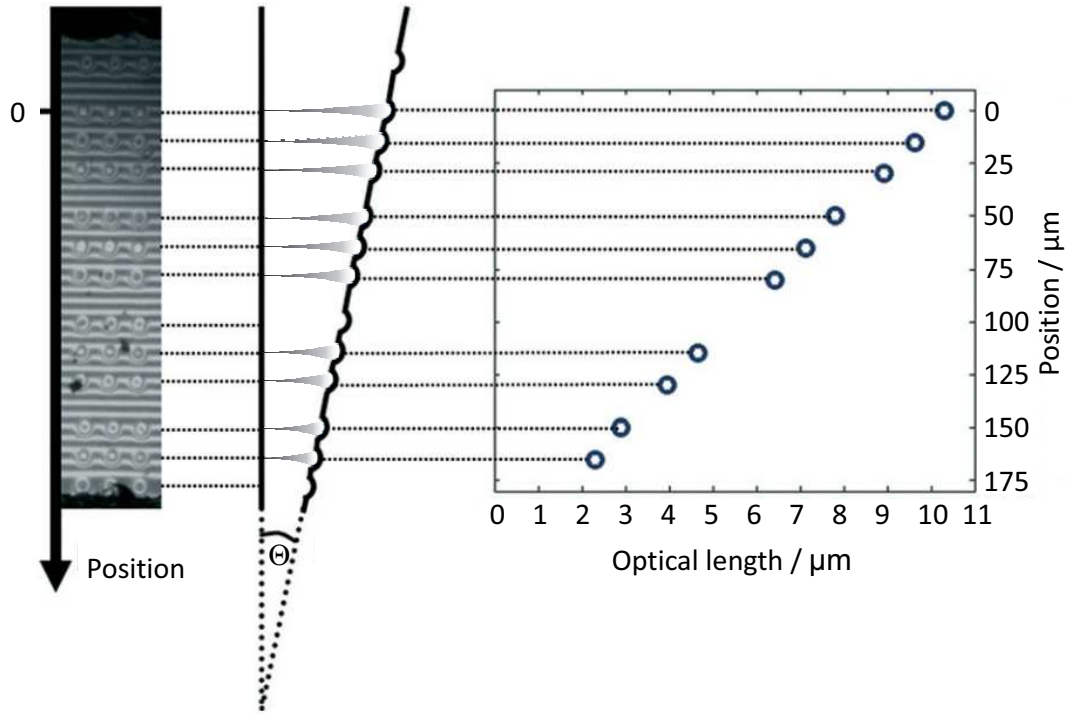

Figure 5.4: Top view (photo) and side view (schematic) of the tilted wedge-shaped mirror configuration (tilt-angle $\approx 2.8°$). The graph demonstrates the linear relationship between the optical length of each cavity with its position in the array. Introducing a tilt angle between the planar and milled mirrors yields an array of cavities each resonant at a different wavelength. Adapted from [119].

to four sets of three cavities in a 12×1 array. The graphic on the right of Figure 5.4 demonstrates the linear relationship between the optical length of each cavity with its position in the array. Two cavities in the array did not show transmission peaks and have been discarded.

The mechanical and chemical properties required for the flow cell sealant posed a significant experimental challenge. Given the range of motion undertaken by the flow cell during alignment, a highly compressible elastomer was required, with sufficient restoring force to prevent leaks, yet not so high as to undergo expansion during the course of the experiment. Water was selected as the solvent for the initial experiments so as to provide a choice from the greatest range of possible elastomers (chemical incompatibility poses significant challenges when other solvents are used). Commercially available O-rings proved to be ineffective, and custom-manufactured solutions were deemed uneconomical during the prototyping stage. A range of

fast-curing liquid elastomers was trialled, until (eventually) a proprietary silicone sealant (Homebase, 281782) with the correct properties was found.

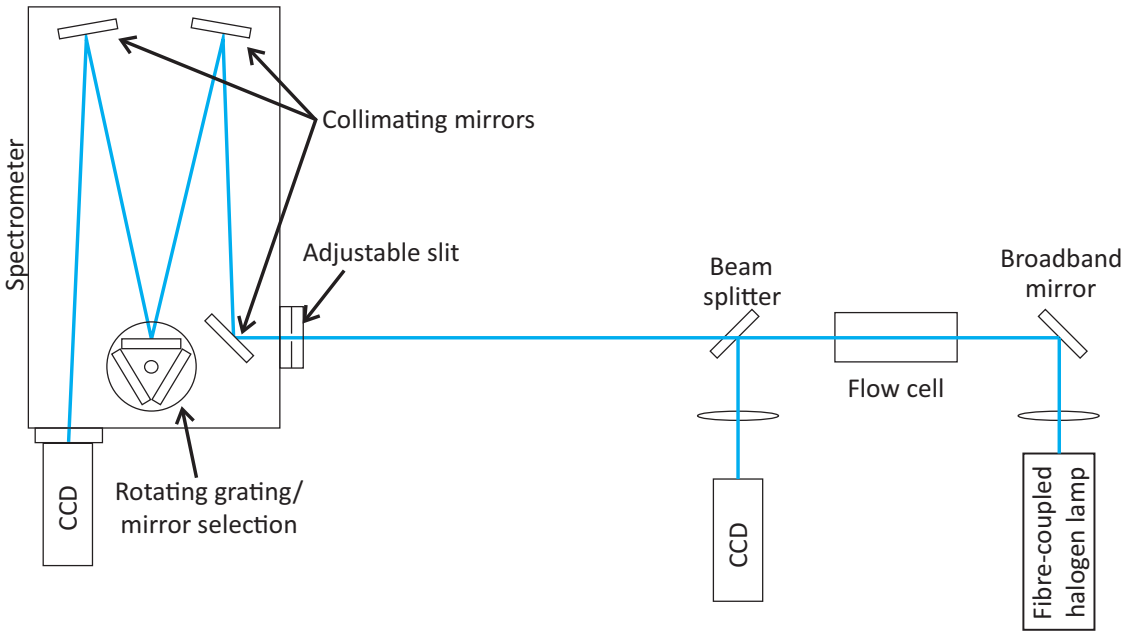

Figure 5.5: A schematic of the microcavity experimental set-up used to detect changes in refractive index.

The flow cell was mounted within a cage-and-rod system, and attached to a three-axis translation stage (Newport Corporation, 443), equipped with micrometer resolution actuators (Newport Corporation, SM-25). This provides full control over the position and angle of the cell, allowing both to be optimised to ensure light travels through the centre of the flow cell.

The cavities are illuminated from the planar side by white light generated by a fibre-coupled, quartz halogen lamp (Betham, WLS100). The white light passes through the microcavity array and an objective achromatic lens collects and focuses the transmitted light into a spectrometer (Andor, Shamrock 500i). The spectrometer has a 300 groove mm^{-1} grating which disperses the incident light by wavelength onto a CCD sensor (Andor, Newton DU940P) which can acquire an image every 100 ms. The spectrometer has a multitrack feature which enables the recorded spectra to be spatially resolved along one axis of the CCD, as well as wavelength resolved along the other axis by the grating. This enables up to ten broadband cavity outputs to be monitored simultaneously given the mirror-array pattern used in this experiment.

The initial alignment of the two mirrors is performed by deflecting 10% of the cavity output for imaging in two dimensions by another CCD sensor. This CCD image is also monitored during the experiment to identify any interferences from contamination or vibrations. An adjustable slit in the spectrometer is used to focus the light from a single column of cavities onto the grating, and each cavity in the column is aligned to a known track on the CCD in the spectrometer.

The flow cell was connected to a flow system by gluing Nanoports (Upchurch Scientific) to the inlet and outlet of the flow cell. This is shown in Figure 5.6. All tubing was kept as short as possible to minimise pumping volumes, whilst care was taken to reduce torsional strain on the connectors. The output tubing was submersed in a beaker to collect the outflow whilst preventing vibrations from droplet formation. The inlet was connected to a syringe pump (Chemyx, Fusion 400).

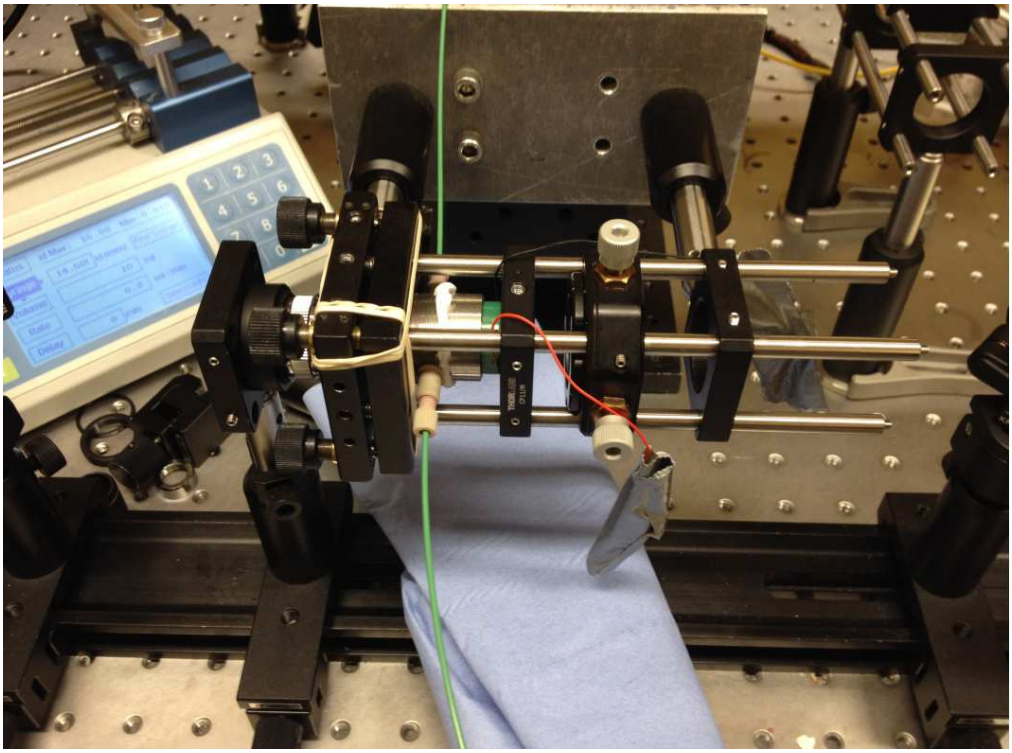

Figure 5.6: Mounted microcavity flow cell, showing connected fluidic system.

It should be noted that this flow system is not microfluidic, with a total pumping volume (defined by the tubing and sealant ring) of >1 mL. In this initial experiment,

the focus was on the feasibility of performing optical measurements within micron-scaled microcavities, which could then be integrated into a microfluidic system at a later date.

5.3 Refractive index measurements

Our initial experiments focussed on the measurement of refractive index changes within the cavities as samples were flowed through them. Refractive index and absorption are two manifestations of the electric polarisability of the medium through which light travels. Electric polarisability describes the response of the medium to the electric field component of the incident electromagnetic radiation. As the driving electric field is time-dependent, there may be some time-lag in the induced response. Fourier analysis of both the driving electric field and the induced electric polarisation allows for separation into different frequency components, whereby the time lag can be represented as a frequency-dependent phase difference. Combining this phase difference with the response amplitude allows the electrical polarisability to be expressed as a complex number with real and imaginary parts. The real part of the response represents the refractive index of the medium, whilst the imaginary part quantifies the absorption of light by the medium.

The Kramers-Kronig relations allow us to calculate the real component of the response function if the imaginary component is known, and *vice versa*. The relationship between the frequency (ω) dependent variables of refractive index, $n(\omega)$, and absorption coefficient, $\alpha(\omega)$, has been shown to be given by [207]:

$$n(\omega) = 1 + \frac{c}{\pi} \int_0^\infty \frac{\alpha(\omega')}{\omega'^2 - \omega^2} d\omega' \tag{5.1}$$

5.3.1 Theory

For refractive index sensing within an optical cavity, we need to establish a link between the refractive index of the cavity medium and a measurable property of the light propagating through the cavity. From Equation 2.1, we recognise that the wavelength of light confined within a cavity of length d will depend on the refractive

index of the medium within the cavity, n. We replace λ with the "medium-dependent" value $\lambda_{\mathrm{m}} = \frac{\lambda_0}{n}$, with λ_0 being the wavelength through vacuum, and rearrange to give:

$$\lambda_m = \frac{\lambda_0}{n} = \frac{2d}{q} \tag{5.2}$$

Such that:

$$\lambda_0 = \frac{2nd}{q} \tag{5.3}$$

It should be noted that this equation only includes the mode number q, and thus is only valid for longitudinal modes. A more realistic treatment that takes into account the transverse modes (defined by the mode numbers q, l and m) in a plano-concave cavity yields:

$$\lambda_0 = \frac{2nd}{q + \frac{1}{\pi}(l + m + 1)\cos^{-1}\sqrt{g_1 g_2}} \tag{5.4}$$

For the purposes of our measurements it is possible to simply consider the longitudinal modes, as they have the greatest intensity and are easily identified in our experimental data. For a selected cavity and longitudinal mode, a change in refractive index, Δn, will result in a change in supported wavelength, $\Delta\lambda_0$, as follows:

$$\Delta\lambda_0 = \frac{2\Delta nd}{q} \tag{5.5}$$

Dividing by Equation 5.3 gives:

$$\frac{\Delta\lambda_0}{\lambda_0} = \frac{\Delta n}{n} \tag{5.6}$$

At present we have assumed that d is the length of the cavity, defined by the distance between the mirrors, and that the refractive index is uniform across this distance. However, in reality light will penetrate a certain distance into the mirrors, and the refractive index within the mirrors will be different from that between them. The mirrors used are distributed Bragg reflectors (DBRs), which are formed of multiple layers with differing refractive indices. The multiple layers provide constructive interference over a range of wavelengths, which defines the

reflectivity band of the mirrors. This means that reflection does not occur at the mirror surface, but within the layered mirror structure, which may extend several hundred nanometres into the surface. For macrocavities (where d is on the order of centimetres) this effect is negligible; however for the microcavities it becomes significant. If we define the penetration depth as d_{mirr}, we can define d_{opt}, the optical pathlength through the cavity including this penetration into the mirrors:

$$d_{\mathrm{opt}} = nd_{\mathrm{geo}} + 2d_{\mathrm{mirr}} \tag{5.7}$$

where d_{geo} is the geometrical distance between the two mirrors. Substituting into Equation 5.6:

$$\frac{\Delta\lambda_0}{\lambda_0} = \frac{\Delta d_{\mathrm{opt}}}{d_{\mathrm{opt}}} \tag{5.8}$$

If we assume that during the course of an experiment both d_{geo} and d_{mirr} are constant for a given cavity, then $\Delta d_{\mathrm{opt}} = d_{\mathrm{geo}}\Delta n$. Substitution into Equation 5.8 gives us a model for refractive index change that considers mirror penetration:

$$\frac{\Delta\lambda_0}{\lambda_0} = \frac{\Delta n}{n}\left(\frac{nd_{\mathrm{geo}}}{d_{\mathrm{opt}}}\right) \tag{5.9}$$

Use of Equation 5.9 to analyse experimental data requires that the cavity mirror separation, d_{geo}, remains constant. However, in the early stages of our experiments, we discovered that the system exhibited a gradual drift in cavity length. This was most probably caused either by thermal fluctuations, or by spring relaxation within the kinematic mount used to position the mirrors. As such, we must consider a more complete examination of the cavity modes. Generalising Equation 2.1 to take account of both penetration into the mirror surfaces (Equation 5.7) and the potential presence of both longitudinal and transverse cavity modes (Equation 5.4), the resonant cavity modes are given by:

$$\left[q + \frac{1}{\pi}(l+m+1)\cos^{-1}\left(\sqrt{1-\frac{d_{\mathrm{geo}}}{r}}\right)\right] = nd_{\mathrm{geo}} + 2d_{\mathrm{mirr}} \tag{5.10}$$

where q, l and m are the mode numbers, and r is the radius of curvature of the concave mirror. Assuming that d_{geo} varies by no more than a few tens of nanometres over the course of a measurement, we can treat it as constant to within one part in 10^6, and the left hand side of Equation 5.10 simplifies to $\frac{q'\lambda}{2}$, where q' is constant for a given mode, but no longer restricted to integer values. The shift in resonance wavelength arising from a variation in the refractive index and/or the cavity length, may then be written:

$$\frac{\Delta\lambda}{\lambda} = \frac{n d_{\mathrm{geo}}}{d_{\mathrm{opt}}}\left(\frac{\Delta d_{\mathrm{geo}}}{d_{\mathrm{geo}}} + \frac{\Delta n}{n}\right) \tag{5.11}$$

From this equation we can see that, for a single cavity, it is not possible to separate the effects of mirror displacement and refractive index change on the resonant wavelength. However, by analysing multiple cavities at once, it is possible to overcome this if we can assume that the variation in cavity length over time is the same for all cavities. As all of the mirrors are part of the same substrate within our setup, we believe that this is a valid assumption.

Therefore, allowing both n and d_{geo} to be time dependent, and assuming that for all cavities the variation in cavity length can be written as $\delta d(t) = d_{\mathrm{geo}}(t) - d_{\mathrm{geo}}(0)$, we now have an equation for each individual cavity, i.

$$\frac{q'(i)\lambda(t,i)}{2} = d_{\mathrm{opt}}(0,i) + n(0)(d_{\mathrm{geo}}(t,i) - d_{\mathrm{geo}}(0,i)) + (n(t) - n(0))d_{\mathrm{geo}}(0,i) \tag{5.12}$$

Substituting for $d_{\mathrm{geo}}(0)$ using Equation 5.7, and using our definition of $\delta d(t)$, we can rearrange to obtain:

$$d_{\mathrm{opt}}(t,i) = \frac{q'(i)\lambda(t,i)}{2} = \frac{n(t)}{n(0)} d_{\mathrm{opt}}(0,i) + n(0)\delta d(t) + 2d_{\mathrm{mirr}}\left(1 - \frac{n(t)}{n(0)}\right) \tag{5.13}$$

which provides us with the key result needed for our analysis. If the penetration depth, d_{mirr} and variation in cavity length, $\delta d(t)$, are the same for all cavities monitored, then at a single time, t, only the first term on the right hand side of Equation 5.13 changes from cavity to cavity. If our assumption is correct, plotting

$d_{\mathrm{opt}}(t)$ against $d_{\mathrm{opt}}(t=0)$ for each cavity at a given time will give a straight line with gradient $\frac{n(t)}{n(0)}$, allowing the change in n to be tracked with time. Note that the parameter $q'(i)$ can be measured for each cavity at $t = 0$, and remains constant so long as the same cavity mode is tracked with time. Also, it is experimentally simple to extract the optical pathlength from the spectra by measuring the free spectral range of each cavity (Equation 2.3).

Furthermore, if the change in cavity lengths ($\delta d(t)$) is assumed to be much smaller than the other length parameters, we can rearrange 5.13 to determine the penetration depth into the mirrors, d_{mirr}.

$$d_{\mathrm{mirr}} = \frac{d_{\mathrm{opt}}(t) - \left(\frac{n(t)}{n(0)}\right) d_{\mathrm{opt}}(t=0)}{2\left(1 - \frac{n(t)}{n(0)}\right)} \tag{5.14}$$

This can be compared with the theoretical value for d_{mirr} [208], which can be calculated with knowledge of the wavelength λ, refractive indices of the cavity medium n_c, and the alternating layers of the dielectric mirror, $n_{\mathrm{SiO_2}} = 1.4$ and $n_{\mathrm{TiO_2}} = 2.1$, and the difference between the two refractive indices of the layers, Δn:

$$d_{\mathrm{mirr}} = \frac{1}{2}\lambda\left(\frac{n_c}{4n_{\mathrm{TiO_2}}\Delta n} + \frac{n_{\mathrm{TiO_2}}}{4n_c\Delta n} + \frac{\Delta n}{2\pi^2 n_c n_{\mathrm{TiO_2}}}\right) \tag{5.15}$$

5.3.2 Flow cell characterisation

As outlined above, we expect to observe a shift in resonant wavelength if we replace a "reference" solution within the cavities, in our case deionised water, by a solution of a different refractive index. For these experiments, a glucose solution of known concentration was used, as glucose has a well-documented refractive index across a range of concentrations, as well as being readily soluble in water and chemically inert with respect to the mirrors and flow cell. Figure 5.7 illustrates the expected form of the signal over the course of the experiment.

An initial investigation was undertaken to examine the effect of sample flow rate upon the measurement. The cavities were set up as described in Section 5.1. Deionised water was flowed through the flow cell to clear any existing residue and to

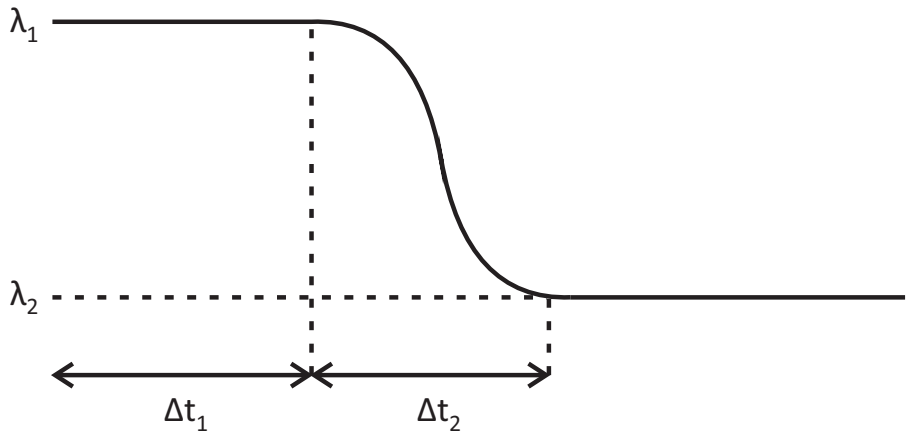

Figure 5.7: Expected wavelength shift as glucose solution is flowed into a cavity. At $t = 0$ the syringe pump begins pumping glucose solution, Δt_1 is the time taken for the glucose to reach the cavity, Δt_2 is the duration of the wavelength shift, taken as the time to entirely replace the cavity contents with glucose solution.

provide the initial refractive index reference. A solution of 1.39 ± 0.002 M aqueous glucose (with refractive index $n = 1.3604$) was connected to the system and the acquisition software set to record spectra from each cavity for a total of 30 minutes, with an integration time of 100 ms. This was repeated for a range of flow rates, and the resulting time-dependent output spectra were examined in order to determine the induction time, Δt_1, before the refractive-index-induced wavelength shift was observed, and the duration of the wavelength shift, Δt_2.

Table 5.1: Wavelength shift delay (Δt_1) and duration, (Δt_2) for different flow rates of glucose solutions. Flow rates above 0.3 mL min^{-1} have been omitted due to increased vibrational noise, which masks the onset of the shift.

Flow rate / mL min^{-1}	Δt_1 / min	Δt_2 / s
0.1	11	100
0.2	7	80
0.3	3.2	70

As shown in Table 5.1, increasing the flow rate reduces Δt_1 significantly, but has little effect on Δt_2. At flow rates above 0.3 mL min^{-1}, Δt_1 was shorter than the time taken for the signal to stabilise following the vibrations caused by changing the input

syringe. Therefore a flow rate of 0.3 mL min^{-1} was chosen for all future experiments, optimising the balance between acquisition time and measurement error.

5.3.3 Refractive index measurements

Having determined the optimum measurement conditions, deionised water was flowed through the flow cell to clear any existing residue and to provide the initial refractive index reference. A solution of 1.39 ± 0.002 M aqueous glucose (with refractive index $n = 1.3604$, determined using an Abbe refractometer) was connected to the system and flowed at 0.3 mL min^{-1}, and the acquisition software was set to record spectra from each cavity for a total of 30 minutes, with an integration time of 100 ms. The system was left undisturbed for several minutes after the wavelength shift had occurred, at which point the syringe of deionised water was reconnected, and the system allowed to return to its initial state as the deionised water was flushed through the cavities.

Figure 5.8a shows a typical spectrum for a single cavity at a single time. Multiple longitudinal modes are visible, as well as their associated transverse modes. The acquired data was processed using custom MATLAB software to generate a time and wavelength resolved spectrum of each cavity. An example is shown in the contour map in Figure 5.8b. The figure shows wavelength against time, with the intensity of the peaks shown by the contour map. During analysis of the data, only the longitudinal mode closest to 640 nm is considered, as this is where the mirrors have highest reflectivity, and therefore the modes have the narrowest linewidth.

The key features of the data are marked in Figure 5.8b. At point A, we see mechanical noise caused by connection of the glucose syringe and vibrations from the initialisation of the syringe pump. After this the cavity begins to relax, though some noise is observed, probably due to small amounts of turbulent flow generated by the pumping action. At point B, around $t = 400$ s, the wavelength of the cavity mode begins to shift as glucose solution enters the cavity. At point C, noise is observed as the deionised water syringe is reconnected to the flow system. Finally, at point D, the wavelengths resonant in the cavity begin to return to their original

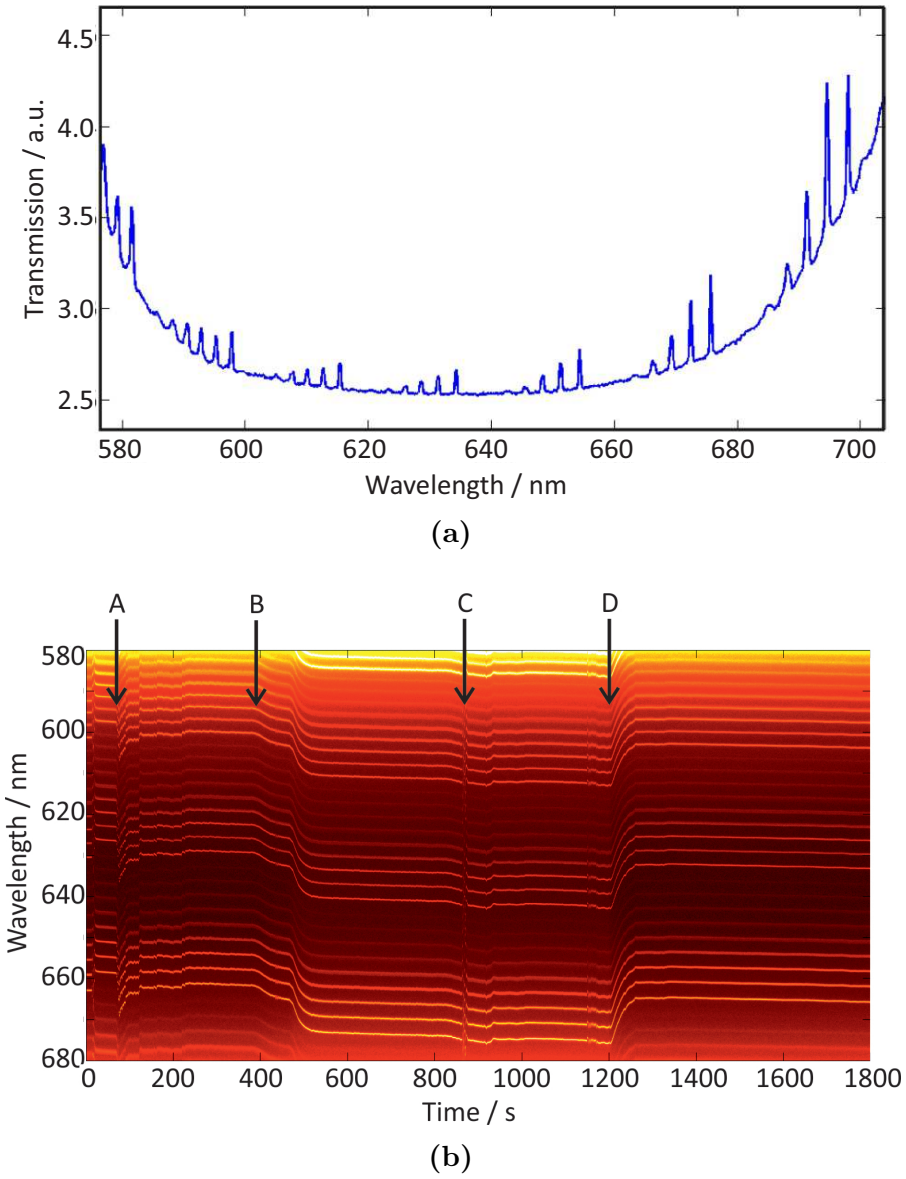

Figure 5.8: (a) White lamp transmission through a cavity ($d_{\text{opt}} = 9.9\ \mu\text{m}$) at a single time, showing a range of stable longitudinal modes and their associated transverse modes; (b) White lamp transmission through a single cavity versus time, with intensity shown by colourmap. Labels: A - Syringe changed to glucose solution; B - Glucose begins to enter cavity; C - Syringe changed to deionised water; D - Water begins to enter cavity.

values as the glucose solution is replaced by deionised water. In addition to the clear shifts in resonant wavelength due to the change in refractive index of the cavity medium, there is an additional small yet constant drift of the mode wavelength over time, caused by either a temperature drift or spring relaxation in the kinematic mount upon which the flow cell is mounted. This is corrected for by monitoring

several cavities simultaneously, and analysing the data using Equation 5.13.

As described in Section 5.3.1, if at a given time we plot $d_{\mathrm{opt}}(t)$ against $d_{\mathrm{opt}}(0)$ for all cavities monitored, the gradient of the resulting line provides $\frac{n(t)}{n(0)}$. Figure 5.9a shows this plot at two different times, $t = 300$ s and $t = 600$ s, before and after the resonant wavelength shifts, respectively. The small difference in the slope reflects the change in refractive index.

Repeating this process for all t allows us to plot Figure 5.9b, which shows measured refractive index as a function of time. The labels A-D represent the same events as in Figure 5.8b. Initially, while the cell is filled with deionized water, the refractive index is constant and shows no drift, demonstrating the reliability of the method we have developed. The same is true at later times, once the microcavity array is filled with glucose solution.

The wavelength shift seen as the glucose enters the cavities shows a distinct "shoulder", appearing over a period of around 100 s. This is thought to be due to the geometry of the flow cell causing both flow- and diffusion-driven entry of the glucose into the cavity array, leading to a rather complex time dependence. In theory, if we were able to carry out experiments under pure diffusion conditions, then it should also be possible to measure the diffusion coefficient of the sample molecule, however this is not feasible with the present flow cell geometry.

Figure 5.9c shows the 3σ uncertainty in the refractive index recorded with a spectrometer sampling time of 100 ms, and provides a good indication of the limit of detection. In the regions of the plot corresponding to deionised water and glucose solutions, the uncertainty is 7×10^{-4} RIU. During the resonance shift, whilst the glucose solution is diffusing into the cavity, the uncertainty in the measured refractive index is seen to be much higher, increasing by up to a factor of 10. The increase in uncertainty arises because glucose diffuses into each cavity at a different rate - for example, the wavelength shift in the final cavity to be filled is delayed by approximately 8 seconds compared to the first cavity. This effect could be mitigated by improving the flow dynamics of the flow cell.

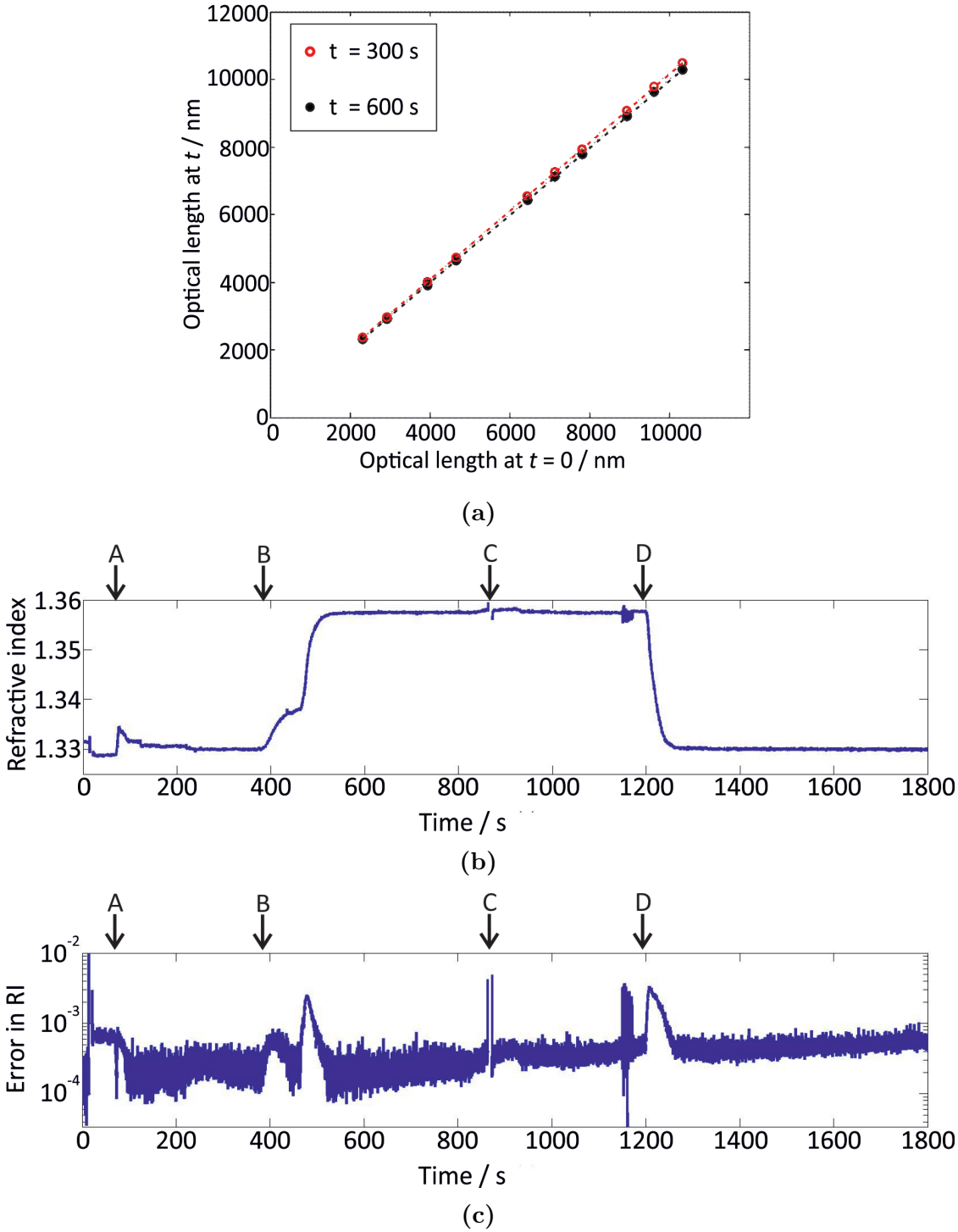

Figure 5.9: (a) Optical pathlength at time t against optical pathlength at time $t = 0$ for different cavities. Plots are shown for two different times, $t = 300$ s and $t = 600$ s (before and after the resonance shift). (b) Measured refractive index of cavity medium as a function of time. Labels: A - Syringe changed to glucose solution; B - Glucose begins to enter cavity; C - Syringe changed to deionised water; D - Water begins to enter cavity. (c) 3σ error of the measured refractive index (logarithmic scale).

An Allan variance analysis [188] of the data, initially averaged over the 100 ms timescale of the spectrometer, is shown in Figure 5.10a. Minimum variance is observed when averaging over 400 ms. Re-averaging the data over this time reduces the 3σ detection limit to 3.5×10^{-4} RIU.

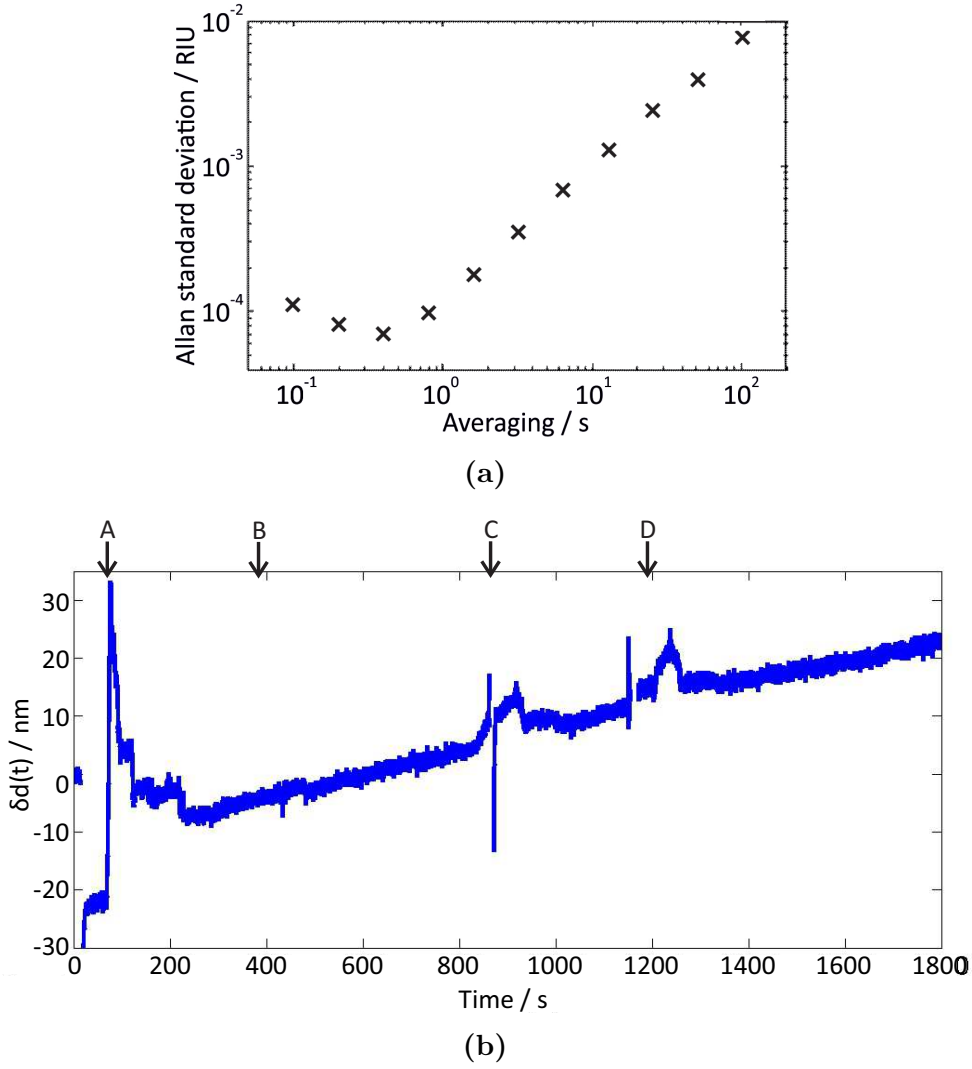

Figure 5.10: (a) Allan variance for the measured refractive index as a function of sampling time; (b) Cavity displacement, δd, as a function of time.

Equation 5.14 allows us to calculate the penetration depth into the mirrors, d_{mirr}, assuming that $\delta d(t)$ is significantly smaller than d_{opt}. This yields a penetration depth of 570 ± 20 nm, which is in close agreement with the theoretical value of 520 nm, calculated using Equation 5.15 [119, 208].

Using this calculated value of d_{mirr}, and the time-dependent refractive index plotted in Figure 5.9b, we can use Equation 5.13 to determine the mirror displacement as a function of time, $\delta d(t)$. This is plotted in Figure 5.10b, and is found to be the same for all cavities within an uncertainty of 1 nm, as assumed in the derivation of our analysis procedure. The overall drift over the course of the experiment is on the order of tens of nanometres, significantly smaller than d_{opt}, as required in order for the derivation of Equation 5.14 to be valid.

5.4 Chapter summary

We have described the design and construction of an open-access microcavity sensor for refractive index measurements. By recording data simultaneously from multiple cavities, we have shown that shifts in the wavelength of resonant cavity modes caused by refractive index changes and physical mirror displacements can be decoupled, thereby overcoming an inherent challenge for sensors based on open-access cavities. Although the flow system into which the microcavities are immersed does not fall within the realm of microfluidics, our first iteration of microcavity sensing demonstrates that it is possible to make high sensitivity measurements using optical cavities confluent with the dimensions of microfluidic systems.

Using 10 μm diameter mirrors with cavity lengths from 2.238 μm to 10.318 μm, we have demonstrated refractive index sensing with a limit of detection of 3.5×10^{-4} RIU. Whilst there are many approaches to refractive index sensing with higher sensitivity, we have been unable to find references to any system capable of detecting refractive index changes of this magnitude in the tiny volume of liquid probed by this experiment. The detection volume is the sum of the mode volumes of the cavities in the array, which can each be calculated using Equation 2.6. The total volume of detection in our setup is 54 fL. Thus, at the limit of detection, the setup can detect the change of refractive index that results from the introduction of 900 zeptomoles (500,000 molecules) of glucose into the device. This limit of detection is governed by the accuracy of the fit to each mode peak, and as such can be improved

by increasing the intensity of the light source, the sensitivity of the detector, the resolution of the spectrometer, or the finesse of the cavities.

In the next chapter, we will adapt this microcavity system to enable broadband absorption measurements via CEAS. In Chapter 7 we will then describe the development of a new prototype with improved cavity finesse and a higher intensity light source, along with the development of a cavity mode-locking scheme. This prototype also benefits from an improved flow design, which reduces the total flow volume to microfluidic dimensions.

6

Open-access microcavities: broadband cavity enhanced spectroscopy

In the previous chapter, we described the development of an open-access microcavity system and its application to refractive index sensing. By placing the two mirror plinths in a tilted wedge-shaped conformation, we produce an array of optical microcavities with different cavity lengths. In our refractive index measurements, we used these different pathlengths to discriminate between shifts in the resonant wavelengths caused by refractive index change and those caused by physical mirror displacements. In the context of absorption spectroscopy, however, these different cavity lengths allow us to monitor absorption at a number of different wavelengths simultaneously (Equation 2.1). As discussed in Section 5.3, refractive index and absorption measurements are simply two manifestations of the electrical polarisability of the medium through which light travels. In this chapter we detail the modifications to the experiment necessary to perform broadband CEAS measurements on a micron-scale, and determine the detection sensitivity of our setup.

6.1 Microcavity setup

As before, the cavity mirrors were manufactured in-house by Dr. Aurélien Trichet as part of a collaboration with Prof. Jason Smith's research group in the Department of

Materials, using the same technique outlined in Section 5.1. For these experiments, the design of the patterned mirror was altered to yield a uniform 10×10 array of equally spaced concave mirrors (Figure 6.1a), each 10 μm in diameter and with a radius of curvature of 25 μm.

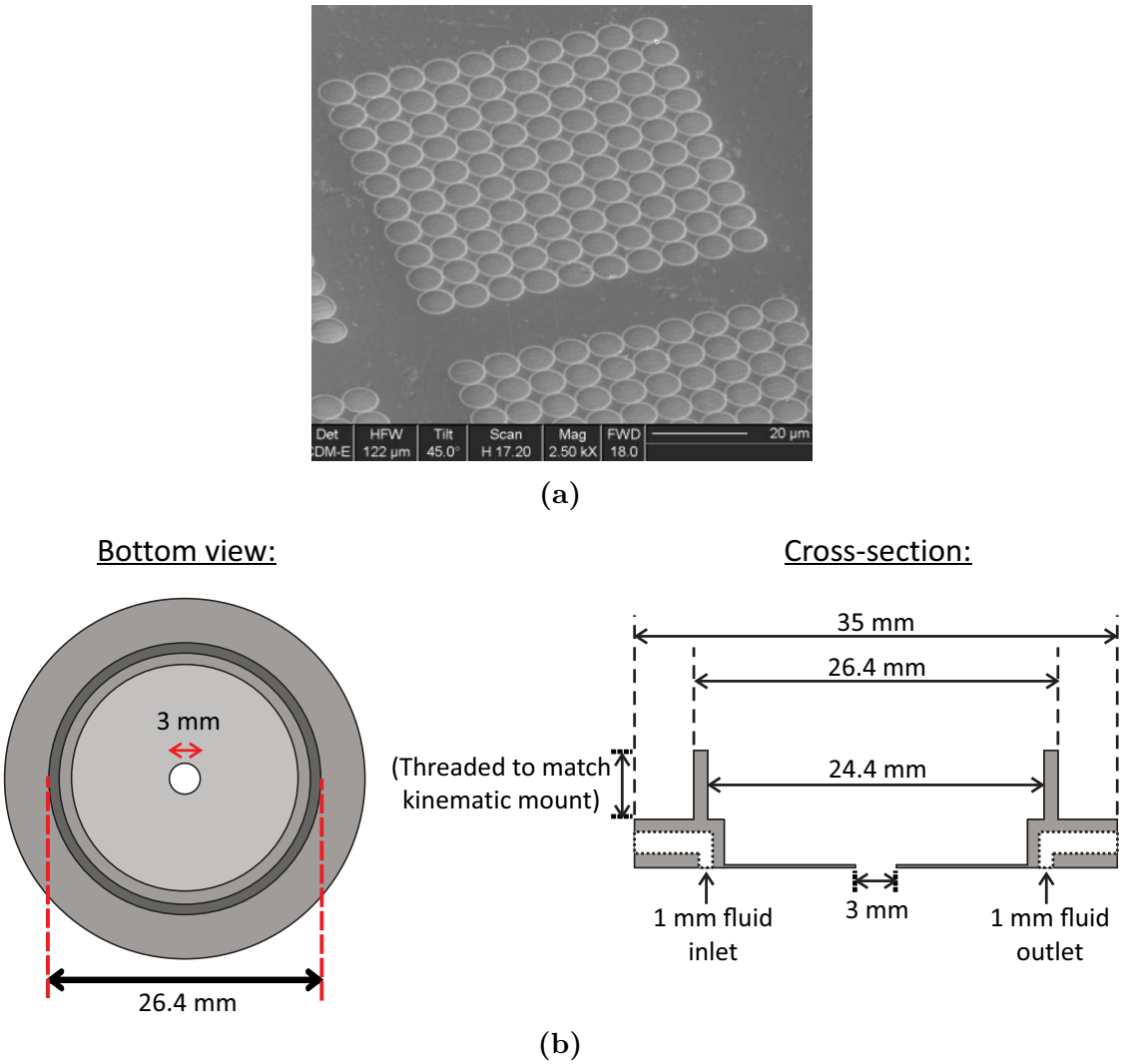

Figure 6.1: (a) Uniform array of equally spaced 10 μm diameter, 25 μm radius of curvature concave mirrors; (b) Redesigned mirror mounts with integrated fluid inlet/outlet and increased internal clearance to allow for more facile integration of optics.

The mirror mounts used to form the flow cell were also redesigned for this experiment (Figure 6.1b). In the previous prototype, the sloped edges illustrated in Figure 5.3a would often obstruct the approach of the objective achromatic lens used to collimate the microcavity output, complicating alignment of the system. For this reason, these sloped edges were removed in order to maximise internal

clearance. The array of concave mirrors and the planar mirror were then fixed to these mounts with optically transparent, solvent-resistant thiolene glue (Norland Products Inc., NOA61). As before, the flow cell is formed by placing the mounts opposite each other, with a sealant material in between.

The results of Chapter 5 indicated that samples enter the cavities through a combination of forced flow and diffusion. The syringe pump drives the solution into the flow cell around the cavities, followed by diffusion of the analyte into the cavities themselves. In order to improve the flow dynamics within the microcavity system, a decision was made to switch to a lower viscosity solvent than deionised water, namely ethanol. This shift to an organic solvent required a redesign of the sealant for the flow cell, as the proprietary elastomer used in Chapter 5 demonstrated significant loss in mass and change in mechanical properties when cured samples were soaked in ethanol for 1 hour then left to dry. A range of sealants were trialled, with a chemically-resistant single-component self-curing fluoroelastomer (Thermodyn, Fluorodyn VITON caulk) proving to be a reasonable short term solution, with the caveat that it was somewhat difficult to install reliably without leaks.

The micromirror array is mounted on a kinematic mount (Thorlabs, KC1/M), allowing the cavity lengths to be adjusted manually. In addition, the planar mirror mount is affixed to two cylindrical piezo actuators (NAC2125-A01, Noliac and HPSt 150/20-15/12, Piezomeckanik), which allow for control of the cavity length with sub-nanometer precision. By adjusting the three screws within the kinematic mount, a small angle can be introduced between the two mirrors, producing the tilted wedge-shaped configuration introduced in the previous chapter. This allows a number of different cavity lengths to be examined at once, with each cavity supporting a cavity mode at a unique wavelength.

In order to analyse the absorption data, it is necessary to have knowledge of the cavity pathlength in real time. The pathlength can be determined from a cavity's free spectral range using Equation 2.3 if there is more than one longitudinal mode present within the mirrors' reflectivity range. The mirror fabrication process described in Section 5.1 results in mirrors reflective over a wavelength range of

around 100 nm. The minimum pathlength required for more than one longitudinal mode to fall within this range can be calculated by considering Equation 2.3 in terms of wavelength, where $\Delta\lambda$ is the free spectral range, $\bar{\lambda}$ is the average of the two wavelengths observed, n_c is the refractive index of the cavity medium, and d_{opt} is the optical pathlength of the cavity:

$$\Delta\lambda = \frac{\bar{\lambda}}{2n_{\text{c}}d_{\text{opt}}} \tag{6.1}$$

Taking $\bar{\lambda}$ as 640 nm, the centre of the stop band for our mirrors, and $n_{\text{ethanol}} = 1.36$, the minimum optical pathlength required for two modes to be present within the cavity at the very edges of the stopband ($\Delta\lambda = 100$ nm) is 1.5 μm. Monitoring $\Delta\lambda$ for an optical cavity in the array which has at least two resonant modes within the photonic stopband of the mirrors therefore allows the cavity length to be accurately monitored.

Therefore, a small angle is introduced between the two mirrors, such that the largest cavity supports two fundamental modes, with mode numbers n and $n+1$, and the other nine cavities support a single mode each, with mode number n. The cavity length of the largest cavity is determined from the free spectral range in that cavity, and the cavity lengths of all further cavities can be determined by monitoring the change in wavelength of the fundamental mode relative to the fundamental mode of the same mode number in the largest cavity (Equation 2.1). The bottom edge of the flow cell is brought together until the mirrors are in contact, whilst at the top of the flow cell, the optical pathlength of the longest cavity is set to be $< 2\mu$m. Pushing the planar and patterned mirrors against each other along the bottom edge has a stabilising effect on the cavities, and the cavity lengths are not observed to change significantly over the course of an experiment. In this way, the cavity length is both known and maintained.

Given the shallow angle generated between the two touching mirror plinths, the first five cavities are too short to support any cavity modes. The tilted wedge-shaped configuration of the two mirrors results in optical pathlengths, d_{opt}, varying from 1100 nm to 1640 nm across the remaining five cavities in the array. These five

cavities span a distance of 95 μm across the flow cell, corresponding to an angle of 0.3° between the two mirrored substrates.

The flow cell was mounted within a cage-and-rod system, and attached to a three-axis translation stage (Newport Corporation, 443), equipped with micrometer resolution actuators (Newport Corporation, SM-25). This provides full control over the position and angle of the cell, allowing both to be optimised to ensure light travels through the centre of flow cell.

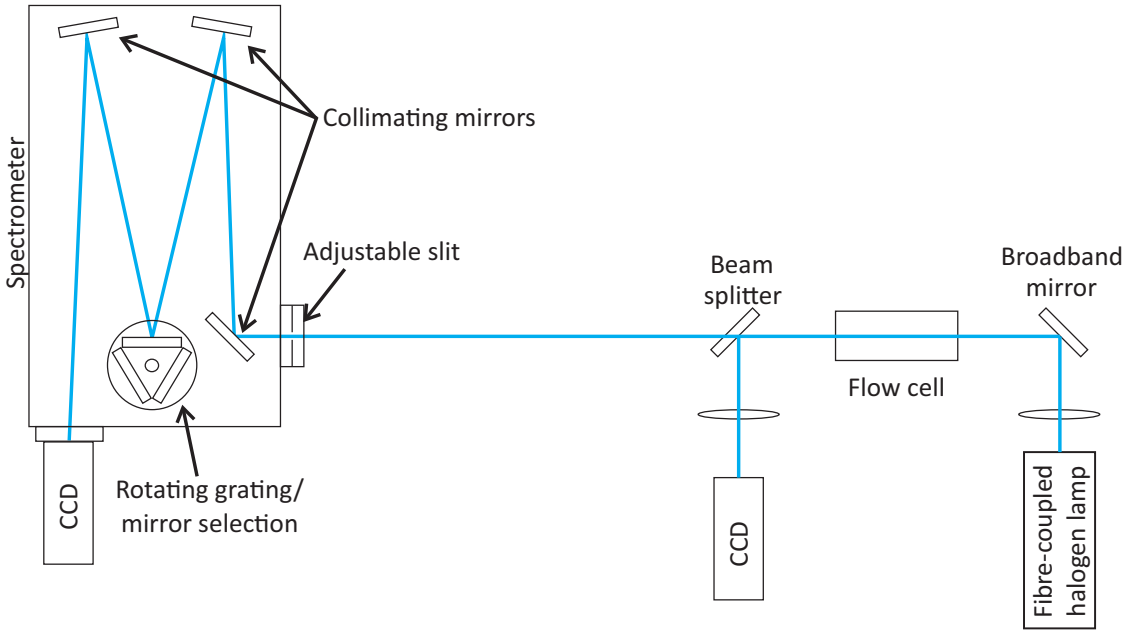

Figure 6.2: Experimental setup used to perform multi-wavelength CEAS using optical microcavities.

The cavities are illuminated from the planar side by white light generated by a fibre-coupled, quartz halogen lamp (Betham, WLS100). The white light passes through the microcavity array and an objective achromatic lens collects and focuses the transmitted light into a spectrometer (Andor, Shamrock 500i). The spectrometer has a 300 groove mm^{-1} grating which disperses the incident light by wavelength onto a CCD sensor (Andor, Newton DU940P) which can acquire an image every 100 ms. The spectrometer has a multitrack feature which enables the recorded spectra to be spatially resolved along one axis of the CCD, as well as wavelength resolved along the other axis by the grating. This enables up to ten broadband cavity outputs to be monitored simultaneously given the mirror-array pattern used in this experiment.

The initial alignment of the two mirrors is performed by deflecting 10% of the cavity output for imaging in two dimensions by another CCD sensor. This CCD image is also monitored during the experiment in order to identify any interferences from contamination or vibrations. An adjustable slit in the spectrometer is used to focus the light from a single column of ten cavities onto the grating, and each cavity in the column is aligned to a known track on the CCD in the spectrometer.

As in Chapter 5, the flow cell was connected to a flow system by glueing Nanoports (Upchurch Scientific) to the inlet and outlet of the flow cell. All tubing was kept as short as possible to minimise pumping volumes, whilst care was taken to reduce torsional strain on the connectors. The output tubing was submersed in a beaker to collect the outflow whilst preventing vibrations from droplet formation. The inlet was connected to a syringe pump (Chemyx, Fusion 400). The total volume of this prototype is less than 1 mL.

6.2 Absorption measurements

Placing the mirrors in contact with the liquid sample places restrictions on the analyte that can be used. Beyond the obvious requirement that the analyte must not chemically degrade the mirrored surface, we must also select an analyte that does not adsorb onto the SiO_2/TiO_2 mirror coating. For this investigation, we used 3,7-bis(dimethylamino)-phenothiazin-5-ium chloride ("Methylene Blue") dissolved in ethanol. Methylene blue is a strongly absorbing dye, with maximum absorption at a wavelength, $\lambda_{max} = 665$ nm [209], close to the centre of our mirrors' range of reflectivity (590 to 690 nm). A literature value for the absorption coefficient, α, at 636 nm is 1.06×10^5 M^{-1} cm^{-1} [210].

A 1 mM solution of Methylene Blue was prepared by dissolving 0.080 g of Methylene Blue hydrate powder (28514, Sigma-Aldrich) in 250 mL of ethanol. Ten concentrations of Methylene Blue between 10 μM and 100 μM were made by serial dilution.

An initial measurement was conducted in a commercial UV-vis spectrometer (Varian, Cary 100 Bio UV-vis) in a 5 mm cuvette to determine the absorption

coefficient, α, of Methylene Blue across all wavelengths. A baseline measurement of absorbance was made on a blank solution of ethanol, and then absorbance spectra of the ten concentrations were recorded for Methylene Blue.

For the microcavity experiments, the acquisition software was set to record 8000 spectra from each cavity, with an integration time of 500 ms for each. This was the minimum integration time that gave an observable signal, chosen to minimise detector noise. This gave a total run time of approximately one hour. A flow rate of 0.3 mL min^{-1} was used to flow blank ethanol and sample solutions through the flow cell in alternation, with flow stopped for one minute between each to allow the system to relax before the next solution was flowed. The experiment was repeated several times to determine reproducibility.

The intensity of the cavity output for the blank ethanol solution was monitored to ensure proper flushing of the cavities. If the blank intensity did not return to the original value, the measurement for the following Methylene Blue solution was discounted.

6.3 Results

The single-pass data collected using a commercial UV-vis spectrometer is presented in Figure 6.3. Figure 6.3a shows absorption spectra recorded for different Methylene Blue concentrations. Figure 6.3b shows a plot of absorption at 636 nm versus Methylene Blue concentration, the gradient of which yields a natural absorption coefficient of 125000 ± 1860 M^{-1} cm^{-1} at this wavelength, in close agreement with the literature value [210].

The data acquired from the microcavity experiment were processed using custom MATLAB software to generate a time and wavelength resolved spectrum of each cavity. An example is shown in the contour map in Figure 6.4. The figure shows wavelength against time (truncated to show only the relevant regions), with the intensity of the peaks shown by the contour map. The peak was fit to a Lorentzian curve, and the integrated intensity averaged over 10 spectra at the end of each stopped-flow relaxation period.

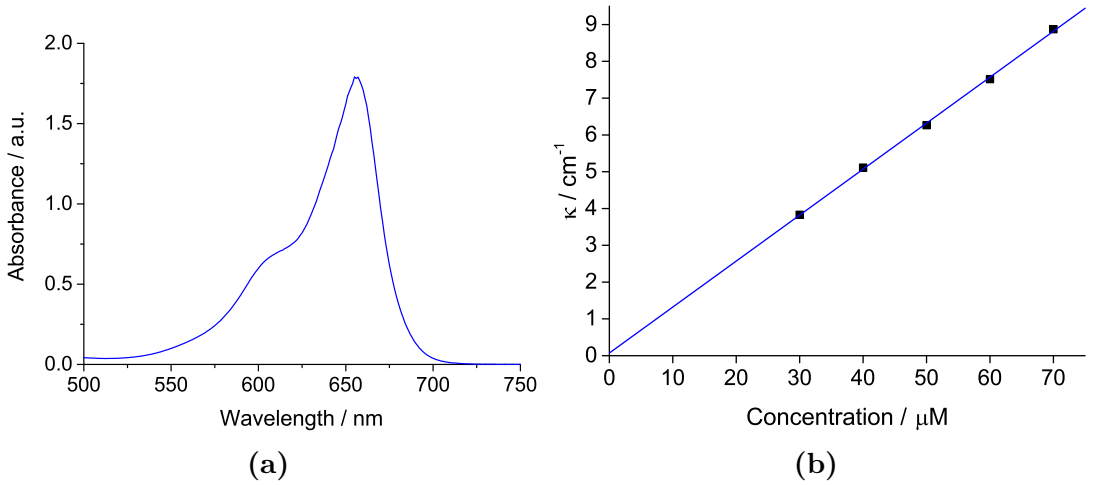

Figure 6.3: (a) Absorption against wavelength for 40 μM Methylene Blue determined in a commercial UV-vis spectrometer; (b) κ against concentration at 636 nm. The gradient of the graph is 0.125 μM^{-1} cm^{-1}, which equates to 1.25×10^5 M^{-1} cm^{-1}.

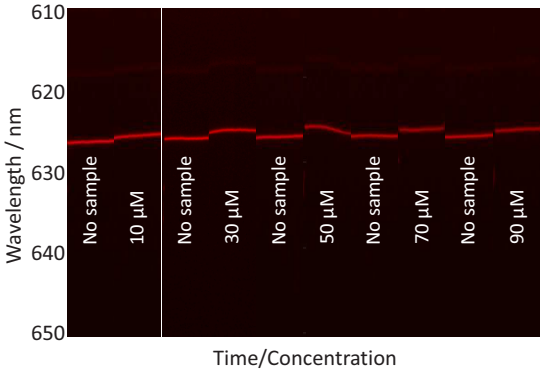

Figure 6.4: White lamp transmission through a single cavity versus time (time axis is discontiguous, illustrating regions of different concentrations). The intensity of a single longitudinal mode (red peak) is monitored as a function of concentration (see Figure 6.5).

The pathlength measured by the free spectral range is the optical pathlength of the light, $d_{\text{opt}} = n_c d_{\text{geo}} + 2d_{\text{mirr}}$, where n_c is the refractive index of the intracavity medium. For the shortest cavities, the penetration depth into both mirrors, $2d_{\text{mirr}}$, accounts for approximately half of the measured pathlength. The physical pathlength through the sample can be calculated by substituting our theoretical calculation of the penetration depth (Equation 5.15) and rearranging:

$$d_{\text{geo}} = \frac{1}{n_c}\left[d_{\text{opt}} - \lambda\left(\frac{n_c}{4n_{\text{TiO}_2}\Delta n} + \frac{n_{\text{TiO}_2}}{4n_c\Delta n} + \frac{\Delta n}{2\pi^2 n_c n_{\text{TiO}_2}}\right)\right] \tag{6.2}$$

where the refractive index of the intracavity medium is taken to be that of

the solvent, $n_c = 1.361$, λ is the wavelength of the cavity mode, and Δn is the difference between the two refractive indices of the dielectric mirror coating layers ($n_{TiO_2} = 2.1$, $n_{SiO_2} = 1.4$, such that $\Delta n = 0.7$). Detection volumes are determined by substituting the calculated pathlengths into Equation 2.6.

For the cavity enhanced measurements, a plot of $\frac{1}{\alpha_\lambda d_{geo}}\left(\frac{I_0}{I} - 1\right)$ against C for each wavelength allows us to determine the cavity enhancement factor from the gradient, using Equation 2.40. The absorption coefficient, α_λ, was taken to be that determined using the UV-vis spectrometer. Typical plots are shown in Figure 6.5.

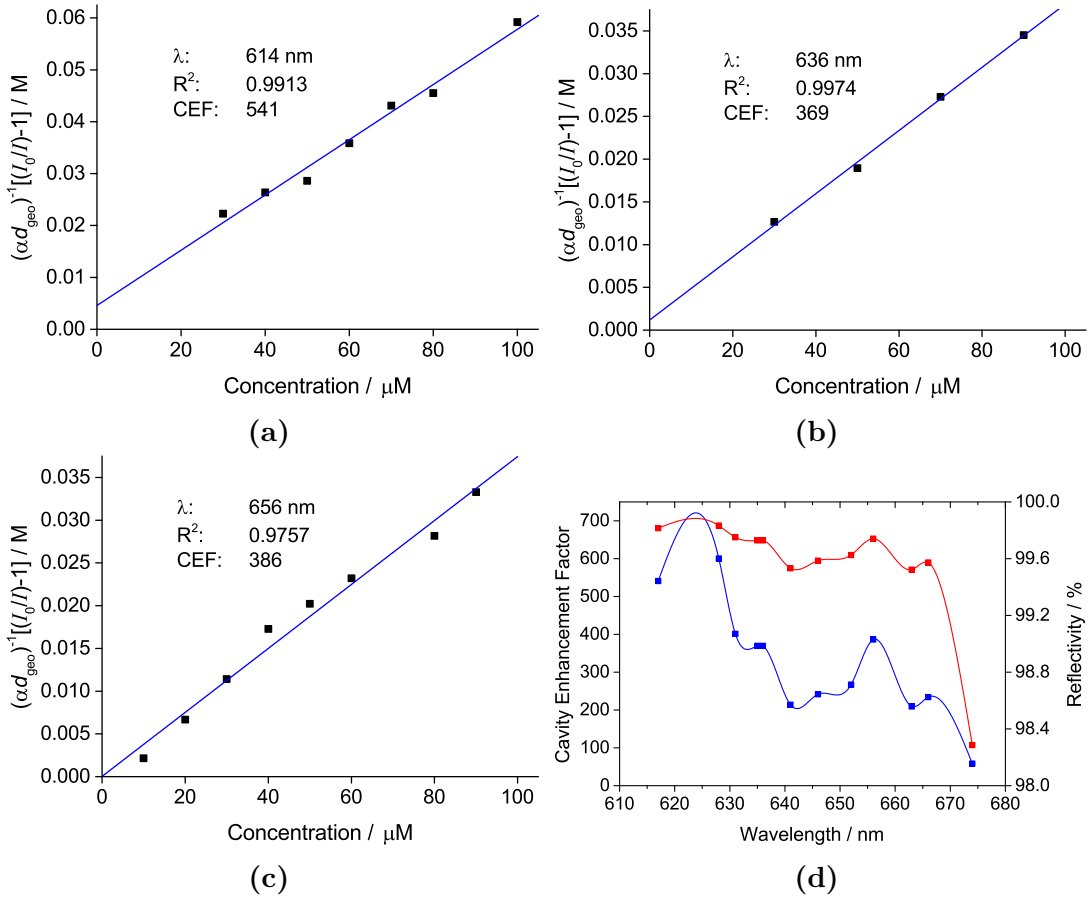

Figure 6.5: A plot of $\frac{1}{\alpha_\lambda d_{geo}}\left(\frac{I_0}{I} - 1\right)$ against concentration for three wavelengths: (a) $\lambda = 617$ nm, CEF = 541; (b) $\lambda = 636$ nm, CEF = 369; (c) $\lambda = 656$ nm, CEF = 386. (d) A plot of CEF (blue) and subsequently calculated mirror reflectivity (red) against wavelength. Spline fits have been placed through the data to guide the eye.

At each wavelength, the standard deviation in the measurement of the blank intensity was calculated and used in Equation 2.44 to calculate the spectroscopic limit of detection (Section 2.3.3.1). The standard error in the y-intercept of the

Table 6.1: Cavity enhancement factors and detection limits for all wavelengths measured. λ is the cavity wavelength, R is the mirror reflectivity indicated by the cavity enhancement factor, d_{geo} is the pathlength through the sample, V_{illum} is the volume of sample illuminated in the cavity mode, κ_{min} is the absorption per unit pathlength (where the subscripts "r" and "s" denote the regression and spectroscopically determined detection limits, respectively (Section 2.3.3.1)), and C_{min} is the lowest detectable concentration of Methylene Blue. The final column indicated the minimum detectable number of Methylene Blue molecules based on the spectroscopic detection limit.

λ / nm	CEF	R /%	d_{geo} / nm	V_{illum} / aL	$\kappa_{\mathrm{min,r}}$ / cm^{-1}	$C_{\mathrm{min,r}}$ / μM	$\kappa_{\mathrm{min,s}}$ / cm^{-1}	$C_{\mathrm{min,s}}$ / μM	No. molecules
617	541	99.82	476	224	0.95	14.7	2.02	31.0	4182
628	600	99.83	486	235	0.68	6.8	2.22	22.4	3164
631	401	99.75	512	255	2.44	22.2	2.50	22.7	3489
635	369	99.73	527	268	0.89	7.1	3.22	25.7	4158
636	369	99.73	527	268	0.88	7.0	2.94	23.1	3738
641	214	99.53	561	297	2.33	16.2	5.67	39.3	7031
646	242	99.59	569	306	2.64	16.1	4.27	25.8	4757
652	267	99.63	611	343	2.48	13.5	3.94	21.5	4450
656	386	99.74	580	319	2.09	10.6	1.71	8.7	1668
663	209	99.52	665	395	2.33	10.6	5.18	23.6	5607
666	234	99.57	626	363	1.18	5.1	5.07	21.8	4774
674	58	98.29	728	460	4.73	18.3	11.82	45.8	12664

plots illustrated in Figure 6.5 was also used to calculate a regression-based limit of detection. All calculated values are summarised in Table 6.1.

6.4 Discussion

Comparing our results with the literature examples of liquid-coupled cavity enhanced experiments summarised in Table 2.2, we can see that the attolitre (illuminated) detection volumes of our microcavity system are significantly smaller than those reported previously, whilst producing cavity enhancement factors towards the higher end of those accessible by other liquid-phase cavity-enhanced techniques.

It can be seen from Figure 6.5d that placing the mirrors in contact with a solution of refractive index 1.361 has slightly altered the reported reflectivity of the mirrors ($R = 99.74\%$ at 640 nm). This is common when employing the "wet mirror" technique to integrate liquid samples (McGarvey *et al.* reported a CEF a factor of two smaller than would be expected for their nominal mirror reflectivity when

attempting a similar scheme on a millimeter scale [142]), although this does not appear to have had a debilitating impact on the sensitivity of our microcavity system.

As discussed in Section 2.3.3.1, we have determined our detection limits using two techniques: a regression analysis and a spectroscopic method. The former is generally expected to give a larger value for $\kappa_{\min}$ because it is affected by all sources of experimental error, for example errors in making up solutions of a nominal concentration. On the other hand, the spectroscopic method is dependent on the error associated with making repeated baseline measurements and is only affected by the inherent signal-to-noise ratio of the instrument. This is not the case in the results summarised in Table 6.1, suggesting that the regression analysis should be treated with caution; due to the limited number of data points available, there may be insufficient statistics for the regression based detection limit to be reliable. However, being based solely on the inherent signal-to-noise ratio of the instrument, $\kappa_{\min,s}$ provides a fair measure of the best possible limit of detection of the set-up [130].

The absorption per unit pathlength ($\kappa_{\min}$) achieved by our microcavity system is significantly limited by our light source. The incoherent halogen lamp used in these experiments is relatively noisy, with a 3σ noise of $\approx 6\%$, and provides limited signal after passing through two highly reflective dielectric mirrors. Despite this limitation, the small mode volume of our microcavities means that the absolute number of molecules being detected is extremely small: only a few thousand molecules. As in the experiment described in the previous chapter, this limit of detection can be improved by increasing the intensity and stability of the light source, the sensitivity of the detector, the resolution of the spectrometer, or the finesse of the cavities.

The large free spectral range of the microcavity system allows us to analyse the change in a single cavity mode in response to an analyte, which opens up the possibility of using another cavity enhanced technique not yet discussed in this thesis: cavity mode-width spectroscopy (CMWS). Nakagawa [168] was the first to note the relationship between increased cavity losses and an increased width of the cavity mode in the context of cavity enhanced spectroscopies:

$$\delta\nu_m = \frac{1}{2\pi n_c \tau} \tag{6.3}$$

where $\delta\nu_m$ is the FWHM of the cavity mode (measured in terms of frequency), n_c is the refractive index within the cavity, and τ is the cavity ringdown time, as defined in Equation 2.30. In determining the cavity ringdown time from the FWHM of the cavity mode, the CMWS technique combines the relative advantages of both the CRDS and CEAS techniques. Like CRDS, it is insensitive to fluctuations in the light source intensity, and requires no knowledge of the mirror reflectivity, R, to make a measurement, removing the need to perform calibration experiments as in CEAS. However, CMWS retains a core advantage of CEAS, in that there is no need for ultrafast detectors, providing greater scope for wavelength-resolved measurements, as well as allowing for very small cavity lengths that result in ultrashort ringdown times.

The core limitation of CMWS is that, in general, tunable and very narrow linewidth lasers are required in order to resolve the FWHM of a cavity mode with sufficient precision. In 2013, Cygan *et al.* [211] used a tunable and Hz-level-linewidth offset-frequency lock (OFL) laser to probe the mode widths of a 75 cm cavity with a finesse of 10500. An 8 Hz linewidth laser capable of being scanned in 2 kHz steps was required to detect changes in the FWHM of cavity modes that varied between 15 to 50 kHz. Such stringent requirements on the light source increase the experimental complexity and limit the applications of such a technique.

We can approximate the magnitude of the FWHM of the longitudinal modes within the microcavities, $\delta\nu$, by using the following two equations:

$$\Delta\nu = \frac{c}{2d_{opt}} \tag{6.4}$$

$$\delta\nu = \frac{\Delta\nu}{\pi n_c \mathrm{CEF}} \tag{6.5}$$

where n_c is the refractive index of the intracavity medium, and is taken to be that of ethanol ($n_{\mathrm{ethanol}} = 1.361$), d_{opt} is the optical pathlength (including penetration into the mirrors), and CEF is the cavity enhancement factor (given in Table 6.1). Calculating $\delta\nu$ at 617 nm (CEF = 541 and $d_{\mathrm{opt}} = 1139$ nm) and

656 nm (CEF = 386 and $d_{\mathrm{opt}} = 1503$ nm) gives $\delta\nu \approx 60$ GHz, which corresponds to $\delta\lambda \approx 0.08$ nm. This is below the resolution of our spectrometer (0.2 nm), however may prove an interesting avenue for future work.

6.5 Chapter summary

We have described the design and construction of an open-access microcavity sensor for cavity enhanced absorption spectroscopy. By placing the microcavity array in a tilted wedge-shaped confirmation, and recording data simultaneously from multiple cavities of differing lengths, we have demonstrated multi-wavelength capabilities. Although the flow system into which the microcavities are immersed is rather rudimentary and may not be considered truly microfluidic, this prototype demonstrates that it is possible to make high sensitivity absorption measurements using optical cavities confluent with the dimensions of microfluidic systems

Using 10 μm diameter mirrors with physical pathlengths from 476 nm to 728 nm, we have demonstrated absorption measurements with a limit of detection as low as $\kappa_{\mathrm{min,s}} = 1.71$ cm^{-1} within a volume of 580 attolitres, corresponding to less than 2000 molecules within the mode volume of the cavity. Although liquid-phase CEAS has been demonstrated with κ_{min} several orders of magnitude lower than this result, we have been unable to find references to any system capable of performing absorption measurements with equal sensitivity on the tiny volume of liquid probed by this experiment. In addition, the reported detection limit is not an inherent limitation of the microcavity system, but rather the noisy halogen lamp used as a broadband light source within our experiments, which leads to a 3σ noise of approximately 6%. As such, our limit of detection could be improved significantly by increasing the intensity of the light source, the sensitivity of the detector, the resolution of the spectrometer, or the finesse of the cavities.

In the previous Section, we also discussed the possibility of utilising the CMWS technique to allow for calibration-free absorption measurements that would be immune to fluctuations in the light source intensity. Such a modification to the experiment would require improving the wavelength resolution, or use of a tunable

narrowband light source in order to monitor the increase in the FWHM of the single mode present within the microcavity in response to increased absorption by a sample.

In the next chapter, we describe the development of a new prototype with improved cavity finesse and a higher intensity light source, along with the development of a cavity mode-locking scheme. This prototype also benefits from an improved flow design, which reduces the total flow volume to microfluidic dimensions.

7

Open-access microcavities: single-wavelength cavity enhanced analysis

In the previous chapter, we described the development of an open-access microcavity sensor and its application to absorption spectroscopy. By placing the two mirror plinths in a tilted wedge-shaped conformation, we are able to produce an array of optical microcavities with different cavity lengths, enabling simultaneous detection at a number of different wavelengths. Given the attolitre mode volumes, we were able to detect the absorption of only a few thousand molecules present within the cavity mode using mirrors with modest reflectivity ($R \approx 99.74\%$). In this chapter, we attempt to improve upon this result by using higher finesse mirrors ($R \approx 99.99\%$), and a much more intense and stable light source.

7.1 Microcavity design and fabrication

As before, the cavity mirrors were manufactured by Dr. Aurélien Trichet as part of a collaboration with Prof. Jason Smith's research group in the Department of Materials. In this iteration of mirror fabrication, the design of the patterned mirror was altered to yield nine rows of cavities, with each row having different dimensions (Figure 7.1a), leading to a number of possible mode volumes. For our

experiments, we utilised a row of 4 μm radius of curvature concave mirrors, the smallest mirrors that yielded a stable cavity.

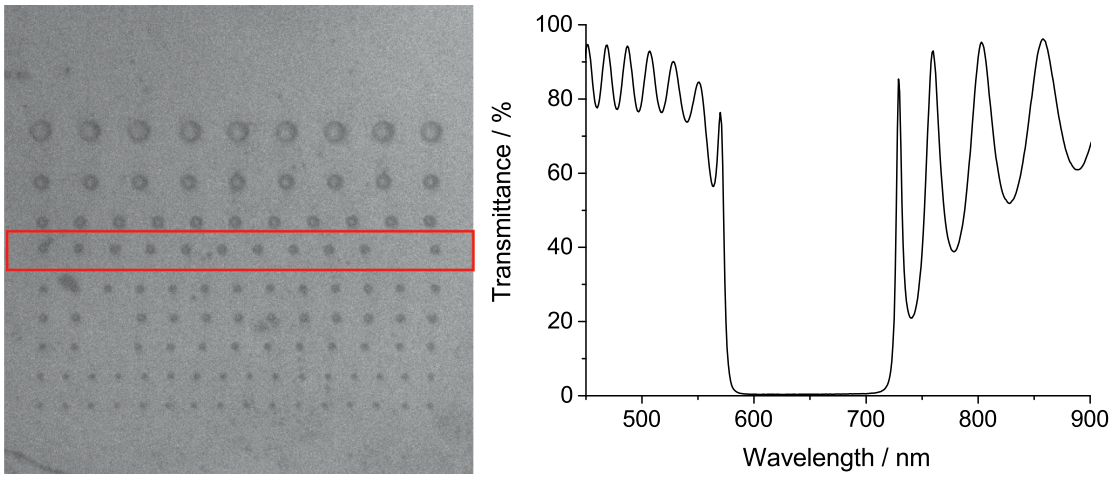

Figure 7.1: (a) Array of micron-scale concave mirrors, with each row possessing a different radius of curvature. The 4 μm radius of curvature mirrors (highlighted with a red box) were used in the experiments described in this chapter. (b) Calculated transmission spectrum of LaserOptik ion-beam-deposition-coated mirrors as a function of wavelength.

To achieve higher reflectivity than the previous prototypes, the FIB milled silica substrates were commercially coated by LaserOptik Gmbh using a process called ion beam deposition (IBD). This technique is related to the FIB milling process described in Section 5.1, with the key difference being that the ion beam is of much lower energy. As a result, when the ion beam is directed onto the surface of the substrate, the ions stick to the surface rather than causing ablation of the surface material. As before, once the required layer thickness has been achieved the ion beam composition is changed to a material of different refractive index, and the process repeated to produce alternating layers. IBD forms much more uniform layers, and therefore creates mirrors of a much higher reflectivity than the electron beam physical vapour deposition technique used for the previous prototypes. The mirrors prepared by this method have reflectivity of 99.99% at 640 nm.

The mirror mounts used to form the flow cell were the same as those described in Section 6.1 and illustrated in Figure 6.1b, and the mirrors were affixed in the same way, using optically transparent, solvent-resistant thiolene glue (Norland

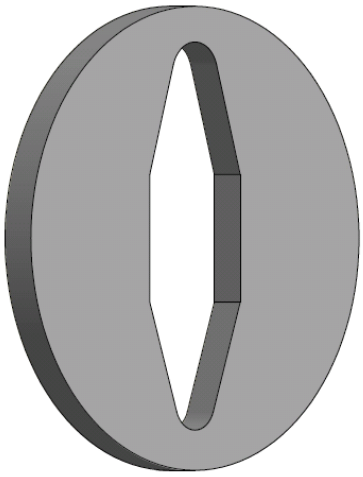

Figure 7.2: Computer aided design of the polymer seal which is compressed between the two mirror mounts.

Products Inc., NOA61). As before, the flow cell was formed by placing the mounts opposite each other, with a sealant material in between. For these experiments, the sealant material used in the previous chapter (Fluorodyn VITON caulk) was replaced due to the difficulty in installing it reliably without leaks. Instead, a stencil was used to cut the required sealant shape (Figure 7.2) from sheets of a pre-cured proprietary elastomer (Gel-Pak, DGL Film XT).

As in the previous prototype, the flow cell was connected to a flow system by glueing Nanoports (Upchurch Scientific) to the inlet and outlet of the flow cell. All tubing was kept as short as possible to minimise pumping volumes, and care was taken to minimise torsional strain on the connectors. The output tubing was submersed in a beaker to collect the outflow whilst preventing vibrations arising from droplet formation at the outlet. With use of a stencil and a pre-cured polymer, it was much easier to control the internal geometry of the flow cell, reducing total flow volume to ≈ 700 μL, including the connected tubing.

The micromirror array is mounted on a kinematic mount (Thorlabs, KC1/M), allowing the cavity lengths to be adjusted manually. In addition, the planar mirror mount is affixed to two cylindrical piezo actuators (NAC2125-A01, Noliac and

HPSt 150/20-15/12, Piezomeckanik), which allow for control of the cavity length with sub-nanometer precision.

In the experiments described in Chapter 6, the poor signal-to-noise ratio achieved when using the broadband halogen lamp limited the sensitivity of the microcavities. The increased reflectivity of the IBD coated mirrors (99.99% *c.f.* 99.74%) in the improved setup further decreases transmission through the mirrors, compounding this issue. Therefore a more stable, higher intensity light source was employed: a narrowband 150 mW laser centred at a wavelength of 640 nm. Use of a narrowband light source precludes use of the free-spectral range of the microcavities as a method of tracking the cavity length in real-time, as in Section 6.1, without greatly increasing the angle between the mirrors or the length of the mirror array. Therefore a new feedback system was developed to track and maintain the cavity length.

7.2 Cavity-locking scheme

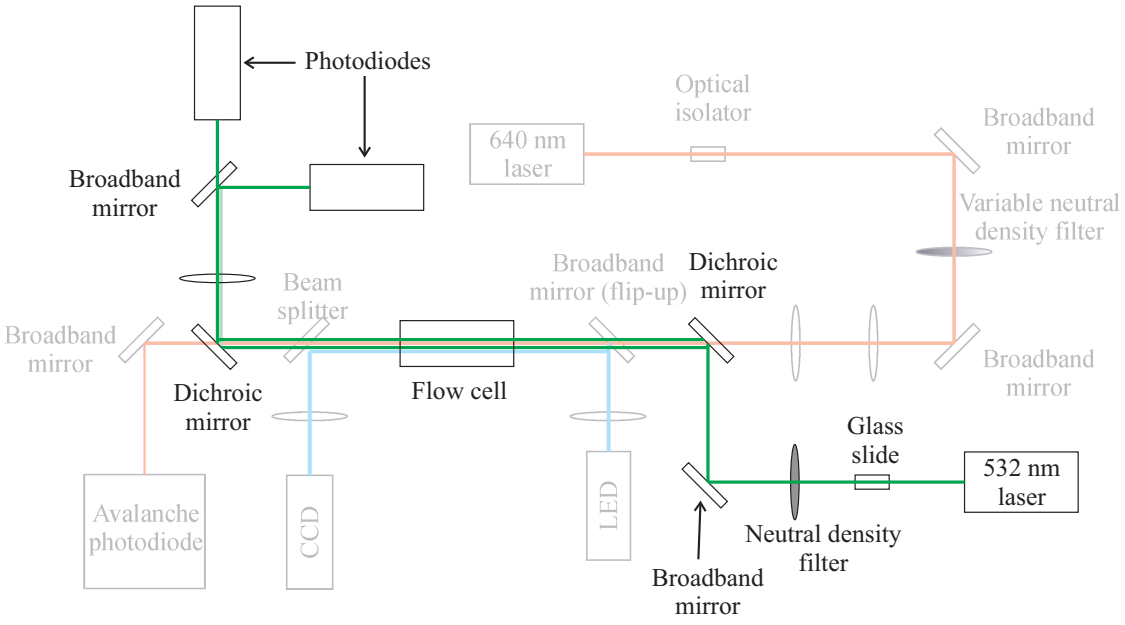

Figure 7.3: Schematic of the optical arrangement used for single-wavelength microcavity sensing, with the cavity-locking components highlighted. A 532 nm laser beam is split into two separate beams, passed through different points on the flow cell, and then detected by different photodiodes.

The cavity-locking system is based on the operating principle of a Fabry-Pérot

interferometer (Figure 7.4a). When opposed by the flat unfeatured mirror, the flat parts of the patterned mirror (between the concave features, see Figure 7.1a) form the interferometer (see Figure 7.4b).

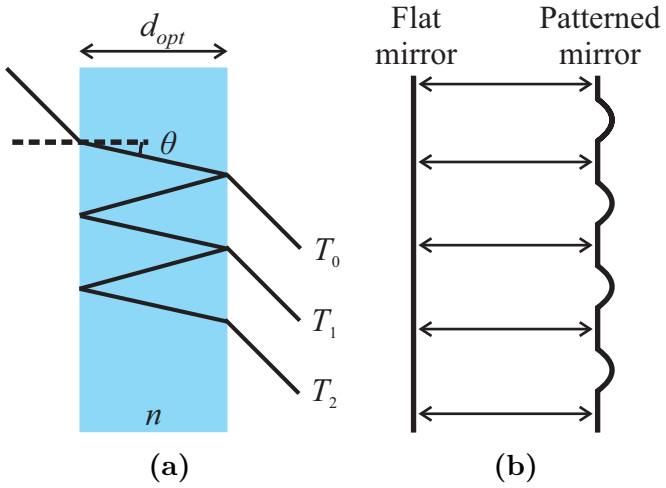

Figure 7.4: (a) A Fabry-Pérot interferometer. (b) The flat regions of the patterned mirror form a Fabry-Pérot interferometer with the opposing flat mirror.

Initial alignment of the cavity array is performed by imaging the cavities using diffuse light from a light emitting diode (LED) with a charge coupled device (CCD) camera. The mirrors are then brought close together until an interference pattern is observed. The phase difference between successive fringes, δ, is given by:

$$\delta = \left(\frac{2\pi}{\lambda}\right) 2 n_c d_{\text{opt}} \cos\theta \tag{7.1}$$

where λ is the wavelength of light, n_c is the refractive index of the medium between the mirrors, d_{opt} is the optical pathlength and θ is the transmission angle to the normal, as shown in Figure 7.4a.

The transmission function, T, for the centre of the bright fringes is then given by:

$$T = \frac{(1-R)^2}{1 - 2R\cos\delta + R^2} \tag{7.2}$$

where R is the reflectivity of the mirrors at the wavelength of the locking laser. By introducing a slight tilt angle of θ, between the mirrors along one axis, the phase difference becomes a function of the vertical displacement along that axis.

In the cavity locking scheme a green laser beam is split into two beams using a glass slide, and focussed onto two different points on the flat portions of the mirrors along that axis. The normalised intensities of the two beam spots transmitted through the mirrors are approximated by:

$$I_1 = \cos\left(\frac{2\pi n_c d_{\text{opt}}}{\lambda}\right) \tag{7.3}$$

$$I_2 = \cos\left(\frac{2\pi n_c d_{\text{opt}}}{\lambda} + \delta\right) \tag{7.4}$$

The intensity of each transmitted beam is measured by a different photodiode (see Figure 7.3). By altering the vertical displacement between where the two locking beams are incident upon the microcavities, δ can be tuned to be $\frac{\pi}{2}$, and a Lissajous-like expression can be calculated:

$$\widetilde{I} = I_1 + iI_2 = e^{-\frac{2i\pi n d_{\text{opt}}}{\lambda}} \tag{7.5}$$

When this is plotted on a complex plane as a function of cavity length, the intensity, $\widetilde{I}$, corresponds to a point moving on a quasi-circular shape (Figure 7.5a). The lower the reflectivity of the mirrors, the more out-of-phase the intensities become and the more circular this shape becomes. The wavelength of the locking laser is chosen to correspond to a low enough mirror reflectivity that the two transmission functions are out of phase with each other whilst maintaining enough reflectivity that there is still an interference effect. This is so that when I_1 reaches a turning point, the derivative of I_2 is non-zero, and the feedback mechanism always "knows" which way the cavity length has changed. In our setup, 532 nm was chosen as the locking wavelength. At this wavelength the mirror reflectivity is 15%.

By using the piezoelectric actuators to close the cavity, such that the distance between the flat regions of the mirrors is zero, and calibrating the point on the Lissajous-like circle at this point, any change in the phase of $\widetilde{I}$ can be correlated to a pathlength relative to this position. The tracking is performed via a custom LabVIEW interface. The software monitors the relative pathlength, and when a mode is found and the lock applied, the feedback loop applies a voltage to the piezo

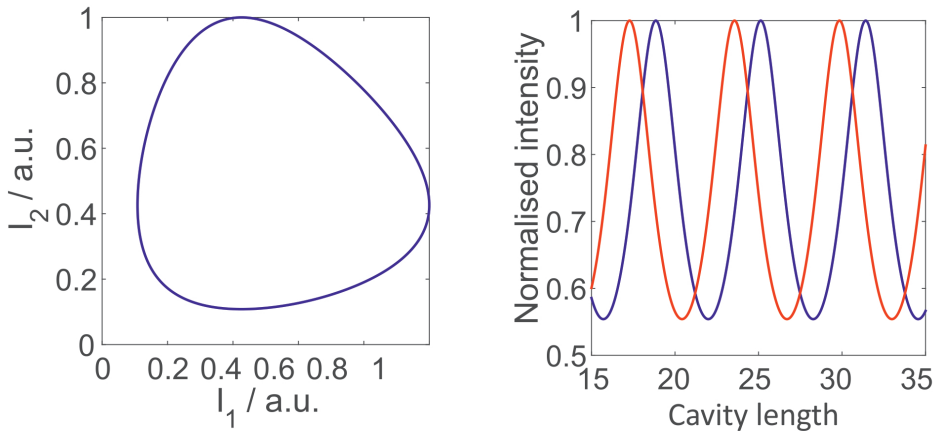

Figure 7.5: (a) Shape of the Lissajous circle for the reflectivity of our mirrors at 532 nm; (b) Transmission intensities I_1 (blue) and I_2 (red) as a function of cavity length.

actuator controlling the cavity length to keep the length constant. The position accuracy is around 10 pm and the refresh rate is 50 Hz.

7.3 Absorption measurements

7.3.1 Optical setup

To perform spectroscopic absorption measurements, a single cavity is illuminated from the planar side by a beam from a highly stable diode-pumped solid state (DPSS) laser (LASOS, RLK 40150, <1% power deviation over 8 hours, <1 MHz linewidth). The 640 nm excitation light is first passed through an optical isolator and a variable neutral density filter optimised to transmit the most power possible without leading to heating within the cavity. The beam spot is then matched to the numerical aperture of an aspheric lens housed in a three-axis translation optical mount attached to the cage-and-rod system of the flow cell. This mode matches and directs the light into the cavity under interrogation, focusing the light down to the diffraction limit within the cavity. The light passing through the cavity is collected by an objective achromatic lens and directed onto an avalanche photodetector (Thorlabs, APD, DET36A/M). The CCD camera is used for initial

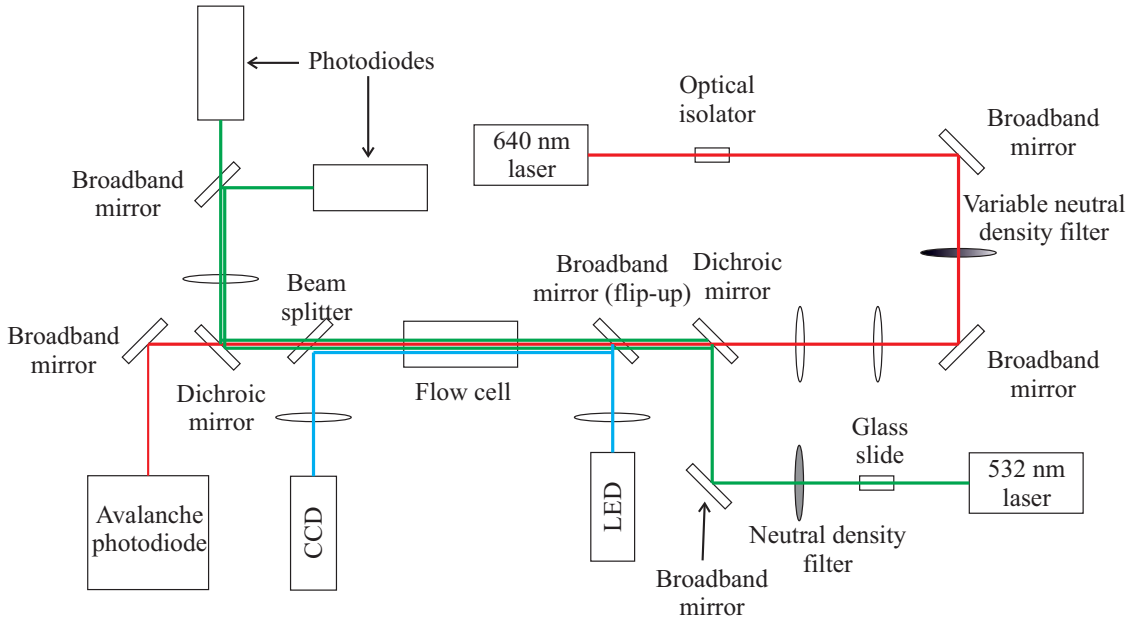

Figure 7.6: Schematic of the optical arrangement used to detect Methylene Blue at a single wavelength. The blue beam path illustrates the light emitting diode (LED) used for initial alignment, after which the broadband mirror is removed from the beam path. The green beam path illustrates the locking mechanism from Figure 7.3. The red beam path illustrates the 640 nm probe laser. All unlabelled optics are lenses.
CCD = Charge-coupled device.

alignment into the microcavity, with final alignment performed by maximising the signal measured by the APD.

One of the piezoelectric actuators attached to the mirror mounts is used to scan the cavity length over a 1 nm range. The scan is controlled by a 1 kHz triangular voltage signal from a function generator. The chosen scan range sweeps the wavelength of the resonant cavity mode across the entire width of the laser mode. By scanning across the entire laser mode, we ensure that changes in the measured transmitted intensity relate only to changes in the finesse of the cavity, and not to changes in which part of the (wider) laser mode the cavity mode overlaps. This scanning of the cavity length serves a dual purpose in that it also limits absolute power build up in the cavity over a longer period of time, preventing heating within the cavity. The second piezo actuator is used to position the planar mirror to achieve the desired cavity length to sub-nanometer precision.

The signal from the APD is interfaced with an oscilloscope (Tektronix, DPO7104) which is doubly triggered, first by the rising portion of the triangular wave supplied

to the scanning piezo, and then secondly by the rising edge of the cavity output. This means that the oscilloscope is locked to the cavity mode itself so that the signal can be averaged. Signal averaging is performed on-board the oscilloscope, and the averaged signal is later transferred to a PC via an ethernet interface for analysis. An Allan variance analysis [188] indicates an optimum on-board averaging time of 100 ms.

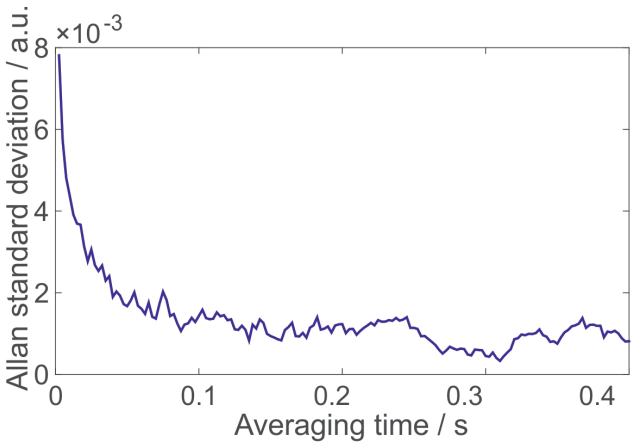

Figure 7.7: A plot of Allan standard deviation against averaging time for single wavelength microcavity experiment.

7.3.2 Sample preparation and handling

A 10 mM stock solution of Methylene Blue was prepared from 0.7988 g of solid Methylene Blue hydrate (Sigma-Aldrich, 28514) dissolved in 250 mL of ethanol. This solution was then diluted to a concentration of 2.5 μM for use in the experiment. Two independently controlled syringe pumps (Chemyx, Fusion 400) were used: one pumping pure ethanol; and the other pumping the solution of 2.5 μM Methylene Blue. The tubing from these two pumps was connected with a Y-connector, creating a turbulent-flow mixing region to ensure that a homogeneous mixture reached the microcavities. By varying the relative flow rates at constant total flow rate, it is possible to pump blanks and samples of various concentrations without having to change syringes (as was required in the previous prototype), reducing vibrational noise.

7.3.3 Measurement protocol

Measurements were carried out by alternating pure ethanol (our blank measurement) and Methylene Blue samples of varied concentration. A total flow rate of 0.5 mL min^{-1} was used to pump a total of 3 mL of liquid in each measurement to ensure the cavity was completely flushed. Whilst liquid was being flowed, the locking scheme was altered such that the cavity length was monitored but not actively maintained, as the response time of the feedback loop to the piezoelectric actuators was sufficiently slow with respect to the vibrational noise induced by pumping that the cavity lock actually *increased* noise. Once 3 mL of liquid had been pumped through the flow system, the cavity lock was restored to bring the cavity back to the correct mirror separation, and the system was left for two minutes to allow the flow cell to stabilise before the trace from the oscilloscope was acquired.

A secondary check that cavity length had been restored to its previous position is possible given the double-trigger used on the oscilloscope: by ensuring that the cavity mode occurs at the same time relative to the first trigger (the rising edge of the triangular signal used to scan the cavity length across the laser linewidth). If this was not the case, it was assumed that the Lissajous tracking system was no longer calibrated, and the experiment was repeated after recalibrating the cavity length using the method described in Section 7.2.

7.4 Analysis

The trace from the oscilloscope is analysed in OriginPro 9 by fitting a Lorentzian function to the observed mode. The data is then analysed using the equations derived in Section 2.3.2.

In order to perform this analysis it is necessary to know the exact physical pathlength through the sample. However, over the course of the experiment, the relative cavity length determined by the LabVIEW tracking system showed a variance of 20 nm, despite being locked to a narrow cavity mode, most likely due to the pulsed flow dynamics generated by the syringe pumps, which may have

altered the alignment of the mirrors relative to one another (this will be explored in greater depth in Section 7.5).

7.4.1 Determination of pathlength

Although the Lissajous tracking system showed variation of 20 nm over the course of the experiment, we know that the cavity was locked to a single cavity mode with mode number q. As q must be an integer number, and we are operating at a single wavelength ($\lambda = 640$ nm), the optical pathlength of our experiment is restricted to multiples of 320 nm:

$$d_{\text{opt}} = \frac{q\lambda}{2} \tag{7.6}$$

This allows us to determine the absorption pathlength from our Lissajous pathlength tracking system, despite the unexpected 20 nm variance (the source of which shall be discussed in detail in the following section).

The Lissajous tracking system measures the optical pathlength between the planar mirror and the flat section of the patterned mirror, d_{sep}. The total optical pathlength of the cavity, d_{opt}, can be calculated by also considering the physical well depth of the concave mirror, $d_{\text{well}} = 600$ nm, the refractive index of the cavity medium, n_c, and the penetration depth of light into the mirrors, $2d_{\text{mirr}}$ (which can be calculated using Equation 5.15):

$$d_{\text{opt}} = d_{\text{sep}} + n_c d_{\text{well}} + 2d_{\text{mirr}} \tag{7.7}$$

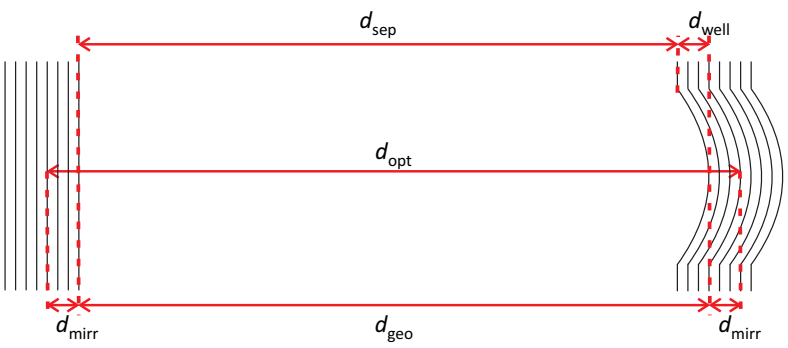

Figure 7.8: Defining the pathlength through an open-access microcavity.

Taking the average measurement of d_{sep} over the course of the experiment (330.8 nm), the refractive index within the cavity to be that of ethanol ($n_c = 1.361$), and the theoretical penetration depth of light into the mirrors ($2d_{\text{mirr}} = 513.8$ nm), gives $d_{\text{opt}} = 1604.6$ nm. This corresponds to a mode number of $q = 5.01$. Since the cavity is aligned until there is a stable resonant mode, if we instead set the mode number to 5, we can determine the physical pathlength through the sample, d_{geo}:

$$\begin{aligned} d_{\text{geo}} &= \frac{1}{n_c}\left(d_{\text{opt}} - 2d_{\text{mirr}}\right) \\ &= \frac{1}{n_c}\left(\frac{q\lambda}{2} - 2d_{\text{mirr}}\right) \end{aligned} \tag{7.8}$$

This gives an absorption pathlength of $d_{\text{geo}} = 839.7$ nm.

7.5 Results

Using our calculated absorption pathlength of 839.7 nm and the nominal reflectivity value of the cavity mirrors of 99.99% calculated from finite-difference time-domain (FDTD) calculations performed by collaborators in Prof. Jason Smith's research group, a value of κ was calculated for each sample using Equation 2.40. Figure 7.9a shows a plot of the mean value of κ against concentration yielding an absorption coefficient, α, of 139400 M^{-1} cm^{-1}, which is very close to the value of 140400 M^{-1} cm^{-1} that was measured in the commercial UV-Vis spectrometer in Chapter 6. Unfortunately, the reliability of this data is poor, as is shown from the large error bars, which represent one standard deviation, $\pm\sigma$, either side of the mean.

Rearranging Equation 2.40 to the form:

$$C\left(\frac{1}{1-R}\right) = \frac{1}{\alpha d_{\text{geo}}}\left(\frac{I_0}{I} - 1\right) \tag{7.9}$$

and plotting the right-hand side against the concentration yields a plot which has a gradient equal to the cavity enhancement factor (Figure 7.9b). The cavity enhancement factor determined in this way is 9270, which is close to the value of

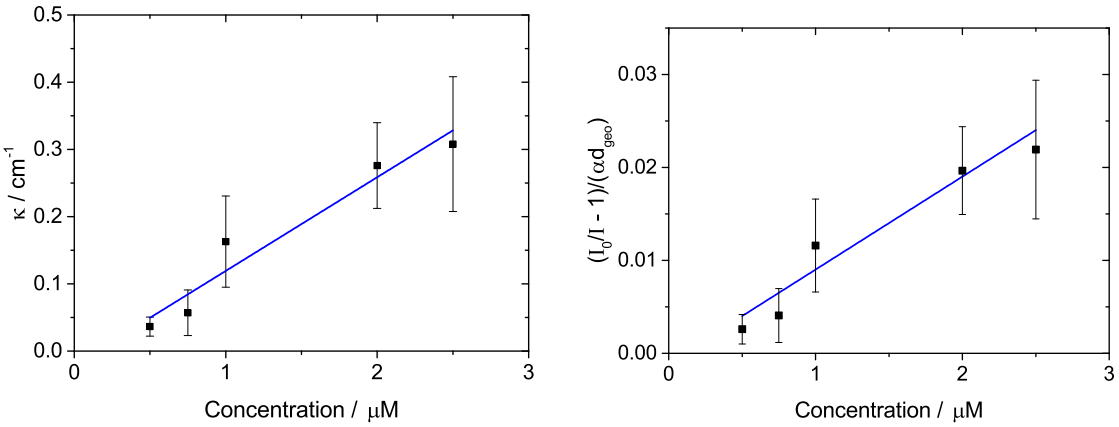

Figure 7.9: (a) A plot of κ against concentration, yielding a gradient of $\alpha = 139400\ \mathrm{M}^{-1}\ \mathrm{cm}^{-1}$; (b) Plot of $\frac{1}{\alpha d_{\mathrm{geo}}}\left(\frac{I_0}{I} - 1\right)$ against concentration, yielding a gradient equal to the cavity enhancement factor, 9270. The error bars are $\pm\sigma$

10000 based on an ideal cavity with the only losses being those due to the reflectivity of the mirrors. Again, the reliability of this data is poor, as is shown from the large error bars, which represent one standard deviation, $\pm\sigma$, either side of the mean.

The most likely cause of this unreliability is related to maintaining alignment of the mirrors. Since the cavity mode is always resonant when we make a measurement, and resonance requires that the optical pathlength satisfies Equation 7.6, we are satisfied that the length of the cavity being interrogated is maintained throughout the experiment. However, as the Lissajous pathlength tracking system erroneously displays a 20 nm variance in the separation of the two mirrors (which would have caused the cavity mode to be non-resonant, if correct), we infer that there is some angular deviation in the alignment of the two mirror plinths. A change in angle, whilst maintaining the length of the resonant cavity would alter the phase parameter δ:

$$\delta = \left(\frac{2\pi}{\lambda}\right) 2n_c d_{\mathrm{opt}} \cos\theta \tag{7.10}$$

Since δ defines the relationship between the intensities of the two locking laser beams, a change in this value will lead to a perceived change in cavity length by the Lissajous tracking system (Section 7.2). Such a change in alignment would

result in a mode remaining resonant, but would alter the finesse of the cavity, and thus the cavity enhancement factor.

Such variation in cavity finesse clearly limits the usefulness of this system. However, a theoretical spectroscopic limit of detection can be calculated from the baseline noise using Equation 2.44. 500 measurements of I_0 were made, and an Allan variance measurement (Figure 7.7) showed that averaging of 100 points led to the lowest standard deviation of 0.002118. The average value of I_0 is 0.133136, yielding $\kappa_{\mathrm{min,s}} = 0.0146$ cm^{-1}, which corresponds to a minimum detectable concentration of 0.104 μM. Using Equations 2.5 and 2.6, the mode volume is determined to be 219 aL, giving a theoretical minimum detectable number of molecules of 14.

Table 7.1: A summary of the limits of detection for the single-wavelength measurements of Methylene Blue in the microcavities. N is the theoretical minimum detectable number of molecules

Wavelength	$\kappa_{\mathrm{min,s}}$ / cm^{-1}	C_{min} / μM	V / aL	N	CEF
640	0.015	0.104	219	14	9270

By making improvements to the reflectivity of the mirrors used, and by using a very stable, collimated light source, significant improvements to the detection sensitivity have been demonstrated. Unfortunately, the concomitant change to a different cavity locking system has led to difficulties in controlling the alignment of the optical cavities, reducing the reliability beyond usable levels. In principle, it appears that this instrument is capable of approaching single molecule detection, however the reliability has to be improved. The following section explores the causes of instabilities, and looks at methods of eliminating them.

7.6 Flow dynamics

In principle, the cavity locking scheme described in Section 7.2 provides the ability to monitor and maintain the cavity length to a high degree of precision (10 pm). However, the locking mechanism requires a small and *constant* angle of at least 0.102° between the two mirrors, such that the intensities of the two locking laser

beams are out of phase by $\delta = \frac{\pi}{2}$ (Equation 7.10) when directed through the top and bottom of the microcavity array. The accuracy of the locking scheme is therefore acutely sensitive to the angular alignment of the two mirrors.

The optical table upon which the experiment is mounted is vibrationally isolated, so the main source of disturbance to the cavity alignment is likely to arise from the pressure variations within the cavity as liquid samples are pumped through the flow system. Figure 7.10 shows a screenshot of the plot of cavity length versus time produced within the data acquisition programme by the tracking function. It shows the change in cavity length as a function of time when the lock is turned off (i.e. there is no feedback loop in operation, the cavity length is simply being monitored). When this data was taken the syringe pump was flowing solution into the cavity at a flow rate of 0.5 mL min^{-1}.

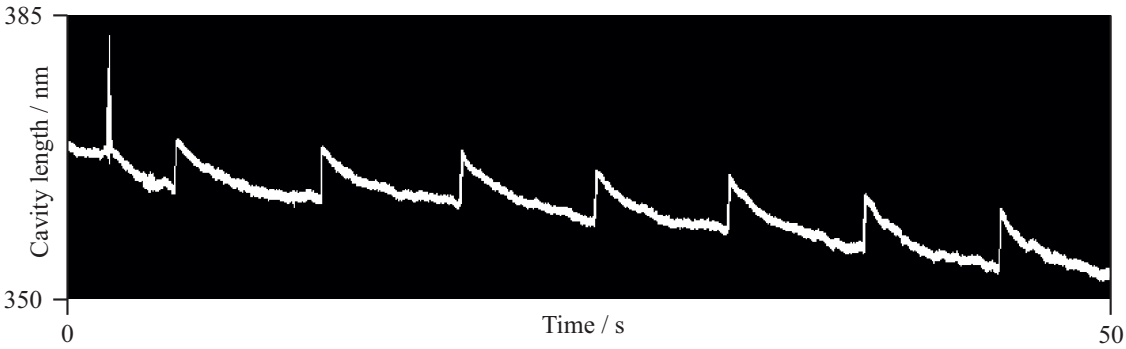

Figure 7.10: Cavity length as a function of time, demonstrating fluctuations when pumping ethanol at a flow rate of 0.5 mL min^{-1} with the Chemyx Fusion 400 syringe pumps. Data was acquired using the Lissajous tracking LabVIEW programme whilst the piezoelectric actuator feedback was disabled.

The periodic jumps observed in the relative cavity length over time are thought to be caused by wavefronts of pressure within the fluid. The Chemyx Fusion 400 syringe pumps use stepper motors to actuate a block which depresses the plungers into the syringes, leading to pulsed flow, which is clearly observable in our measurements. At the low flow rates employed in our experiments, a series of distinct pulses averaged over time produces the desired flow rate, with the system relaxing back to equilibrium between each pulse.

The time dependence of the relaxation can be explained by considering the compressibility of the polymer seal between the two mirror mounts; as the separation of the mirrors reduces back to the initial value, the polymer seal is under compression and pushes back with a restoring force, as given by the compressive normal stress, σ:

$$F_n = A\sigma = A\epsilon E = AE\frac{\Delta l}{l} \tag{7.11}$$

where F_n is the force normal to the mirror mounts, A is the cross-sectional area of the polymer seal, E is the Young's modulus, and ϵ is the engineering strain given by the change in thickness divided by the equilibrium thickness of the polymer seal. A, E and l are all constants, so the restoring force of the polymer seal is proportional to the amount it has been compressed. The reduction in relative cavity length therefore slows down the more the system relaxes back towards equilibrium.

In order to eliminate these pressure waves, a pneumatic flow system (Elveflow, OB1 MK3) has been purchased and some preliminary tests conducted. This system is connected to a dry nitrogen supply at 2 bar and has three air pressure outlets that are connected to a reservoir of solution in a manner that allows the unit to control the pressure in the empty head space of the reservoir. The end of another length of tubing is immersed in the liquid in the solution reservoir and connects the reservoir to the flow cell. Changes in the gas pressure in the head space of the reservoir therefore generate fluid flow through the tube and into the flow cell (Figure 7.11).

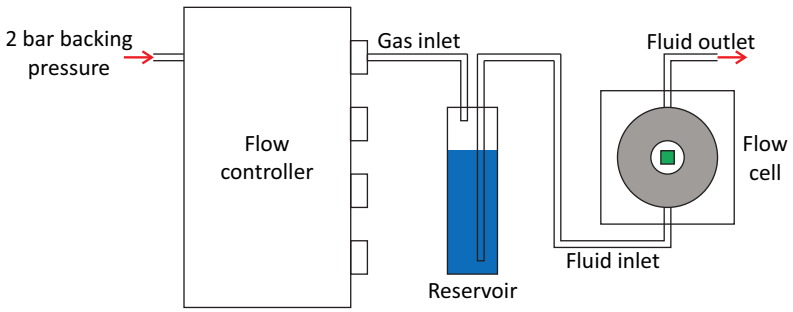

Figure 7.11: Schematic of a pneumatic flow system.

In preliminary experiments, pure ethanol was flowed though the flow cell under an applied pressure of 12 mbar, generating a flow rate of approximately

0.5 mL min^{-1}. Again, the cavity length was tracked but not locked, with the results displayed in Figure 7.12.

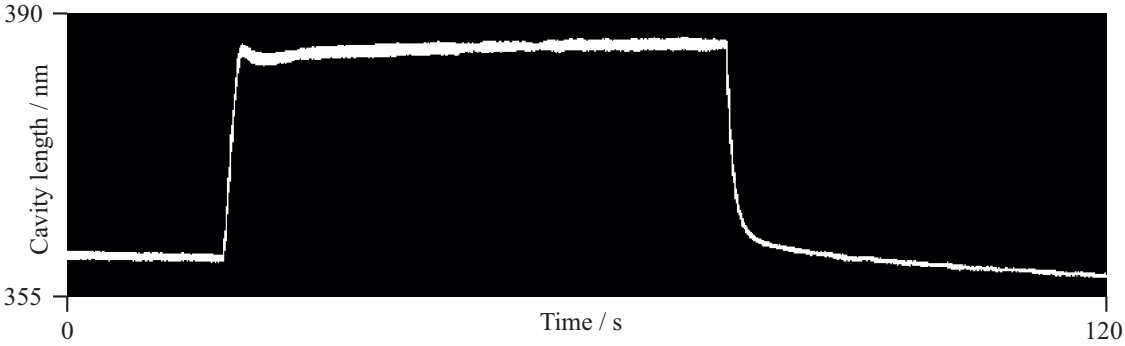

Figure 7.12: Cavity length as a function of time, demonstrating fluctuations when pumping ethanol at a flow rate of ≈0.5 mL min^{-1} with the Elveflow OB1 MK3 pneumatic syringe pump. Data was acquired using the Lissajous tracking LabVIEW programme whilst the piezoelectric actuator feedback was disabled.

As before, the initial sharp increase in cavity length is due to a pressure front moving through the fluid as the pressure source is switched on at around 20 s. There is a small amount of relaxation until the cavity length reaches equilibrium, but then the net force on the cavity mirrors reduces to zero and the cavity length is maintained. The pressure source is then turned off at around 75 s. This results in a sudden decrease in cavity length as the slowing flow generates a contractive force, followed by a slower exponential decrease in cavity length as the system relaxes and pushes against the polymer seal. This behaviour can be explained by recourse to computational fluid dynamics (CFD) simulations (performed by a Part II student, Christopher Mason, in Autodesk CFD) of the flow system. The simulation results are shown in Figure 7.13.

In the CFD simulation, a model of the flow cell interior was built. A transient boundary condition was applied to the flow inlet: a time dependent step-function, with a maximum flow rate of 2 mL min^{-1} and a minimum flow rate of 0 mL min^{-1} (Figure 7.13a). The boundary condition at the outlet of the flow void was set to 0 bar gauge pressure (i.e. the flow was expanding against atmospheric pressure). The force normal to the face of each mirror mount was calculated as a function

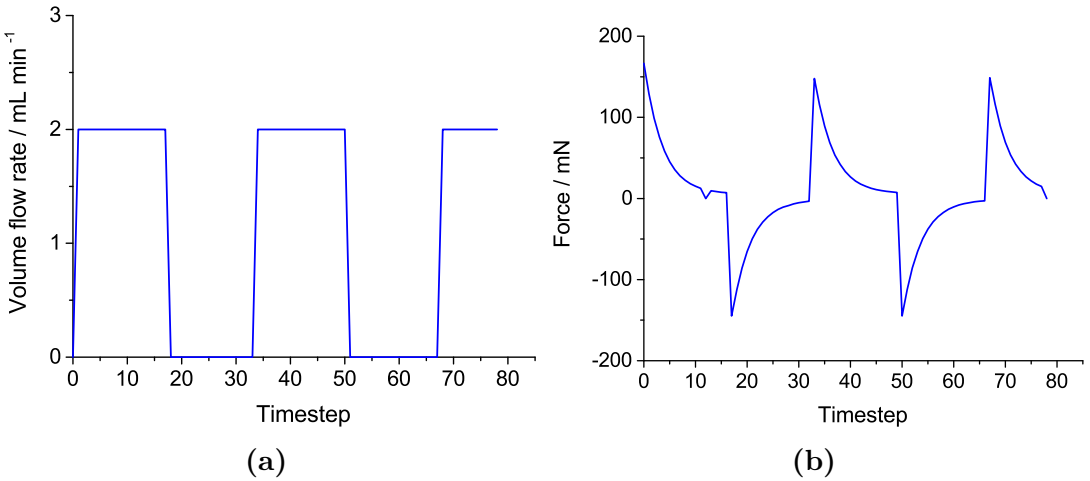

Figure 7.13: Computational fluid dynamics (CFD) simulations: (a) A plot of flow rate against time, illustrating the step function of flow boundary condition, corresponding to the pneumatic system being turned on and then turned off; (b) A plot of simulated force acting on the patterned mirror holder (relative to the planar mirror holder) plotted on the same timescale.

of time. Eighty iterations were performed within each timestep to ensure the solution at each timestep converged.

Figure 7.13b shows that when the pumping is started, there is a sudden increase in expansive force on the mirror mounts, which would cause a sudden large change in cavity length. As the pumping continues at the same flow rate, the force on the walls decays to zero, which would be expected to result in a static cavity length. When the pumping is turned off, a sudden, large, negative force is observed, explaining the sudden decrease in cavity length. Since the contraction force decreases over time, the rate of change of cavity length would decrease, as is observed experimentally in the data shown in Figure 7.12.

The graphs in Figure 7.13 show a qualitative agreement with the experimental results shown in Figure 7.12, and suggest that the new flow system will reduce the effects of the flow dynamics on the cavity length, improve the reliability of the data acquired using this system, and move the instrument towards being able to perform real-time analysis of fluid samples. Due to the microfluidic nature of this device, correlating the applied pressures to the generated flow rates has been problematic. This has made it difficult to maintain a constant flow rate in the

cavity whilst accurately mixing solutions to achieve known concentrations. Further improvements to be made include using microfluidic flow monitors as part of a feedback loop to control the backing pressure of each solution reservoir in order to generate known flows accurately.

In principle, both the CFD calculations and Figure 7.12 suggest that if the flow rate is kept constant within a series of experiments there should be no significant vibrations or movement of the mirrors. This should resolve our reliability issues by maintaining cavity alignment.

7.7 Chapter summary

We have described the design and construction of a higher-finesse open-access microcavity sensor for cavity enhanced absorption spectroscopy. Higher reflectivity mirrors and a much more stable and intense light source were utilised in the new prototype with the intention of improving the detection limit relative to the work described in the previous chapter.

The change to a single-wavelength light source required the design and implementation of a new method for determining and maintaining the cavity length. Therefore, a cavity-locking scheme based on the operating principle of a Fabry-Pérot interferometer was introduced.

Using a single plano-concave microcavity within the array with a physical path-length of 839.7 nm, and 4 μm radius of curvature mirror, absorption measurements were performed on concentrations of Methylene Blue ranging from 500 nM to 2.5 μM. Analysis of this data indicated a CEF of around 9270, and a theoretical spectroscopic limit of detection of $\kappa_{\mathrm{min,s}} = 0.0146\ \mathrm{cm}^{-1}$. This corresponds to a minimum detectable concentration of 104 nM Methylene Blue, which given the mode volume of 219 aL, suggests a theoretical minimum detectable number of molecules of 14.

Although the indicated sensitivity is promising, it is emphasised that the reliability of these results is rather poor, with the absorption data demonstrating a large degree of variation. The origin of this variation was determined to be caused by pressure variations within the cavity as liquid samples are pumped through the

flow system. Pressure waves induced by the stepper-motor of the syringe pumps cause angular variation in the alignment of the two cavity mirrors, slightly altering the cavity finesse between each measurement.

To eliminate these pressure waves, the syringe pumps were replaced with a pneumatic flow system and some preliminary tests conducted. These experiments (and CFD simulations run in parallel) indicate that within a single series of experiments, if the flow rate is kept constant there should be no significant vibrations or movement of the mirrors. This should resolve our reliability issues by maintaining cavity alignment.

Due to the microfluidic nature of the device, correlating the applied pneumatic pressure with the resulting flow rates requires the integration of flow rate monitors and development of a feedback system to maintain a constant flow rate in the cavity whilst accurately mixing solutions to achieve known concentrations. Unfortunately this was not possible within the timescale of this thesis, but will be the immediate focus of future work for this project.

In the final chapter, we will summarise the results of this thesis and consider a number of promising directions for future work arising from this investigation.

8

Concluding remarks

We have explored a number of approaches to improving sensitivity in the analysis of small-volume (sub-microlitre) liquid-phase samples through the use of cavity-enhanced spectroscopic techniques. Our investigation began by incorporating a flow cell with microfluidic dimensions into a "macrocavity" formed from two highly reflective dielectric mirrors separated by 51.3 cm. By angling the flow cell relative to the longitudinal axis of the cavity, we minimised the additional cavity losses caused by Fresnel reflections at the surfaces of the flow cell. This macrocavity was then used to perform a single-wavelength CRDS experiment to determine the nitrite concentration within aqueous samples, achieving a detection limit of 8.83 nM nitrite in an illuminated volume of only 74.6 nL.

Despite achieving detection limits appropriate for sensing nitrite at ambient levels in water courses, the size of this macrocavity setup was a clear barrier to application of the approach in a remote sensing application. Therefore, the subsequent chapters of the thesis explored the potential for miniaturisation of our detection scheme. In addition, we focussed on enhancing sensitivity by removing losses due to the sample container through integration of the cavity mirrors into the liquid channel (a "cavity in a chip" configuration).

Chapter 4 detailed our first attempt at integrating cavity mirrors within a microfluidic flow system. We performed CEAS measurements using custom-made

microfluidic chips containing plane-parallel mirrors formed from commercially available enhanced-specular-reflector II (ESRII) film, which were manufactured by our collaborators at the University of Southampton. Unfortunately the results were underwhelming, with almost no cavity enhancement observed. Given the expected investment of time and resources required to perfect this plane-parallel mirror technique, a strategic decision was made to focus on a more well-defined cavity geometry: open-access plano-concave microcavities.

The microcavities described in Chapters 5 to 7 were developed by collaborators in the Department of Materials, originally for applications in quantum electrodynamics. However, during the course of the work described in this thesis, we have worked together to explore applications in chemical sensing. In contrast to the work described in the previous chapters, the microcavities allow optical measurements to be performed in which we monitor the change of wavelength and/or amplitude of a single well-defined cavity mode in response to a liquid sample introduced between the mirrors.

In Chapter 5, we described the design and construction of an open-access microcavity sensor for refractive index measurements. By recording data simultaneously from multiple cavities of different pathlengths, we showed that shifts in the wavelength of resonant cavity modes caused by refractive index changes ("signal") and physical mirror displacements ("noise") can be decoupled, thereby overcoming an inherent challenge for sensors based on open-access cavities. Using 10 μm diameter mirrors with cavity lengths from 2.238 μm to 10.318 μm, we demonstrated refractive index sensing with a limit of detection of 3.5×10^{-4} RIU. The total volume of detection in our setup was 54 fL. Thus, at the limit of detection, the setup can detect the change of refractive index that results from the introduction of 900 zeptomoles (500,000 molecules) of glucose into the device. Whilst there are many approaches to refractive index sensing with higher sensitivity, we have been unable to find references to any system capable of detecting refractive index changes of this magnitude in the tiny volume of liquid probed by this experiment.

We then adapted the microcavity sensor to enable broadband absorption measurements via cavity enhanced absorption spectroscopy (CEAS), as described in Chapter 6. In this experiment, recording data simultaneously from multiple cavities of differing lengths provides absorption data at a number of wavelengths, which can be tuned by altering the length of the microcavity. Using 10 μm diameter mirrors with physical pathlengths from 476 nm to 728 nm, we demonstrated absorption measurements on Methylene Blue with a limit of detection as low as $\kappa_{\mathrm{min,s}} = 1.71$ cm^{-1} within a volume of 580 attolitres, corresponding to less than 2000 molecules within the mode volume of the cavity. Although liquid-phase CEAS has been demonstrated with κ_{min} several orders of magnitude lower than this result, again, we have been unable to find references to any system capable of performing absorption measurements with equal sensitivity on the tiny volume of liquid probed by this experiment.

In both Chapters 5 and 6, the reported detection limits were not an inherent limitation of the microcavity systems, but rather were governed by the quality of the fit to each mode peak. It was noted that the detection limits could be improved by utilising a more intense and stable light source, a more sensitive detector, and a spectrometer with higher resolution, as well as by improving the finesse of the cavities.

Some of these improvements were implemented in the work described in Chapter 7, where we provided an account of the development of a new prototype with improved cavity finesse and a much more intense and stable light source, to improve the detection limit, and improved flow design to reduce the total flow volume to microfluidic dimensions. We also described the development of a cavity-locking scheme to allow the pathlength to be measured and maintained within a single-wavelength experiment. Using a single plano-concave microcavity with a physical pathlength of 839.7 nm and a 4 μm radius of curvature mirror, absorption measurements were performed on concentrations of methylene blue ranging from 500 nM to 2.5 μM. Analysis of this data indicated a CEF of around 9270, and a theoretical spectroscopic limit of detection of $\kappa_{\mathrm{min,s}} = 0.0146$ cm^{-1}.

This corresponds to a minimum detectable concentration of 104 nM methylene blue, which given the mode volume of 219 aL, suggests a theoretical minimum detectable number of molecules of 14.

However, we noted that the reliability of these results was rather poor, as the absorption data demonstrated a large degree of variation as a result of pressure variations within the cavity. CFD simulations of the cavity indicated that these fluctuations were caused by the syringe pump, and a pneumatic pumping system was evaluated as a potential replacement. Preliminary experiments, as well as CFD simulations performed in parallel, indicated that the reliability issues should be resolved using this pneumatic system if the total flow rate is kept constant during a single series of experiments.

In summary, we have demonstrated that cavity enhanced spectroscopies provide significant improvements to small-volume liquid analysis compared with single-pass absorption measurements, and are competitive with existing techniques described in Chapter 1. It is clear that in terms of sensitivity, experimental footprint, and detection volumes, the microcavity sensors provide the most promising direction for future research. The most obvious next step for continued research using this device is the integration of flow rate monitors and development of a feedback system to maintain a constant flow rate in the cavity whilst accurately mixing solutions to achieve known concentrations. The Methylene Blue absorption measurements can then be repeated to demonstrate the indicated detection limits more reliably.

Our collaborators in the Department of Materials have already demonstrated that within a cavity essentially identical to that used in the work described in Chapter 7, it is possible to resolve wavelength shifts as small as 0.9 pm [204]. We can use this value to estimate the minimum detectable change in refractive index achievable in the new setup. Equation 5.6 yields a predicted detection limit of 1.4×10^{-6} RIU.

In addition, although the final prototype described in this thesis reduced the total flow volume to around 700 μL, the flow geometry remains rather rudimentary and we believe that samples still enter the cavities through a combination of forced flow and diffusion. As well as increasing the volume of sample required, as a large

proportion of sample flowed into the system never enters the microcavities, this reliance on diffusion increases the time required to perform each measurement. One simple alteration to the experiment would be to move away from square arrays of microcavities. Given that we only ever use a single column or row of microcavity mirrors, it would be possible to reduce one dimension of the array, significantly reducing the time required for the sample to diffuse to the microcavity furthest from the edge of the array. In the longer term, it would be preferable to design and manufacture true microfluidic channels onto the face of the micromirror array, such that when opposed by a planar mirror, microfluidic channels would be formed along a single row or column of microcavities, leading to forced flow of much smaller volumes of sample. Using this method, it might also be possible to perform simultaneous analysis of multiple individual channels patterned across the array of microcavities.

In this thesis we have demonstrated that the microcavity sensor can be used with great sensitivity for both absorption and refractive index sensing on small-volume liquid-phase samples. More broadly, the microcavities have the potential to act as a general sensing platform which could be used to increase the sensitivity of a number of other optical techniques by exploiting the interaction of confined light with species present within the microcavity. In parallel with the work described in this thesis, our collaborators in Materials have already demonstrated the microcavities' potential for optically trapping and characterising nanoparticles suspended in liquid samples [204]. Furthermore, combining microcavity-enhancement with other common optical detection techniques, such as fluorescence, Raman scattering, and Forster Resonance Energy Transfer (FRET) offers a potential new route to ultra-sensitive detection of a broad range of chemical species. Several such sensing modalities could, in theory, be combined within the same device, further enhancing the opportunities for developing highly sensitive and specific detection and characterisation capabilities for a variety of applications.

References

(1) Berden, G.; Peeters, R.; Meijer, G. Cavity ring-down spectroscopy: Experimental schemes and applications. *International Reviews in Physical Chemistry* **2000**, *19*, 565–607.

(2) Whitesides, G. M. The origins and the future of microfluidics. *Nature* **2006**, *442*, 368–373.

(3) Manz, A.; Graber, N.; Widmer, H. a. Miniaturized total chemical analysis systems: a novel concept for chemical sensing. *Sensors and actuators B: Chemical* **1990**, *1*, 244–248.

(4) Reyes, D. R.; Iossifidis, D.; Auroux, P.-A.; Manz, A. Micro total analysis systems. 1. Introduction, theory, and technology. *Analytical chemistry* **2002**, *74*, 2623–2636.

(5) Auroux, P.-A.; Iossifidis, D.; Reyes, D. R.; Manz, A. Micro total analysis systems. 2. Analytical standard operations and applications. *Analytical chemistry* **2002**, *74*, 2637–2652.

(6) Rushworth, C. M.; Davies, J.; Cabral, J. T.; Dolan, P. R.; Smith, J. M.; Vallance, C. Cavity-enhanced optical methods for online microfluidic analysis. *Chemical Physics Letters* **2012**, *554*, 1–14.

(7) Tabeling, P., *Introduction to microfluidics*; Oxford University Press: 2010.

(8) Culbertson, C. T.; Mickleburgh, T. G.; Stewart-James, S. A.; Sellens, K. A.; Pressnall, M. Micro total analysis systems: fundamental advances and biological applications. *Analytical chemistry* **2013**, *86*, 95–118.

(9) Paguirigan, A. L.; Beebe, D. J. Microfluidics meet cell biology: bridging the gap by validation and application of microscale techniques for cell biological assays. *Bioessays* **2008**, *30*, 811–821.

(10) Kang, L.; Chung, B. G.; Langer, R.; Khademhosseini, A. Microfluidics for drug discovery and development: from target selection to product lifecycle management. *Drug discovery today* **2008**, *13*, 1–13.

(11) Skelton, V.; Greenway, G. M.; Haswell, S. J.; Styring, P.; Morgan, D. O.; Warrington, B.; Wong, S. Y. The preparation of a series of nitrostilbene ester compounds using micro reactor technology. *Analyst* **2001**, *126*, 7–10.

(12) Fletcher, P. D.; Haswell, S. J.; Pombo-Villar, E.; Warrington, B. H.; Watts, P.; Wong, S. Y.; Zhang, X. Micro reactors: principles and applications in organic synthesis. *Tetrahedron* **2002**, *58*, 4735–4757.

(13) Cygan, Z. T.; Cabral, J. T.; Beers, K. L.; Amis, E. J. Microfluidic platform for the generation of organic-phase microreactors. *Langmuir* **2005**, *21*, 3629–3634.

(14) Ohno, K. i.; Tachikawa, K.; Manz, A. Microfluidics: applications for analytical purposes in chemistry and biochemistry. *Electrophoresis* **2008**, *29*, 4443–4453.

(15) Oosterbroek, E.; Van den Berg, A., *Lab-on-a-chip: miniaturized systems for (bio) chemical analysis and synthesis*; Elsevier: 2003.

(16) Daridon, A.; Sequeira, M.; Pennarun-Thomas, G.; Dirac, H.; Krog, J. P.; Gravesen, P.; Lichtenberg, J.; Diamond, D.; Verpoorte, E.; de Rooij, N. F. Chemical sensing using an integrated microfluidic system based on the Berthelot reaction. *Sensors and Actuators B: Chemical* **2001**, *76*, 235–243.

(17) Ramirez-Garcia, S.; Baeza, M.; OToole, M.; Wu, Y.; Lalor, J.; Wallace, G. G.; Diamond, D. Towards the development of a fully integrated polymeric microfluidic platform for environmental analysis. *Talanta* **2008**, *77*, 463–467.

(18) Sieben, V. J.; Floquet, C. F.; Ogilvie, I. R.; Mowlem, M. C.; Morgan, H. Microfluidic colourimetric chemical analysis system: Application to nitrite detection. *Analytical Methods* **2010**, *2*, 484–491.

(19) Floquet, C. F.; Sieben, V. J.; Milani, A.; Joly, E. P.; Ogilvie, I. R.; Morgan, H.; Mowlem, M. C. Nanomolar detection with high sensitivity microfluidic absorption cells manufactured in tinted PMMA for chemical analysis. *Talanta* **2011**, *84*, 235–239.

(20) Beaton, A. D.; Sieben, V. J.; Floquet, C. F.; Waugh, E. M.; Bey, S. A. K.; Ogilvie, I. R.; Mowlem, M. C.; Morgan, H. An automated microfluidic colourimetric sensor applied in situ to determine nitrite concentration. *Sensors and actuators B: Chemical* **2011**, *156*, 1009–1014.

(21) Fukuba, T.; Aoki, Y.; Fukuzawa, N.; Yamamoto, T.; Kyo, M.; Fujii, T. A microfluidic in situ analyzer for ATP quantification in ocean environments. *Lab on a Chip* **2011**, *11*, 3508–3515.

(22) Jokerst, J. C.; Emory, J. M.; Henry, C. S. Advances in microfluidics for environmental analysis. *Analyst* **2012**, *137*, 24–34.

(23) Watanabe, T.; Sassa, F.; Yoshizumi, Y.; Suzuki, H. Review of Microfluidic Devices for On-Chip Chemical Sensing. *Electronics and Communications in Japan* **2017**, *100*, 25–32.

(24) Sajeesh, P.; Sen, A. K. Particle separation and sorting in microfluidic devices: a review. *Microfluidics and Nanofluidics* **2014**, *17*, 1–52.

(25) Ren, K.; Chen, Y.; Wu, H. New materials for microfluidics in biology. *Current Opinion in Biotechnology* **2014**, *25*, 78–85.

(26) Waheed, S.; Cabot, J. M.; Macdonald, N. P.; Lewis, T.; Guijt, R. M.; Paull, B.; Breadmore, M. C. 3D printed microfluidic devices: enablers and barriers. *Lab on a Chip* **2016**, *16*, 1993–2013.

(27) Dittrich, P. S.; Manz, A. Single-molecule fluorescence detection in microfluidic channels—the Holy Grail in µTAS? *Analytical and bioanalytical chemistry* **2005**, *382*, 1771–1782.

(28) Trojanowicz, M. Recent developments in electrochemical flow detections - a review: Part I. Flow analysis and capillary electrophoresis. *Analytica chimica acta* **2009**, *653*, 36–58.

(29) Huang, Y.; Mason, A. J. Lab-on-CMOS integration of microfluidics and electrochemical sensors. *Lab on a Chip* **2013**, *13*, 3929–3934.

(30) Leung, S.-A.; Winkle, R. F.; Wootton, R. C. A method for rapid reaction optimisation in continuous-flow microfluidic reactors using online Raman spectroscopic detection. *Analyst* **2005**, *130*, 46–51.

(31) Cristobal, G.; Arbouet, L.; Sarrazin, F.; Talaga, D.; Bruneel, J.-L.; Joanicot, M.; Servant, L. On-line laser Raman spectroscopic probing of droplets engineered in microfluidic devices. *Lab on a Chip* **2006**, *6*, 1140–1146.

(32) Massin, C.; Vincent, F.; Homsy, A.; Ehrmann, K.; Boero, G.; Besse, P.-A.; Daridon, A.; Verpoorte, E.; De Rooij, N.; Popovic, R. Planar microcoil-based microfluidic NMR probes. *Journal of Magnetic Resonance* **2003**, *164*, 242–255.

(33) Koster, S.; Verpoorte, E. A decade of microfluidic analysis coupled with electrospray mass spectrometry: An overview. *Lab on a Chip* **2007**, *7*, 1394–1412.

(34) Callis, J. B.; Illman, D. L.; Kowalski, B. R. Process analytical chemistry. *Analytical Chemistry* **1987**, *59*, 624A–637A.

(35) Skelton, V.; Greenway, G. M.; Haswell, S. J.; Styring, P.; Morgan, D. O.; Warrington, B. H.; Wong, S. Y. The generation of concentration gradients using electroosmotic flow in micro reactors allowing stereoselective chemical synthesis. *Analyst* **2001**, *126*, 11–13.

(36) Kawaguchi, T.; Miyata, H.; Ataka, K.; Mae, K.; Yoshida, J. Room temperature swern oxidations by using a microscale flow system. *Angewandte Chemie International Edition* **2005**, *44*, 2413–2416.

(37) Sands, M.; Haswell, S. J.; Kelly, S. M.; Skelton, V.; Morgan, D. O.; Styring, P.; Warrington, B. The investigation of an equilibrium dependent reaction for the formation of enamines in a microchemical system. *Lab on a Chip* **2001**, *1*, 64–65.

(38) Wiles, C.; Watts, P.; Haswell, S. J.; Pombo-Villar, E. The aldol reaction of silyl enol ethers within a micro reactor. *Lab on a Chip* **2001**, *1*, 100–101.

(39) Wiles, C.; Watts, P.; Haswell, S. J.; Pombo-Villar, E. 1, 4-Addition of enolates to α, β-unsaturated ketones within a micro reactor. *Lab on a Chip* **2002**, *2*, 62–64.

(40) Pang, X.; Lewis, A. C. A microfluidic lab-on-chip derivatisation technique for the measurement of gas phase formaldehyde. *Analytical Methods* **2012**, *4*, 2013–2020.

(41) Yin, H.; Killeen, K.; Brennen, R.; Sobek, D.; Werlich, M.; van de Goor, T. Microfluidic chip for peptide analysis with an integrated HPLC column, sample enrichment column, and nanoelectrospray tip. *Analytical Chemistry* **2005**, *77*, 527–533.

(42) Olson, D. L.; Peck, T. L.; Webb, A. G.; Magin, R. L.; Sweedler, J. V. High-resolution microcoil 1H-NMR for mass-limited, nanoliter-volume samples. *Science* **1995**, *270*, 1967.

(43) Pfeiffer, S. A.; Nagl, S. Microfluidic platforms employing integrated fluorescent or luminescent chemical sensors: a review of methods, scope and applications. *Methods and Applications in Fluorescence* **2015**, *3*, 034003.

(44) Streets, A. M.; Huang, Y. Microfluidics for biological measurements with single-molecule resolution. *Current Opinion in Biotechnology* **2014**, *25*, 69–77.

(45) Zhu, Y.; Fang, Q. Analytical detection techniques for droplet microfluidics: A review. *Analytica chimica acta* **2013**, *787*, 24–35.

(46) Kirschbaum, S. E.; Baeumner, A. J. A review of electrochemiluminescence (ECL) in and for microfluidic analytical devices. *Analytical and bioanalytical chemistry* **2015**, *407*, 3911–3926.

(47) Kuswandi, B.; Huskens, J.; Verboom, W. Optical sensing systems for microfluidic devices: a review. *Analytica chimica acta* **2007**, *601*, 141–155.

(48) Bernath, P. F., *Spectra of atoms and molecules*; Oxford University Press: 2015.

(49) Van der Sneppen, L.; Ariese, F.; Gooijer, C.; Ubachs, W. Cavity ring-down spectroscopy for detection in liquid chromatography at UV wavelengths using standard cuvettes in a normal incidence geometry. *Journal of Chromatography A* **2007**, *1148*, 184–188.

(50) Wu, M.-H.; Cai, H.; Xu, X.; Urban, J. P.; Cui, Z.-F.; Cui, Z. A SU-8/PDMS hybrid microfluidic device with integrated optical fibers for online monitoring of lactate. *Biomedical Microdevices* **2005**, *7*, 323–329.

(51) Jindal, R.; Cramer, S. M. On-chip electrochromatography using sol gel immobilized stationary phase with UV absorbance detection. *Journal of Chromatography A* **2004**, *1044*, 277–285.

(52) Mogensen, K. B.; El-Ali, J.; Wolff, A.; Kutter, J. P. Integration of polymer waveguides for optical detection in microfabricated chemical analysis systems. *Applied Optics* **2003**, *42*, 4072–4079.

(53) Mogensen, K. B.; Eriksson, F.; Gustafsson, O.; Nikolajsen, R. P.; Kutter, J. P. Pure silica optical waveguides, fiber couplers, and high aspect ratio submicrometer channels for electrokinetic separation devices. *Electrophoresis* **2004**, *25*, 3788–3795.

(54) Mogensen, K. B.; Kutter, J. P. Optical detection in microfluidic systems. *Electrophoresis* **2009**, *30*, S92–S100.

(55) Landers, J. P., *Handbook of capillary and microchip electrophoresis and associated microtechniques*, 3rd; CRC press: 2008, p 1255.

(56) Gotz, S.; Karst, U. Recent developments in optical detection methods for microchip separations. *Analytical and bioanalytical chemistry* **2007**, *387*, 183–192.

(57) Streets, A. M.; Huang, Y. Chip in a lab: Microfluidics for next generation life science research. *Biomicrofluidics* **2013**, *7*, 011302.

(58) Hindson, B. J.; Ness, K. D.; Masquelier, D. A.; Belgrader, P.; Heredia, N. J.; Makarewicz, A. J.; Bright, I. J.; Lucero, M. Y.; Hiddessen, A. L.; Legler, T. C. High-throughput droplet digital PCR system for absolute quantitation of DNA copy number. *Analytical chemistry* **2011**, *83*, 8604–8610.

(59) Hindson, C. M.; Chevillet, J. R.; Briggs, H. A.; Gallichotte, E. N.; Ruf, I. K.; Hindson, B. J.; Vessella, R. L.; Tewari, M. Absolute quantification by droplet digital PCR versus analog real-time PCR. *Nature methods* **2013**, *10*, 1003–1005.

(60) Pekin, D.; Skhiri, Y.; Baret, J.-C.; Le Corre, D.; Mazutis, L.; Salem, C. B.; Millot, F.; El Harrak, A.; Hutchison, J. B.; Larson, J. W. Quantitative and sensitive detection of rare mutations using droplet-based microfluidics. *Lab on a chip* **2011**, *11*, 2156–2166.

(61) Zhong, Q.; Bhattacharya, S.; Kotsopoulos, S.; Olson, J.; Taly, V.; Griffiths, A. D.; Link, D. R.; Larson, J. W. Multiplex digital PCR: breaking the one target per color barrier of quantitative PCR. *Lab on a Chip* **2011**, *11*, 2167–2174.

(62) Tadmor, A. D.; Ottesen, E. A.; Leadbetter, J. R.; Phillips, R. Probing individual environmental bacteria for viruses by using microfluidic digital PCR. *Science* **2011**, *333*, 58–62.

(63) Warren, L.; Bryder, D.; Weissman, I. L.; Quake, S. R. Transcription factor profiling in individual hematopoietic progenitors by digital RT-PCR. *Proceedings of the National Academy of Sciences* **2006**, *103*, 17807–17812.

(64) Fan, H. C.; Blumenfeld, Y. J.; El-Sayed, Y. Y.; Chueh, J.; Quake, S. R. Microfluidic digital PCR enables rapid prenatal diagnosis of fetal aneuploidy. *American journal of obstetrics and gynecology* **2009**, *200*, 543–e1.

(65) Fan, H. C.; Wang, J.; Potanina, A.; Quake, S. R. Whole-genome molecular haplotyping of single cells. *Nat Biotech* **2011**, *29*, 51–57.

(66) Amitani, I.; Liu, B.; Dombrowski, C. C.; Baskin, R. J.; Kowalczykowski, S. C. Watching individual proteins acting on single molecules of DNA. *Methods in enzymology* **2010**, *472*, 261–291.

(67) Forget, A. L.; Dombrowski, C. C.; Amitani, I.; Kowalczykowski, S. C. Exploring protein-DNA interactions in 3D using in situ construction, manipulation and visualization of individual DNA dumbbells with optical traps, microfluidics and fluorescence microscopy. *Nature protocols* **2013**, *8*, 525–538.

(68) Forget, A. L.; Kowalczykowski, S. C. Single-molecule imaging of DNA pairing by RecA reveals a three-dimensional homology search. *Nature* **2012**, *482*, 423–427.

(69) Song, H.; Chen, D. L.; Ismagilov, R. F. Reactions in droplets in microfluidic channels. *Angewandte chemie international edition* **2006**, *45*, 7336–7356.

(70) Srisa-Art, M.; Sharma, S. In *Microfluidic Diagnostics: Methods and Protocols*, Jenkins, G., Mansfield, C. D., Eds.; Humana Press: Totowa, NJ, 2013, pp 231–240.

(71) Chrimes, A. F.; Khoshmanesh, K.; Stoddart, P. R.; Mitchell, A.; Kalantar-zadeh, K. Microfluidics and Raman microscopy: current applications and future challenges. *Chemical Society Reviews* **2013**, *42*, 5880–5906.

(72) Feng, J.; De La Fuente-Nunez, C.; Trimble, M. J.; Xu, J.; Hancock, R. E.; Lu, X. An in situ Raman spectroscopy-based microfluidic lab-on-a-chip platform for non-destructive and continuous characterization of Pseudomonas aeruginosa biofilms. *Chemical Communications* **2015**, *51*, 8966–8969.

(73) Lee, M.; Lee, J. P.; Rhee, H.; Choo, J.; Gyu Chai, Y.; Kyu Lee, E. Applicability of laser induced Raman microscopy for in situ monitoring of imine formation in a glass microfluidic chip. *Journal of Raman Spectroscopy* **2003**, *34*, 737–742.

(74) Mozharov, S.; Nordon, A.; Girkin, J. M.; Littlejohn, D. Non-invasive analysis in micro-reactors using Raman spectrometry with a specially designed probe. *Lab on a Chip* **2010**, *10*, 2101–2107.

(75) Rinke, G.; Ewinger, A.; Kerschbaum, S.; Rinke, M. In situ Raman spectroscopy to monitor the hydrolysis of acetal in microreactors. *Microfluidics and Nanofluidics* **2011**, *10*, 145–153.

(76) Kim, H. S.; Waqued, S. C.; Nodurft, D.; Devarenne, T. P.; Yakovlev, V. V.; Han, A. Raman spectroscopy compatible PDMS droplet microfluidic culture and analysis platform towards on-chip lipidomics. *Analyst* **2017**, *142*, 1054–1060.

(77) Luther, S.; Will, S.; Braeuer, A. Phase-specific Raman spectroscopy for fast segmented microfluidic flows. *Lab on a Chip* **2014**, *14*, 2910–2913.

(78) Barnes, S. E.; Cygan, Z. T.; Yates, J. K.; Beers, K. L.; Amis, E. J. Raman spectroscopic monitoring of droplet polymerization in a microfluidic device. *Analyst* **2006**, *131*, 1027–1033.

(79) Mogensen, K. B.; Klank, H.; Kutter, J. P. Recent developments in detection for microfluidic systems. *Electrophoresis* **2004**, *25*, 3498–3512.

(80) Kneipp, J.; Kneipp, H.; Rajadurai, A.; Redmond, R. W.; Kneipp, K. Optical probing and imaging of live cells using SERS labels. *Journal of Raman Spectroscopy* **2009**, *40*, 1–5.

(81) Chen, L.; Choo, J. Recent advances in surface enhanced Raman scattering detection technology for microfluidic chips. *Electrophoresis* **2008**, *29*, 1815–1828.

(82) Cecchini, M. P.; Hong, J.; Lim, C.; Choo, J.; Albrecht, T.; deMello, A. J.; Edel, J. B. Ultrafast surface enhanced resonance Raman scattering detection in droplet-based microfluidic systems. *Analytical chemistry* **2011**, *83*, 3076–3081.

(83) Wang, J. Electrochemical detection for microscale analytical systems: a review. *Talanta* **2002**, *56*, 223–231.

(84) Gencoglu, A.; Minerick, A. R. Electrochemical detection techniques in micro- and nanofluidic devices. *Microfluidics and Nanofluidics* **2014**, *17*, 781–807.

(85) Sassa, F.; Laghzali, H.; Fukuda, J.; Suzuki, H. Coulometric Detection of Components in Liquid Plugs by Microfabricated Flow Channel and Electrode Structures. *Analytical Chemistry* **2010**, *82*, 8725–8732.

(86) Vandaveer, W. R.; Pasas Farmer, S. A.; Fischer, D. J.; Frankenfeld, C. N.; Lunte, S. M. Recent developments in electrochemical detection for microchip capillary electrophoresis. *Electrophoresis* **2004**, *25*, 3528–3549.

(87) Kang, S.; Nieuwenhuis, A. F.; Mathwig, K.; Mampallil, D.; Lemay, S. G. Electrochemical Single-Molecule Detection in Aqueous Solution Using Self-Aligned Nanogap Transducers. *ACS Nano* **2013**, *7*, 10931–10937.

(88) Choi, S.; Goryll, M.; Sin, L. Y. M.; Wong, P. K.; Chae, J. Microfluidic-based biosensors toward point-of-care detection of nucleic acids and proteins. *Microfluidics and Nanofluidics* **2011**, *10*, 231–247.

(89) Manica, D. P.; Mitsumori, Y.; Ewing, A. G. Characterization of electrode fouling and surface regeneration for a platinum electrode on an electrophoresis microchip. *Analytical chemistry* **2003**, *75*, 4572–4577.

(90) Petersen, N. J.; Mogensen, K. B.; Kutter, J. P. Performance of an in plane detection cell with integrated waveguides for UV-vis absorbance measurements on microfluidic separation devices. *Electrophoresis* **2002**, *23*, 3528–3536.

(91) Wang, T.; Aiken, J. H.; Huie, C. W.; Hartwick, R. A. Nanoliter-scale multireflection cell for absorption detection in capillary electrophoresis. *Analytical chemistry* **1991**, *63*, 1372–1376.

(92) O'Keefe, A. Integrated cavity output analysis of ultra-weak absorption. *Chemical Physics Letters* **1998**, *293*, 331–336.

(93) Moring, S. E.; Reel, R. T.; van Soest, R. E. Optical improvements of a Z-shaped cell for high-sensitivity UV absorbance detection in capillary electrophoresis. *Analytical Chemistry* **1993**, *65*, 3454–3459.

(94) Xue, Y.; Yeung, E. S. Characterization of band broadening in capillary electrophoresis due to nonuniform capillary geometries. *Analytical Chemistry* **1994**, *66*, 3575–3580.

(95) Alves-Segundo, R.; Ibanez-Garcia, N.; Baeza, M.; Puyol, M.; Alonso-Chamarro, J. Towards a monolithically integrated microsystem based on the green tape ceramics technology for spectrophotometric measurements. Determination of chromium (VI) in water. *Microchimica Acta* **2011**, *172*, 225–232.

(96) Chervet, J.; Van Soest, R.; Ursem, M. Z-shaped flow cell for UV detection in capillary electrophoresis. *Journal of Chromatography A* **1991**, *543*, 439–449.

(97) Mainka, A.; Bachmann, K. UV detection of derivatized carbonyl compounds in rain samples in capillary electrophoresis using sample stacking and a Z-shaped flow cell. *Journal of Chromatography A* **1997**, *767*, 241–247.

(98) Ro, K. W.; Lim, K.; Shim, B. C.; Hahn, J. H. Integrated light collimating system for extended optical-path-length absorbance detection in microchip-based capillary electrophoresis. *Analytical chemistry* **2005**, *77*, 5160–5166.

(99) Suhyeon, K.; Weonseop, K.; Jong, H. H. Extended path length post-column flow cell for UV-visible absorbance detection in capillary electrophoresis. *Journal of Chromatography A* **1994**, *680*, 109–116.

(100) Tiggelaar, R.; Veenstra, T.; Sanders, R.; Gardeniers, J.; Elwenspoek, M.; Van den Berg, A. A light detection cell to be used in a micro analysis system for ammonia. *Talanta* **2002**, *56*, 331–339.

(101) Noda, T.; Takao, H.; Yoshioka, K.; Oku, N.; Ashiki, M.; Sawada, K.; Matsumoto, K.; Ishida, M. Performance of absorption photometry microchip for blood hemoglobin measurement integrated with processing circuits and Si (110) 45 degree mirrors. *Sensors and Actuators B: Chemical* **2006**, *119*, 245–250.

(102) Grumann, M.; Moser, I.; Steigert, J.; Riegger, L.; Geipel, A.; Kohn, C.; Urban, G.; Zengerle, R.; Ducree, J. In *18th IEEE International Conference on Micro Electro Mechanical Systems*, IEEE: 2005, pp 108–111.

(103) Steigert, J.; Grumann, M.; Dube, M.; Streule, W.; Riegger, L.; Brenner, T.; Koltay, P.; Mittmann, K.; Zengerle, R.; Ducree, J. Direct hemoglobin measurement on a centrifugal microfluidic platform for point-of-care diagnostics. *Sensors and Actuators A: Physical* **2006**, *130*, 228–233.

(104) Salimi Moosavi, H.; Jiang, Y.; Lester, L.; McKinnon, G.; Harrison, D. J. A multireflection cell for enhanced absorbance detection in microchip based capillary electrophoresis devices. *Electrophoresis* **2000**, *21*, 1291–1299.

(105) Verpoorte, E.; Manz, A.; Ludi, H.; Bruno, A.; Maystre, F.; Krattiger, B.; Widmer, H.; Van der Schoot, B.; De Rooij, N. A silicon flow cell for optical detection in miniaturized total chemical analysis systems. *Sensors and Actuators B: Chemical* **1992**, *6*, 66–70.

(106) Ellis, P. S.; Lyddy-Meaney, A. J.; Worsfold, P. J.; McKelvie, I. D. Multi-reflection photometric flow cell for use in flow injection analysis of estuarine waters. *Analytica Chimica Acta* **2003**, *499*, 81–89.

(107) Mishra, S. K.; Dasgupta, P. K. Capillary scale light emitting diode based multi-reflection absorbance detector. *Analytica chimica acta* **2007**, *605*, 166–174.

(108) Llobera, A.; Wilke, R.; Buttgenbach, S. Optimization of poly (dimethylsiloxane) hollow prisms for optical sensing. *Lab on a Chip* **2005**, *5*, 506–511.

(109) Llobera, A.; Demming, S.; Wilke, R.; Buttgenbach, S. Multiple internal reflection poly (dimethylsiloxane) systems for optical sensing. *Lab on a Chip* **2007**, *7*, 1560–1566.

(110) Duggan, M. P.; McCreedy, T.; Aylott, J. W. A non-invasive analysis method for on-chip spectrophotometric detection using liquid-core waveguiding within a 3D architecture. *Analyst* **2003**, *128*, 1336–1340.

(111) Patey, M. D.; Rijkenberg, M. J.; Statham, P. J.; Stinchcombe, M. C.; Achterberg, E. P.; Mowlem, M. Determination of nitrate and phosphate in seawater at nanomolar concentrations. *TrAC Trends in Analytical Chemistry* **2008**, *27*, 169–182.

(112) Pan, J.-Z.; Yao, B.; Fang, Q. Hand-held photometer based on liquid-core waveguide absorption detection for nanoliter-scale samples. *Analytical chemistry* **2010**, *82*, 3394–3398.

(113) Berden, G.; Engeln, R., *Cavity ring-down spectroscopy: techniques and applications*; John Wiley & Sons: 2009.

(114) Gagliardi, G.; Loock, H.-P., *Cavity-Enhanced Spectroscopy and Sensing*; Springer: 2014.

(115) Van der Sneppen, L.; Ariese, F.; Gooijer, C.; Ubachs, W. Liquid-phase and evanescent-wave cavity ring-down spectroscopy in analytical chemistry. *Annual Review of Analytical Chemistry* **2009**, *2*, 13–35.

(116) Herbelin, J. M.; McKay, J. A. Development of laser mirrors of very high reflectivity using the cavity-attenuated phase-shift method. *Applied optics* **1981**, *20*, 3341–3344.

(117) Kwok, M. A.; Herbelin, J. M.; Ueunten, R. H. Cavity phase shift method for high reflectance measurements at mid-infrared wavelengths. *Optical Engineering* **1982**, *21*, 216979.

(118) Schmidt, F. M.; Foltynowicz, A.; Ma, W.; Lock, T.; Axner, O. Doppler-broadened fiber-laser-based NICE-OHMS improved detectability. *Optics express* **2007**, *15*, 10822–10831.

(119) Trichet, A.; Foster, J.; Omori, N.; James, D.; Dolan, P.; Hughes, G.; Vallance, C.; Smith, J. Open-access optical microcavities for lab-on-a-chip refractive index sensing. *Lab on a Chip* **2014**, *14*, 4244–4249.

(120) Mazurenka, M.; Orr-Ewing, A. J.; Peverall, R.; Ritchie, G. A. Cavity ring-down and cavity enhanced spectroscopy using diode lasers. *Annual Reports Section" C"(Physical Chemistry)* **2005**, *101*, 100–142.

(121) Rushworth, C. Analysis of Small Volume Liquid Samples using Cavity Enhanced Absorption Spectroscopies., Thesis, University of Oxford, 2012.

(122) Kogelnik, H.; Li, T. Laser beams and resonators. *Applied optics* **1966**, *5*, 1550–1567.

(123) Zalicki, P.; Zare, R. N. Cavity ring down spectroscopy for quantitative absorption measurements. *The Journal of chemical physics* **1995**, *102*, 2708–2717.

(124) Scherer, J.; Paul, J.; O'keefe, A.; Saykally, R. Cavity ringdown laser absorption spectroscopy: history, development, and application to pulsed molecular beams. *Chemical reviews* **1997**, *97*, 25–52.

(125) Wheeler, M. D.; Newman, S. M.; Orr-Ewing, A. J.; Ashfold, M. N. Cavity ring-down spectroscopy. *Journal of the Chemical Society, Faraday Transactions* **1998**, *94*, 337–351.

(126) Paldus, B. A.; Kachanov, A. A. An historical overview of cavity-enhanced methods. *Canadian Journal of Physics* **2005**, *83*, 975–999.

(127) Vallance, C. Innovations in cavity ringdown spectroscopy. *New journal of chemistry* **2005**, *29*, 867–874.

(128) James, D.; Oag, B.; Rushworth, C. M.; Lee, J. W.; Davies, J.; Cabral, J. T.; Vallance, C. High-sensitivity online detection for microfluidics via cavity ringdown spectroscopy. *RSC Advances* **2012**, *2*, 5376–5384.

(129) Fiedler, S. E.; Hese, A.; Ruth, A. A. Incoherent broad-band cavity-enhanced absorption spectroscopy. *Chemical physics letters* **2003**, *371*, 284–294.

(130) Seetohul, L. N.; Ali, Z.; Islam, M. Liquid-phase broadband cavity enhanced absorption spectroscopy (BBCEAS) studies in a 20 cm cell. *Analyst* **2009**, *134*, 1887–1895.

(131) Hallock, A. J.; Berman, E. S.; Zare, R. N. Direct monitoring of absorption in solution by cavity ring-down spectroscopy. *Analytical chemistry* **2002**, *74*, 1741–1743.

(132) Fiedler, S. E.; Hese, A.; Ruth, A. A. Incoherent broad-band cavity-enhanced absorption spectroscopy of liquids. *Review of Scientific Instruments* **2005**, *76*.

(133) Xu, S. C.; Sha, G. H.; Xie, J. C. Cavity ring-down spectroscopy in the liquid phase. *Review of Scientific Instruments* **2002**, *73*, 255–258.

(134) Alexander, A. Flowing liquid-sheet jet for cavity ring-down absorption measurements. *Analytical chemistry* **2006**, *78*, 5597–5600.

(135) Schnippering, M.; Neil, S. R.; Mackenzie, S. R.; Unwin, P. R. Evanescent wave cavity-based spectroscopic techniques as probes of interfacial processes. *Chemical Society Reviews* **2011**, *40*, 207–220.

(136) Hallock, A.; Berman, E.; Zare, R. Use of broadband, continuous-wave diode lasers in cavity ring-down spectroscopy for liquid samples. *Applied spectroscopy* **2003**, *57*, 571–573.

(137) Snyder, K. L.; Zare, R. N. Cavity ring-down spectroscopy as a detector for liquid chromatography. *Analytical chemistry* **2003**, *75*, 3086–3091.

(138) Bahnev, B.; Van der Sneppen, L.; Wiskerke, A.; Ariese, F.; Gooijer, C.; Ubachs, W. Miniaturized cavity ring-down detection in a liquid flow cell. *Analytical chemistry* **2005**, *77*, 1188–1191.

(139) Bechtel, K. L.; Zare, R. N.; Kachanov, A. A.; Sanders, S. S.; Paldus, B. A. Moving beyond Traditional UV-visible Absorption Detection. Cavity Ring-Down Spectroscopy for HPLC. *Analytical chemistry* **2005**, *77*, 1177–1182.

(140) Van der Sneppen, L.; Wiskerke, A.; Ariese, F.; Gooijer, C.; Ubachs, W. Improving the sensitivity of HPLC absorption detection by cavity ring-down spectroscopy in a liquid-only cavity. *Analytica Chimica Acta* **2006**, *558*, 2–6.

(141) Van der Sneppen, L.; Wiskerke, A.; Ariese, F.; Gooijer, C.; Ubachs, W. Cavity ring-down spectroscopy for detection in liquid chromatography: extension to tunable sources and ultraviolet wavelengths. *Applied spectroscopy* **2006**, *60*, 931–935.

(142) McGarvey, T.; Conjusteau, A.; Mabuchi, H. Finesse and sensitivity gain in cavity-enhanced absorption spectroscopy of biomolecules in solution. *Optics express* **2006**, *14*, 10441–10451.

(143) Islam, M.; Seetohul, L. N.; Ali, Z. Liquid-Phase Broadband Cavity-Enhanced Absorption Spectroscopy Measurements in a 2 mm Cuvette. *Applied Spectroscopy* **2007**, *61*, 649–658.

(144) Seetohul, L. N.; Ali, Z.; Islam, M. Broadband cavity enhanced absorption spectroscopy as a detector for HPLC. *Analytical chemistry* **2009**, *81*, 4106–4112.

(145) Kiwanuka, S. S.; Laurila, T.; Kaminski, C. F. Sensitive Method for the Kinetic Measurement of Trace Species in Liquids Using Cavity Enhanced Absorption Spectroscopy with Broad Bandwidth Supercontinuum Radiation. *Analytical Chemistry* **2010**, *82*, 7498–7501.

(146) Ruth, A. A.; Lynch, K. T. Incoherent broadband cavity-enhanced total internal reflection spectroscopy of surface-adsorbed metallo-porphyrins. *Physical Chemistry Chemical Physics* **2008**, *10*, 7098–7108.

(147) Van der Sneppen, L.; Hancock, G.; Kaminski, C.; Laurila, T.; Mackenzie, S. R.; Neil, S. R. T.; Peverall, R.; Ritchie, G. A. D.; Schnippering, M.; Unwin, P. R. Following interfacial kinetics in real time using broadband evanescent wave cavity-enhanced absorption spectroscopy: a comparison of light-emitting diodes and supercontinuum sources. *Analyst* **2010**, *135*, Times Cited: 29 0 29, 133–139.

(148) Rushworth, C. M.; James, D.; Lee, J. W.; Vallance, C. Top notch design for fiber-loop cavity ring-down spectroscopy. *Analytical chemistry* **2011**, *83*, 8492–8500.

(149) Von Lerber, T.; Sigrist, M. W. Cavity-ring-down principle for fiber-optic resonators: experimental realization of bending loss and evanescent-field sensing. *Applied optics* **2002**, *41*, 3567–3575.

(150) Vogler, D. E.; Muller, M. G.; Sigrist, M. W. Fiber-optic cavity sensing of hydrogen diffusion. *Applied optics* **2003**, *42*, 5413–5417.

(151) Vogler, D. E.; Lorencak, A.; Rey, J. M.; Sigrist, M. W. Bending loss measurement using a fiber cavity ringdown scheme. *Optics and lasers in engineering* **2005**, *43*, 527–535.

(152) Gupta, M.; Jiao, H.; OKeefe, A. Cavity-enhanced spectroscopy in optical fibers. *Optics letters* **2002**, *27*, 1878–1880.

(153) Brown, R. S.; Kozin, I.; Tong, Z.; Oleschuk, R. D.; Loock, H.-P. Fiber-loop ring-down spectroscopy. *The Journal of chemical physics* **2002**, *117*, 10444–10447.

(154) Tong, Z.; Jakubinek, M.; Wright, A.; Gillies, A.; Loock, H.-P. Fiber-loop ring-down spectroscopy: a sensitive absorption technique for small liquid samples. *Review of scientific instruments* **2003**, *74*, 4818–4826.

(155) Tong, Z.; Wright, A.; McCormick, T.; Li, R.; Oleschuk, R. D.; Loock, H.-P. Phase-shift fiber-loop ring-down spectroscopy. *Analytical chemistry* **2004**, *76*, 6594–6599.

(156) Li, R.; Loock, H.-P.; Oleschuk, R. D. Capillary electrophoresis absorption detection using fiber-loop ring-down spectroscopy. *Analytical chemistry* **2006**, *78*, 5685–5692.

(157) Andachi, M.; Nakayama, T.; Kawasaki, M.; Kurokawa, S.; Loock, H.-P. Fiber-optic ring-down spectroscopy using a tunable picosecond gain-switched diode laser. *Applied Physics B: Lasers and Optics* **2007**, *88*, 131–135.

(158) Waechter, H.; Bescherer, K.; Durr, C. J.; Oleschuk, R. D.; Loock, H.-P. 405 nm absorption detection in nanoliter volumes. *Analytical chemistry* **2009**, *81*, 9048–9054.

(159) Waechter, H.; Munzke, D.; Jang, A.; Loock, H.-P. Simultaneous and continuous multiple wavelength absorption spectroscopy on nanoliter volumes based on frequency-division multiplexing fiber-loop cavity ring-down spectroscopy. *Analytical chemistry* **2011**, *83*, 2719–2725.

(160) Bescherer, K.; Barnes, J. A.; Loock, H.-P. Absorption Measurements in Liquid Core Waveguides Using Cavity Ring-down Spectroscopy. *Analytical Chemistry* **2013**, *85*, 4328–4334.

(161) Wu, Y.; Zhang, D. Y.; Yin, P.; Vollmer, F. Ultraspecific and Highly Sensitive Nucleic Acid Detection by Integrating a DNA Catalytic Network with a Label-Free Microcavity. *Small* **2014**, *10*, 2067–2076.

(162) Rosenblum, S.; Lovsky, Y.; Arazi, L.; Vollmer, F.; Dayan, B. Cavity ring-up spectroscopy for ultrafast sensing with optical microresonators. *Nature Communications* **2015**, *6*, 6788.

(163) Armani, D. K.; Kippenberg, T. J.; Spillane, S. M.; Vahala, K. J. Ultra-high-Q toroid microcavity on a chip. *Nature* **2003**, *421*, 925–928.

(164) Baaske, M. D.; Foreman, M. R.; Vollmer, F. Single-molecule nucleic acid interactions monitored on a label-free microcavity biosensor platform. *Nature nanotechnology* **2014**, *9*, 933–939.

(165) Vollmer, F.; Yang, L. Review Label-free detection with high-Q microcavities: a review of biosensing mechanisms for integrated devices. *Nanophotonics* **2012**, *1*, 267–291.

(166) Lu, T.; Lee, H.; Chen, T.; Herchak, S.; Kim, J.-H.; Fraser, S. E.; Flagan, R. C.; Vahala, K. High sensitivity nanoparticle detection using optical microcavities. *Proceedings of the National Academy of Sciences* **2011**, *108*, 5976–5979.

(167) Arnold, S.; Khoshsima, M.; Teraoka, I.; Holler, S.; Vollmer, F. Shift of whispering-gallery modes in microspheres by protein adsorption. *Optics letters* **2003**, *28*, 272–274.

(168) Nakagawa, K.; Katsuda, T.; Shelkovnikov, A.; De Labachelerie, M.; Ohtsu, M. Highly sensitive detection of molecular absorption using a high finesse optical cavity. *Optics communications* **1994**, *107*, 369–372.

(169) Shao, L.; Jiang, X.; Yu, X.; Li, B.; Clements, W. R.; Vollmer, F.; Wang, W.; Xiao, Y.; Gong, Q. Detection of single nanoparticles and lentiviruses using microcavity resonance broadening. *Advanced Materials* **2013**, *25*, 5616–5620.

(170) Zhu, J.; Ozdemir, S. K.; Xiao, Y.-F.; Li, L.; He, L.; Chen, D.-R.; Yang, L. On-chip single nanoparticle detection and sizing by mode splitting in an ultrahigh-Q microresonator. *Nature photonics* **2010**, *4*, 46–49.

(171) Mazzei, A.; Götzinger, S.; Menezes, L. d. S.; Zumofen, G.; Benson, O.; Sandoghdar, V. Controlled coupling of counterpropagating whispering-gallery modes by a single Rayleigh scatterer: a classical problem in a quantum optical light. *Physical review letters* **2007**, *99*, 173603.

(172) Armani, A. M.; Kulkarni, R. P.; Fraser, S. E.; Flagan, R. C.; Vahala, K. J. Label-free, single-molecule detection with optical microcavities. *science* **2007**, *317*, 783–787.

(173) Hanumegowda, N. M.; Stica, C. J.; Patel, B. C.; White, I.; Fan, X. Refractometric sensors based on microsphere resonators. *Applied Physics Letters* **2005**, *87*, 201107.

(174) Ehrhardt, M.; Koeve, W. Determination of particulate organic carbon and nitrogen. *Methods of Seawater Analysis, Third Edition* **2007**, 437–444.

(175) Millero, F. J., *Chemical oceanography*; CRC PressI Llc: 2013.

(176) Tovar, A.; Moreno, C.; Manuel-Vez, M. P.; Garcıia-Vargas, M. A simple automated method for the speciation of dissolved inorganic nitrogen in seawater. *Analytica Chimica Acta* **2002**, *469*, 235–242.

(177) WHO Guidelines for Drinking-water Quality. *WHO chronicle* **2011**, *38*, 104–8.

(178) EEC A directive of the quality of freshwater needing protection or improvement in order to support fish life. 78/659/EEC. *Official Journal of the European Communities* **1978**, *21*.

(179) European Union Directive 2006/44/EC of the European Parliament and of the Council of 6 September 2006 on the quality of fresh waters needing protection or improvement in order to support fish life. *Official Journal of the European Union* **2006**, *49*.

(180) Bruning-Fann, C. S.; Kaneene, J. The effects of nitrate, nitrite and N-nitroso compounds on human health: a review. *Veterinary and human toxicology* **1993**, *35*, 521–538.

(181) Gould, J.; Roemmich, D.; Wijffels, S.; Freeland, H.; Ignaszewsky, M.; Jianping, X.; Pouliquen, S.; Desaubies, Y.; Send, U.; Radhakrishnan, K. Argo profiling floats bring new era of in situ ocean observations. *Eos* **2004**, *85*, 179–184.

(182) www.argo.net., Web Page.

(183) Moorcroft, M. J.; Davis, J.; Compton, R. G. Detection and determination of nitrate and nitrite: a review. *Talanta* **2001**, *54*, 785–803.

(184) Dutt, J.; Davis, J. Current strategies in nitrite detection and their application to field analysis. *Journal of Environmental Monitoring* **2002**, *4*, 465–471.

(185) Adarsh, N.; Shanmugasundaram, M.; Ramaiah, D. Efficient reaction based colorimetric probe for sensitive detection, quantification, and on-site analysis of nitrite ions in natural water resources. *Analytical chemistry* **2013**, *85*, 10008–10012.

(186) Griess, P. Bemerkungen zu der Abhandlung der HH. Weselsky und Benedikt Ueber einige Azoverbindungen. *European Journal of Inorganic Chemistry* **1879**, *12*, 426–428.

(187) Fox Jr, J. B. Kinetics and mechanisms of the Griess reaction. *Analytical Chemistry* **1979**, *51*, 1493–1502.

(188) Allan, D. W. Statistics of atomic frequency standards. *Proceedings of the IEEE* **1966**, *54*, 221–230.

(189) Yao, W.; Byrne, R. H.; Waterbury, R. D. Determination of nanomolar concentrations of nitrite and nitrate in natural waters using long path length absorbance spectroscopy. *Environmental science & technology* **1998**, *32*, 2646–2649.

(190) Raimbault, P.; Slawyk, G.; Coste, B.; Fry, J. Feasibility of using an automated colorimetric procedure for the determination of seawater nitrate in the 0 to 100 nM range: Examples from field and culture. *Marine Biology* **1990**, *104*, 347–351.

(191) Greenway, G.; Haswell, S.; Petsul, P. Characterisation of a micro-total analytical system for the determination of nitrite with spectrophotometric detection. *Analytica Chimica Acta* **1999**, *387*, 1–10.

(192) Zhang, J.-Z. Shipboard automated determination of trace concentrations of nitrite and nitrate in oligotrophic water by gas-segmented continuous flow analysis with a liquid waveguide capillary flow cell. *Deep Sea Research Part I: Oceanographic Research Papers* **2000**, *47*, 1157–1171.

(193) Manzoori, J. L.; Soflaee, S. Spectrophotometric determination of nitrite after preconcentration on an SDS coated alumun column. *Analytical letters* **2001**, *34*, 231–237.

(194) Steimle, E. T.; Kaltenbacher, E. A.; Byrne, R. H. In situ nitrite measurements using a compact spectrophotometric analysis system. *Marine Chemistry* **2002**, *77*, 255–262.

(195) Adornato, L.; Kaltenbacher, E.; Villareal, T.; Byrne, R. Continuous in situ determinations of nitrite at nanomolar concentrations. *Deep Sea Research Part I: Oceanographic Research Papers* **2005**, *52*, 543–551.

(196) Czugala, M.; Fay, C.; O'Connor, N. E.; Corcoran, B.; Benito-Lopez, F.; Diamond, D. Portable integrated microfluidic analytical platform for the monitoring and detection of nitrite. *Talanta* **2013**, *116*, 997–1004.

(197) Liu, B.; Su, H.; Wang, S.; Zhang, Z.; Liang, Y.; Yuan, D.; Ma, J. Automated determination of nitrite in aqueous samples with an improved integrated flow loop analyzer. *Sensors and Actuators B: Chemical* **2016**, *237*, 710–714.

(198) Rushworth, C. M.; Jones, G.; Fischlechner, M.; Walton, E.; Morgan, H. On-chip cavity-enhanced absorption spectroscopy using a white light-emitting diode and polymer mirrors. *Lab on a Chip* **2015**, *15*, 711–717.

(199) Jonza, J. M.; Weber, M. F.; Ouderkirk, A. J.; Stover, C. A. Optical film., Patent, 1999.

(200) Smith, D., *Delia Smith's cookery course*; Parkwest Pubns: 1978; Vol. 1.

(201) James, D. Cavity ringdown spectroscopy for microfluidics applications., Thesis, University of Oxford, 2011.

(202) Dolan, P. R.; Hughes, G. M.; Grazioso, F.; Patton, B. R.; Smith, J. M. Femtoliter tunable optical cavity arrays. *Optics letters* **2010**, *35*, 3556–3558.

(203) Vallance, C.; Trichet, A. A.; James, D.; Dolan, P. R.; Smith, J. M. Open-access microcavities for chemical sensing. *Nanotechnology* **2016**, *27*, 274003.

(204) Trichet, A. A. P.; Dolan, P. R.; James, D.; Hughes, G. M.; Vallance, C.; Smith, J. M. Nanoparticle Trapping and Characterization Using Open Microcavities. *Nano Letters* **2016**, *16*, 6172–6177.

(205) Trichet, A. A.; Dolan, P. R.; Coles, D. M.; Hughes, G. M.; Smith, J. M. Topographic control of open-access microcavities at the nanometer scale. *Optics express* **2015**, *23*, 17205–17216.

(206) Flatten, L. C.; He, Z.; Coles, D. M.; Trichet, A. A.; Powell, A. W.; Taylor, R. A.; Warner, J. H.; Smith, J. M. Room-temperature exciton-polaritons with two-dimensional WS2. *Scientific Reports* **2016**, *6*.

(207) De L. Kronig, R. On the Theory of Dispersion of X-Rays. *Journal of the Optical Society of America* **1926**, *12*, 547–557.

(208) Brovelli, L.; Keller, U. Simple analytical expressions for the reflectivity and the penetration depth of a Bragg mirror between arbitrary media. *Optics communications* **1995**, *116*, 343–350.

(209) Ghanadzadeh, A.; Zeini, A.; Kashef, A.; Moghadam, M. Concentration effect on the absorption spectra of oxazine1 and methylene blue in aqueous and alcoholic solutions. *Journal of Molecular Liquids* **2008**, *138*, 100–106.

(210) Brackmann, U., *Lambdachrome Laser Dyes*, 3rd; Lambda Physik AG: 2000.

(211) Cygan, A.; Lisak, D.; Morzynski, P.; Bober, M.; Zawada, M.; Pazderski, E.; Ciurylo, R. Cavity mode-width spectroscopy with widely tunable ultra narrow laser. *Optics Express* **2013**, *21*, 29744–29754.